GL01229

A PRELIMINARY ANALYSIS OF INTRINSIC FLUID AND ROCK RESISTIVITY IN ACTIVE HYDROTHERMAL SYSTEMS

B. Moskowitz and D. Norton

Department of Geology and Geophysics, University of Minnesota, Minneapolis, Minnesota 54421
Department of Geosciences, University of Arizona, Tucson, Arizona 85721

Abstract. Electrical resistivity data are utilized in interpretations of subsurface envitonments and to explore for geothermal and mineral resources. Abnormally low resistivity data are alternatively interpreted to indicate the presence of high-temperature fluids or conductive minerals (metal sulfides) at depth, even though relative contributions of thermal, porosity, and fluid composition effects appear to be poorly known. An analysis of intrinsic rock resistivities, calculated electrical porosities, and two-dimensional heat and mass transfer computations indicates that the host rock resistivity distribution around igneous intrusives is directly related to the mode of dispersion of thermal energy away from the pluton. Comparisons between numerical results and field observations in geothermal areas indicate that resistivity values in the vicinity of thermal anomalies are a complex function of fluid circulation patterns, fluid composition, and the distribution of conductive minerals produced by the reaction between circulating fluids and rocks; therefore in many cases, low near-surface resistivity anomalies cannot be entirely accounted for by hot circulating saline fluids, and observations of high thermal gradients associated with low-resistivity anomalies are not unique indications of a high-energy geothermal resource at shallow crustal depths.

Introduction

The nature of rocks in the upper crust is often deduced from apparent electrical resistivity data. The relationship between these data and the intrinsic resistivities is poorly known, and therefore correlation of the electrical resistivity measurement of rocks with variations in rock and pore fluid properties is usually speculative. Although interpretations are based on resistivity data measured in deep drill holes and laboratory measurements on rocks and fluids, the correlation of laboratory measurements, even in well-controlled laboratory experiments, with

rock properties has not been satisfying. Better understanding of this correlation would facilitate mapping subsurface conditions with the aid of electrical survey data and is particularly relevant in regions of active hydrothermal activity, where there is considerable interest in energy resources.

The electrical resistivity variations in upper crustal rocks have been inferred from various electrical methods. The results of these surveys indicate that average resistivity values in stable crustal regions range from 10^5 to 10^2 ohm m [Keller and Frischknecht, 1966; Keller et al., 1966]. An analysis of laboratory experimental data on the resistivity of fluid-saturated crustal rocks coupled with considerations of regional heat flow data predict similar ranges in resistivity to a 40-km depth [Brace, 1971]. Resistivity surveys in regions of geothermal activity indicate anomalously low resistivities, which range between 10 and 100 ohm m [Sato, 1970; Cheng, 1970; Risk et al., 1970; Zohdy et al., 1973; Keller, 1970]. These anomalous values are often attributed to the presence of prospective thermal energy resources.

The properties and conditions in geothermal systems which contribute to resistivity values are fluid and mineral composition, porosity, temperature, and pressure [Brace, 1971; Brace and Orange, 1968; Brace et al., 1965; Keller and Frischknecht, 1966]. The effect of porosity and fluid resistivity on the bulk rock resistivity of sedimentary rocks was deduced by Archie [1942] and extended to crystalline rocks by Brace et al. [1965]. The empirical relationship derived by Archie defines bulk rock resistivity ρ_r as

$$\rho_r = a\rho_f\phi^{-n} \qquad (1)$$

in terms of pore fluid resistivity ρ_f, a proportionality constant a, porosity ϕ, and a factor which depends on the degree of rock consolidation, n. Experimental data by Brace et al. [1965] and Brace [1977] suggest that for fractured media, $a = 1$ and $n = 2$, values which apparently agree with theoretical electrical network models of Greenberg and Brace [1969] and Shankland and Waff [1974]. The porosity value normally used in (1) is that of total rock porosity. However, only those pores which contribute to current flow should be included in this term,

and in fractured media the total porosity is usually not totally composed of interconnected pores, as is indicated by studies of ion transport in these types of rocks [Norton and Knapp, 1977]. Ranges in rock resistivity of 6 orders of magnitude may be realized for reasonable variations in the abundance of interconnected pores in fractured media [Moskowitz, 1977].

The transient thermal history of rocks in hydrothermal systems related to cooling igneous bodies has been simulated, over large regions and for long time periods, by numerical methods [Norton and Knight, 1977]. Since the variation in resistivity of rocks relates directly to subsurface temperature and pressure conditions, their numerical models provide a basis with which to analyze intrinsic resistivity of hydrothermal systems. The purpose of this communication is to present the results of a first-order approximation to the nature of intrinsic resistivity in such systems. The study considered variations in permeability and porosity, heat sources, rock and fluid properties, including variation in pore fluid resistivity as a function of temperature, pressure, and concentration of components in solution, as well as the time dependence of these parameters in a two-dimensional domain.

'Porosity'

The distribution of porosity in the crust varies in response to changes in pore fluid pressure. Effective pressure P_e is the difference between confining pressure P_c and pore fluid pressure P_f:

$$P_e = P_c - P_f \qquad (2)$$

The variation of effective pressure with depth in the crust shows that in many geologic environments, increases in pore fluid pressure, as a result of temperature increases, will cause the effective pressure to decrease [Knapp and Knight, 1977]. As a consequence of the low tensile strength of rocks, when effective pressure is reduced to zero, the rock will fracture. Thus an increase in porosity is expected at zero effective pressure.

The total porosity in fractured media may be represented by

$$\phi = \phi_F + \phi_D + \phi_R \qquad (3)$$

where ϕ_F, the effective flow porosity represents those pores through which the dominant mode of fluid and aqueous species transport is by fluid flow, ϕ_D, the diffusion porosity, represents those pores through which the dominant mode of transport is by diffusion through the aqueous phase, and ϕ_R, the residual porosity, represents those pores not connected to ϕ_F or ϕ_D. Field observations and experimental studies indicate that ϕ_R apparently accounts for more than 90% of the total porosity observed in crystalline rocks at ambient conditions [Norton and Knapp, 1977]. Our studies indicate that when ϕ_R values are used in (1), intrinsic resistivities of saturated rocks are predicted reasonably well, whereas ϕ_F and ϕ_D predict values many orders of magnitude higher than observed values [Moskowitz, 1977].

The correlation between porosity values consistent with electrical diffusivity and ion diffusivity determined by Norton and Knapp [1977] is unclear. We have assumed that pore fluid thermal expansion in residual pores produces fractures which contribute to electrical porosity. The pore characteristics at which the fluid will simply flow from the pore in response to thermal expansion and not increase the porosity are considered to be typical of the flow porosity normally found in crystalline rocks. Therefore any increases in total porosity due to temperature occur approximately as the result of changes in residual porosity. These assumptions are justified by the fact that $\phi_R \simeq 0.9\phi$ and that ϕ is used in Archie's law. Residual porosity is certainly an upper limit to the actual electrical porosity of crystalline rocks, and subsequently, the intrinsic resistivity calculated from these assumptions represents minimum values. Also, conversion of residual porosity to flow or diffusion porosity which relates directly to permeability is not considered in the fluid flow models to be discussed below.

The concept presented by Knapp and Knight [1977] can be used to relate porosity change at zero effective pressure to temperature. The total derivative of the rock-pore volume at constant composition is

$$dV = \left(\frac{\partial V}{\partial T}\right)_P dT + \left(\frac{\partial V}{\partial P}\right)_T dP \qquad (4)$$

where $V = V_r + V_f$, V_r is rock volume, and V_f is pore volume. The coefficients of isobaric thermal expansion α and isothermal compressibility β for the bulk rock are defined as

$$\alpha \equiv \frac{1}{V}\left(\frac{\partial V}{\partial T}\right)_P \qquad (5a)$$

$$\beta \equiv -\frac{1}{V}\left(\frac{\partial V}{\partial P}\right)_T \qquad (5b)$$

Substitution of (5a) and (5b) into (4) defines the total volume change in terms of α and β:

$$dV = V\alpha\, dT - V\beta\, dP \qquad (6)$$

This total derivative can also be expressed in terms of the individual thermal expansions and compressibilities of pore fluid and rock:

$$dV = [V_f\alpha_f + V_r\alpha_r]\, dT - [V_f\beta_f + V_r\beta_r]\, dP \qquad (7)$$

However, when rocks fracture as a consequence of pore fluid expansion, infinitesimal increases in pore fluid pressure will produce further fracturing. Therefore $dP \cong 0$, and (7) may be simplified to

$$dV = [V_f\alpha_f + V_r\alpha_r]\, dT \qquad (8)$$

Typical values for α_r, for common silicate minerals, over a temperature range of 0°-800°C, are of the order of 10^{-6} $^oC^{-1}$ [Clark, 1966]. The thermal expansion coefficient for pure water, over the same temperature span, is of the order of 10^{-3} $^oC^{-1}$. As long as pore volume V_f is greater than or equal to 0.01, $V_f\alpha_f >> V_r\alpha_r$, and (8) becomes

$$dV = V_f \alpha_f \, dT \tag{9}$$

The total volume change, according to (9), occurs as a result of pore volume changes, the rock volume remaining essentially constant. Rearranging (9) with the approximation that $dV \simeq dV_f$ yields an integral equation relating pore volume and temperature:

$$\int_{V_f^o}^{V_f} \frac{dV_f}{V_f} = \int_{T_b}^{T} \alpha_f(T) \, dT \tag{10}$$

In (1), V_f^o is the initial residual pore volume, and T_b is the temperature at which the rock fractures. Integrating (10) gives the pore volume as a function of temperature:

$$V_f = V_f^o \exp \left[\int_{T_b}^{T} \alpha_f(T) \, dT \right] \tag{11}$$

where $T > T_b$. The initial residual porosity ϕ_R^o is defined as

$$\phi_R^o = \frac{V_f^o}{V^o} = \frac{V_f^o}{V_r + V_f^o} \tag{12}$$

and the fluid and rock volumes are

$$V_f^o = \phi_R^o V^o \qquad V_r = (1 - \phi_R^o) V^o \tag{13}$$

respectively. Substituting (12) and (13) into (11) defines a porosity temperature function in terms of the initial residual porosity:

$$\phi_R = \frac{\phi_R^{\,o} F(T)}{(1 - \phi_R^{\,o}) + \phi_R^{\,o} F(T)} \tag{14}$$

where

$$F(T) = \exp\left[\int_{T_b}^{T} \alpha_f(T)\, dT\right] \tag{15}$$

For the purposes of this discussion we will consider that (14) defines increases in the effective electrical porosity. That is, all porosity increases due to thermal effects are assumed to contribute to increased electrical current flow in the rocks.

The temperature at which the rocks initially fracture, T_b, may be defined as

$$T_b = T_a + \Delta T \tag{16}$$

where T_a is the ambient temperature and ΔT is the temperature increment necessary to reduce effective pressure to zero. The value of ΔT depends on the geothermal gradient, and the maximum value of ΔT along a gradient of 20°C/km is 20°C [Knapp and Knight, 1977].

Porosity, defined by (14), was computed for depths of 1, 2, 3, and 4 km below the earth's surface (Figure 1). At a depth of 1 km and initial temperature of 40°C, large increases in porosity are predicted for temperature changes of the order of 300°C. However, the porosity increases are small for changes in temperatures of less than 100°C at this same depth. At greater depths, e.g., 4 km, much smaller increases in porosity are predicted for these same temperature conditions, owing to increased confining pressure.

The relationship among bulk rock resistivity, fluid resistivity, and electrical porosity is poorly known. Archie's law, equation (1), has been assumed as an adequate first approximation to rock resistivity. Therefore the important parameter in predicting resistivity from (1) is ϕ^{-2}, and therefore small increases in porosity will result in a significant decrease in ρ_R (Figure 2).

Fluid Resistivity

The resistivity of natural groundwaters varies as a function of temperature, pressure, and composition. Since the dissolved constituents in natural waters are often dominated by sodium and chloride, and the resistivity values of NaCl-H_2O fluids are similar, within a factor of 2.5, to those of other common fluids, the compositional effects of fluid resistivity are approximated by the system NaCl-H_2O [Quist and Marshall, 1968; Chambers, 1957; Gunning and Gordon, 1942]. The variation in resistivity of a 0.1 m NaCl solution with temperature and pressure exhibits a steady, pressure independent decrease in resistivity to approximately 300°C, then an order of magnitude increase to 12 ohm m at 500°C and 500 bars (Figure 3). As can be seen, the dominant pressure effect is to shift the resistivity minimum to higher temperatures with increasing pressure. Increasing the NaCl concentration results in a decrease in resistivity that varies from 100 to 0.01 ohm m for concentrations ranging from 10^{-4} to 2 m.

Fluid temperatures in geothermal reservoirs range up to 300°C, and pressures to 1 kbar. Total ionic strength of these fluids ranges from 1 m, such as was observed in the Imperial Valley system [Meidav and Furgerson, 1972] to 10^{-2} m, such as was observed in the Broadlands, New Zealand, system [Browne and Ellis, 1970]. Typical resistivities of geothermal reservoir fluids range from 0.01 to 10 ohm m [Cheng, 1970], which is similar to the range in resistivity of pore fluids in a variety of geologic environments [Keller and Frischknecht, 1966].

Temperature-Pressure Distribution

Notions of temperatures and pressures in geothermal systems are primarily derived from

production or exploration wells, and consequently, information is restricted to small portions of the total system. Knowledge of these parameters over the entire hydrothermal system is necessary in order to analyze the time dependence of resistivity in the region of a cooling pluton. Simulation of cooling plutons by numerical methods is one method by which these parameters can be defined for an idealized geothermal system.

Fluid flow caused by thermal anomalies related to igneous plutons is effectively scaled and represented in two dimensions by partial differential equations which describe the conservation of mass, momentum, and energy for the fluid-rock system [Norton and Knight, 1977]:

Conservation of energy

$$\gamma\frac{\partial T}{\partial t} + q\nabla H = \nabla\cdot\kappa\nabla T \tag{17}$$

Conservation of momentum

$$\nabla\cdot\frac{\nu}{k}\nabla\Psi = R\frac{\partial\rho}{\partial y} \tag{18}$$

where T is the temperature, Ψ is the stream function, q is the fluid flux, t is the time, H, ρ, and ν are the enthalpy, density, and viscosity of the fluid, k is the permeability of the rock, κ is the thermal conductivity, and γ is the volumetric heat capacity of the fluid-saturated media, R is the Rayleigh number, ∇ is the gradient operator, and y is the horizontal distance in the two-dimensional section to which these equations apply.

Equations (17) and (18) are approximated by finite difference numerical equations which permit computation of the values of the dependent variables at discrete points in the domain from initial and boundary values specified for the system. The numerical analysis provides the option to include variable transport properties of the fluid (H_2O system) and rock, general boundary and initial conditions, and radioactive and volumetric heat sources in a two-dimensional domain. The transport process related to the transient thermal anomaly is approximated by a time sequence of steady state numerical solutions

to (17) and (18), computed at explicitly stable time intervals. An alternating direction implicit finite difference method is used to approximate the spatial derivatives at discrete intervals of the order of 0.1-0.5 of the system height. Fluid pressure in the system is computed at each steady state step by integration of Darcy's law, in which the fluid properties, viscosity and density, are expressed as a function of temperature and pressure.

The methods used by Norton and Knight [1977] were used to define the temperature variation in the environment of a cooling pluton as a function of time. The hypothetical system is characterized by a dominance of convective heat transport over conductive heat transport as a result of relatively large host rock permeabilities (Figure 4). As a consequence of fluid circulation the temperature distribution in the host rocks evolves into a plumose pattern at $\sim 10^5$ years (Figure 5) and results in broad regions of uniform temperature above the pluton.

Initial temperatures in the host rocks at this depth are 110°C, as defined by the 20°C/km geothermal gradient and 20°C surface temperature. At 190,000 years after pluton emplacement the 200°C isotherm is at approximately a 0.5-km depth (Figure 5), and the temperatures between the top of the pluton and the 200°C isotherm have increased by at least 90°C. The pore fluid resistivity reaches a minimum at temperatures between 200°C and 300°C (Figure 3), and the porosity increase defined by (14) is of the order of 15% of the initial value for temperature increases of 100°-200°C. Therefore the zone between the 200°C isotherm and the top of the pluton in the system will be characterized by maximum porosity increase and the maximum decrease in pore fluid resistivity.

Porosities in host rocks at depths of <2 km directly over the pluton have significantly increased approximately 20% of the initial value at 190,000 years after pluton emplacement. This porosity increase persists uniformly to a 4-km depth. Time variations in porosity, calculated at fixed points 4, 2.5, and 0.5 km above the top of the pluton, predict a maximum 0.5 km above the pluton at 4×10^4 and 10^5 years after emplacement (Figure 6). However, as a result of convective transport of thermal energy to the surface a porosity maximum is observed at depths of <2 km.

The spatial and temporal distribution of temperature in the system will directly determine the host rock resistivity distribution. The resistivity isopleths closely parallel the isotherms at 50,000 and 190,000 years (Figures 7 and 8, respectively), which also illustrate the displacement in the resistivity isopleths between 50,000 and 190,000 years. By 190,000 years the lateral extent of the isopleth displacement at a 1-km depth spans the entire width of the system (∿22 km).

In summary, the calculations indicate that the dispersion of thermal energy away from a pluton will directly affect the host rock resistivity. When pluton emplacement is into permeable host rocks, significant decreases in resistivity between the surface and depths of <0.5 km are predicted. These resistivity values then persist uniformly in a vertical zone, extending from 0.5 km to approximately 4 km above the pluton by 190,000 years after pluton emplacement. The maximum decrease in resistivity is less than a factor of 10, as compared to surface values. The range in host rock resistivity is from 10^4 to 10^5 ohm m. These values are quite high with respect to values obtained on real rocks. However, our calculations only account for a conductive fluid in a nonconductive matrix.

Discussion

The temperature variations in hydrothermal systems account for changes in electrical porosity and electrical resistivity of pore fluids. Results of our analysis suggest that resistivity anomalies caused by thermal events are several times broader in extent than the thermal source, and the lateral resistivity gradients at the margins of the anomaly are much lower than the vertical resistivity gradients directly above the pluton. The side and top margins of the resistivity anomaly correspond closely to the 200° isotherm, as a consequence of the fluid properties. A resistivity minimum occurs at relatively shallow depths, e.g., 0.5 km, and extends to 4 km. However, the magnitude of these resistivities is considerably greater than values measured in geothermal systems.

The magnitude of ρ_R is defined by the pore fluid concentration and initial host rock porosity, while the distribution of ρ_R is defined by

the temperature distribution. To determine the change in magnitude of ρ_R, due to varying molality of pore fluids and host rock porosities, a series of calculations was made with different initial values of porosity and NaCl molalities. The isopleths of resistivity as a function of porosity and NaCl molality at constant temperature are defined by (1) and shown for T = 300°C in Figure 9. The results of the calculations summarized as the minimum resistivities predicted for the cooling pluton environment are comparable to actual values realized in geothermal systems and in saline groundwater systems. In order to explain the observed resistivities in geothermal areas (<10 ohm m), high-molality pore fluids and/or high-porosity host rocks must occur for large vertical and horizontal zones within the geothermal system.

The results of this study indicate that rock resistivities characteristic of active hydrothermal systems are considerably less than can be accounted for by simple changes in fluid resistivity or rock porosity. The discrepancies between the numerical resistivity models and the field resistivity observations in geothermal systems may be accounted for by the presence of conducting minerals, since pyrite and conductive clay minerals are typically found in the region of hydrothermal systems over the top of the thermal anomaly. If one uses a conservative estimate of a factor of 10 decrease in host rock resistivities resulting from conducting minerals, a geologically reasonable range in porosity and fluid composition can produce the anomalously low resistivity values observed in geothermal areas. Therefore except in anomalously high salinity and high porosity environments the presence of hot fluids alone is not sufficient to generate the low resistivity values observed in geothermal areas.

Considerable interest has been given to exploration techniques that might be useful in detecting high-energy geothermal systems. Commonly used techniques include measurements of heat flow and electrical resistivity. High heat flow in combination with anomalously low electrical resistivity data have been used as a justification for drilling of exploratory wells. Sedimentary basins and young, old, and mature geothermal systems in fractured rocks constitute a set of geologic environments within which the correlation of high thermal gradients, low near-surface

resistivities, and surface thermal effects may lead to nonunique interpretations of the potential for geothermal energy resources at moderate depths. In the basin and range province of the western United States, concentrated brines associated with evaporite deposits in the high-porosity basins can produce lateral density gradients which cause fluid circulation. Exothermal hydration reactions that produce local thermal anomalies, coupled with the fluid circulation, are often sufficient to cause high surface heat flux and surface thermal springs. The high salinity and high porosity in these sedimentary basins would result in anomalously low near-surface resistivity. This particular environment appears to occur in the Safford Basin, southeastern Arizona [Norton et al., 1975].

Geothermal systems which have nearly cooled to regional background temperatures may be characterized by large conductive heat fluxes [Norton, 1977] as a result of remnant thermal energy that has been transported from the heat source to near-surface environments. Conducting minerals will undoubtedly have been formed above the pluton, and thermal springs will still be prevalent on the surface. In this environment, low resistivity would be associated with the conducting minerals and, in part, with the circulating saline fluids.

Geothermal systems in their early stages of formation have not been studied; however, their characteristics have been numerically simulated. The transport of thermal energy away from a pluton may be rapid with respect to the mass flux of reactive components in solution to the surface. This means that hot saline fluids will dominate changes in host rock resistivities because not enough time has elapsed to produce significant quantities of conducting minerals. High heat flux and surface thermal effects will probably form relatively early in the life cycle of a geothermal system. The calculated resistivity values resulting from increased temperatures are anomalous with respect to background values but are relatively high (10^4-10^5 ohm m). Therefore this environment is characterized by high heat flux and thermal surface effects but probably an undetectable resistivity anomaly, even though there is a high-energy thermal source at depth.

Active, mature geothermal systems are abundant worldwide where high heat flux, thermal surface

effects, and low resistivities are associated with a productive thermal source at depth. However, low-resistivity anomalies, <100 ohm m, are probably caused by the presence of conductive minerals which may be coincident with hot thermal fluids.

The four geologic environments presented serve to illustrate the problems which can be encountered in attempting to interpret near-surface resistivity anomalies. Also a combination of heat flux measurements, surface thermal effects, and low resistivity can be characteristic of both productive high-energy geothermal systems and unproductive low-energy geothermal environments. The observations are also manifested in that electrical methods are used in prospecting for both sulfide mineral deposits and thermal energy.

Acknowledgments. We wish to acknowledge the Energy Research Development Administration for support of this study through contract E-11-1-2763. We thank Robert F. Butler, R. Knapp, and J. Knight for discussions and penetrating questions, L. McLean for editing and typing the manuscript, and the University Computer Center personnel for their assistance.

References

Archie, G. E., The electrical resistivity log as an aid in determining some reservoir characteristics, Trans. AIME, 146, 54-62, 1942.

Brace, W. F., Resistivity of saturated crustal rocks to 40 km based on laboratory studies, in The Structure and Physical Properties of the Earth's Crust, Geophys. Monogr. Ser., vol. 14, edited by J. G. Heacock, pp. 243-257, AGU, Washington, D. C., 1971.

Brace, W. F., Permeability from resistivity and pore shape, J. Geophys. Res., 82, 3343-3349, 1977.

Brace, W. F., and A. S. Orange, Further studies of the effect of pressure on electrical resistivity of rocks, J. Geophys. Res., 73, 5407-5420, 1968.

Brace, W. F., A. S. Orange, and T. R. Madden, The effect of pressure on the electrical resistivity of water-saturated crystalline rocks, J. Geophys. Res., 70, 5669-5678, 1965.

Browne, P. R. L., and A. J. Ellis, the Ohaki-Broadlands hydrothermal area, New Zealand: Mineralogy and related geochemistry, Amer. J. Sci., 269, 97-131, 1970.

Chambers, J. F., The conductance of concentrated aqueous solutions of potassium iodide at 25°C and of potassium and sodium chlorides at 50°C, J. Phys. Chem., 62, 1136, 1958.

Cheng, W. T., Geophysical exploration in the Tatun volcanic region, Taiwan, Geothermics, Spec. Issue, 2 (1), 910-917, 1970.

Clark, S. P. Jr., ed., Handbook of Physical Constants, Geol. Soc. America, Mem. 97, New York, Revised edition.

Greenberg, R. J., and W. F. Brace, Archie's law for rocks modeled by simple networks, J. Geophys. Res., 74, 2099-2101, 1969.

Gunning, H. E., and A. R. Gordon, The conductance and ionic mobilities for aqueous solutions of K and NaCl at T = 15°C-45°C, J. Chem. Phys., 10, 1942.

Keller, G. V., Induction methods in prospecting for hot water, Geothermics, Spec. Issue, 2 (1), 318-332, 1970.

Keller, G. V., and F. C. Frischknecht, Electrical Methods in Geophysical Prospecting, Pergamon, New York, 1966.

Keller, G. V., L. A. Anderson, and J. I. Pritchard, Geological survey investigations of the electrical properties of the crust and upper mantle, Geophysics, 31, 1078-1087, 1966.

Knapp, R., and J. Knight, Differential thermal expansion of pore fluids: Fracture propagation and microearthquake production in hot pluton environments, J. Geophys. Res., 82, 2515-2522, 1977.

Meidav, T., and R. Furgerson, Resistivity studies of the Imperial Valley geothermal area, California, Geothermics, 1, 47-62, 1972.

Mitchell, B. J., and M. Landisman, Geophysical measurements in the southern great plains, in The Structure and Physical Properties of the Earth's Crust, Geophys. Monogr. Ser., vol. 14, edited by J. G. Heacock, pp. 77-95, AGU, Washington, D. C., 1971.

Moskowitz, B. M., Numerical analysis of electrical resistivity in hydrothermal systems, M.S. thesis, Univ. of Ariz., Tucson, 1977.

Norton, D., Fluid circulation in the earth's crust, in The Earth's Crust, Geophys. Monogr. Ser., vol. 20, edited by J. G. Heacock, in press, AGU, Washington, D. C., 1977.

Norton, D., and R. Knapp, Transport phenomena in hydrothermal systems: The nature of porosity, Amer. J. Sci., 277, 913-936, 1977.

Norton, D., and J. Knight, Transport phenomena in hydrothermal systems: Cooling plutons, Amer. J. Sci., 277, 937-981, 1977.

Norton, D., T. Gerlach, K. J. DeCook, and J. S. Sumner, Geothermal water resources in Arizona: Feasibility study, technical completion report, project A-054-ARIZ, Office of Water Res. and Technol., Tucson, Ariz., 1975.

Quist, A. S., and W. L. Marshall, Electrical conductances of aqueous sodium chloride solutions from 0°C to 200°C and at pressures to 4000 bars, J. Phys. Chem., 72, 684-703, 1968.

Risk, G. F., W. J. P. MacDonald, and G. B. Dawson, D. C. resistivity surveys of the Broadlands geothermal region, New Zealand, Geothermics, Spec. Issue, 2 (1), 287-294, 1970.

Sato, K., The present state of geothermal development in Japan, Geothermics, Spec. Issue, 2 (1) 155-184, 1970.

Shankland, T. J., and H. S. Waff, Conductivity in fluid-bearing rocks, J. Geophys. Res., 79, 4863-4868, 1974.

Zohdy, A. A. R., L. A. Anderson, and L. J. P. Muffler, Resistivity, self potential, and induced polarization surveys of a vapor-dominated geothermal system, Geophysics, 38, 1130-1144, 1973.

(Received March 15, 1977;
revised August 15, 1977;
accepted August 26, 1977.)

Fig. 1. Porosity as a function of temperature at depths of 1, 2, 3, and 4 km, as computed from (14). Initial porosity ϕ_o is 0.1, and background temperatures are consistent with a surface temperature of 20°C and a temperature gradient of 20°C/km. Pressures were computed for a rock density of 2.75 g/cm^3. Insert shows porosity values consistent with temperatures up to 1200°C.

Fig. 2. Parameter ϕ^{-2} as a function of temperature at depths of 1, 2, 3, and 4 km. Parameters used are same as those in Figure 1.

Fig. 3. Temperature-pressure projection of the two-phase surface (liquid and vapor) in the H_2O-NaCl system at 0.01-m NaCl concentration depicting fluid resistivity isopleths.

Fig. 4. Two-dimensional cross section of a pluton intruded into uniform permeability host rocks depicting initial and boundary conditions for numerical simulation of heat and mass transfer. Domain was discretized into 120 grid points such that Δz = 0.9 km and Δy = 1.75 km. The initial conditions include a background temperature consistent with a surface temperature of 20°C and a thermal gradient $\nabla_z T$ = 20°C/km. The pluton's initial temperature is 960°C. Permeabilities are 10^{-15} m^2 and 10^{-18} m^2 for the host and pluton rocks, respectively.

Fig. 5. Temperature distribution in an idealised hydrothermal system, defined by Figure 4, for (left) 5 x 10^4 and (right) 1.9 x 10^5 years elapsed time.

Fig. 6. Porosity as a function of time resulting from thermal energy transport into host rocks from the pluton at positions directly over the pluton, 0.5, 2, and 4 km below the surface (Figure 4).

Fig. 7. Resistivity and temperature values in a hydrothermal system at 5×10^4 years elapsed time, depicting the temperature control on intrinsic resistivities.

Fig. 8. Resistivity and temperature values in a hydrothermal system at 1.9×10^5 years elapsed time, depicting the temperature control on intrinsic resistivities.

Fig. 9. Concentration of NaCl in pore fluids and electrical porosity effect on intrinsic rock resistivities, with isopleths of 10, 10^2, 10^3, and 10^4 ohm m. Values are for T = 300°C, at which the minimum in fluid resistivity occurs, and for P = 500 bars. Note that the minimum in fluid resistivity is nearly independent of pressures (Figure 3). Regions delimited by dashed lines represent ranges in values of porosity and fluid compositions observed in the respective geologic environments and for idealised systems considered in this study. The latter are labeled 'fractured igneous systems.'

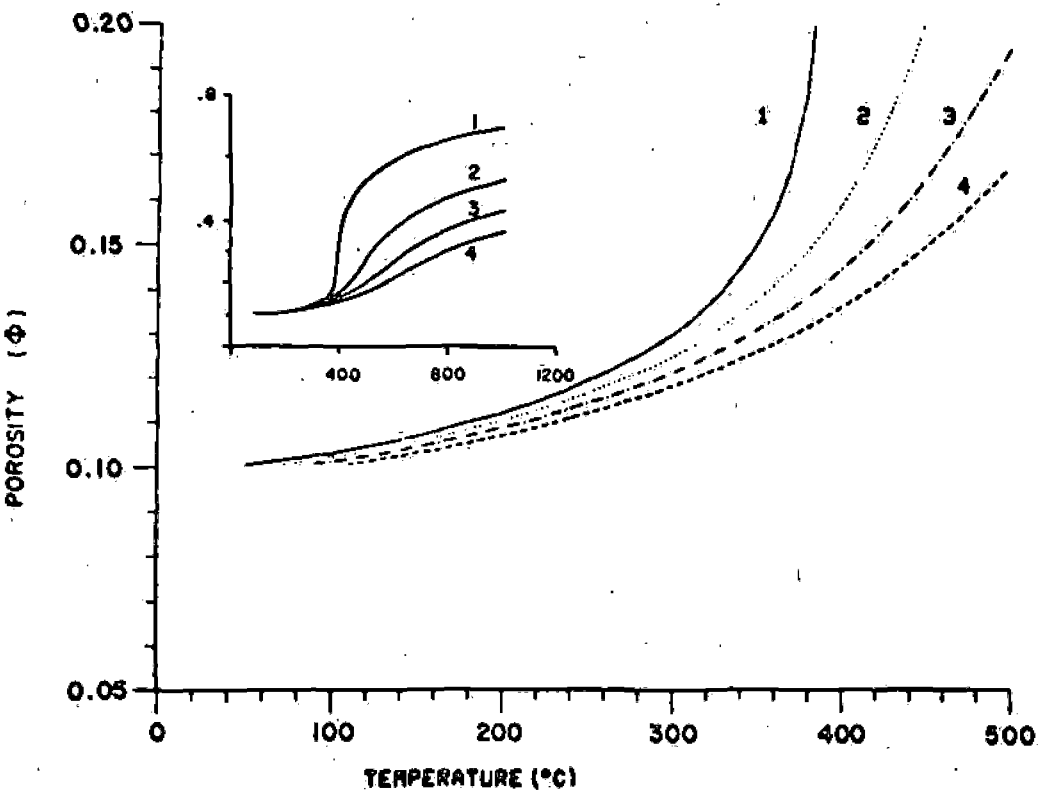
0.20
0.15
0.10
0.05
POROSITY (Φ)
0
100
200
300
400
500
TEMPERATURE (°C)
1
2
3
4
.8
.4
400
800
1200

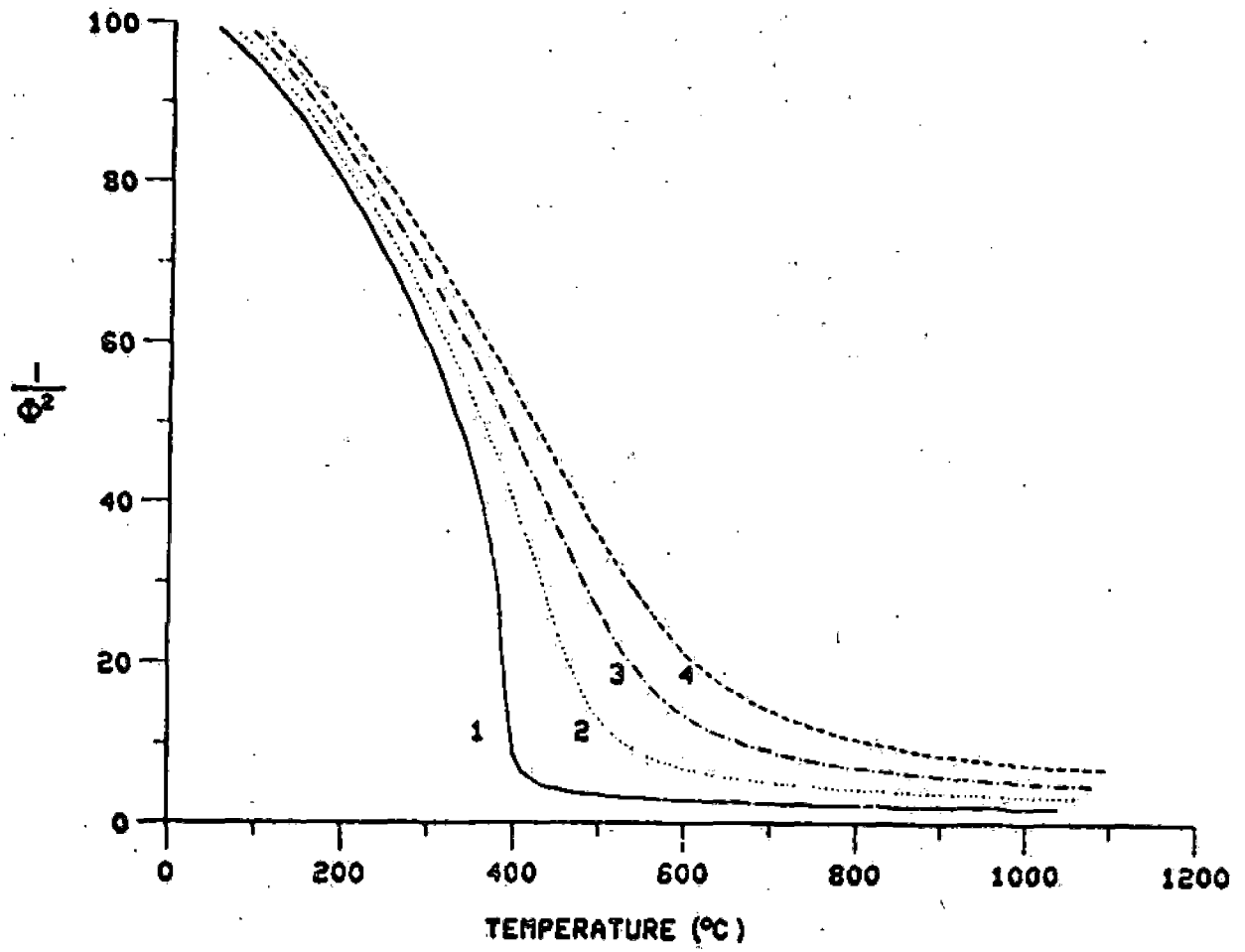
100
80
60
40
20
0
$\frac{1}{\Phi^2}$
0
200
400
600
800
1000
1200
TEMPERATURE (°C)
1
2
3
4

(2)

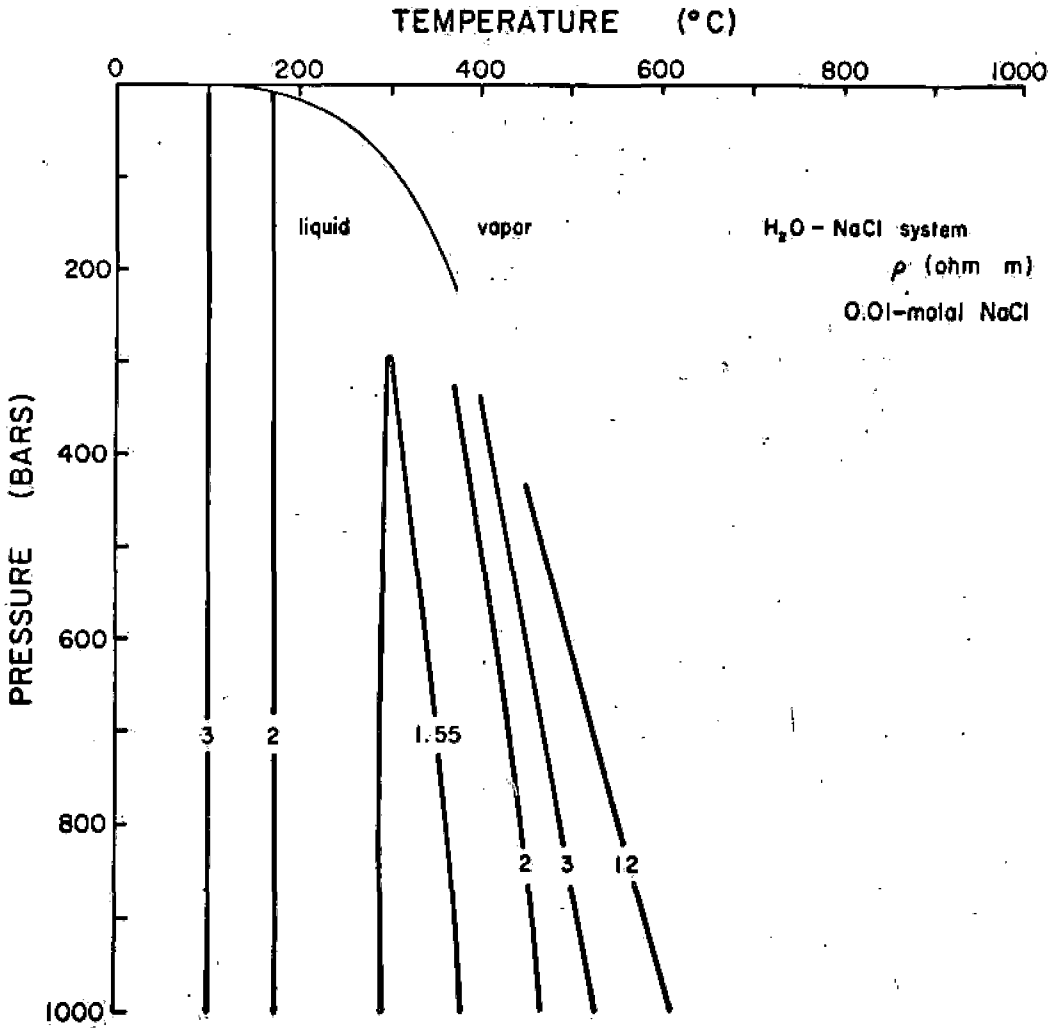
TEMPERATURE (°C)
0
200
400
600
800
1000
PRESSURE (BARS)
200
400
600
800
1000
liquid
vapor
H₂O – NaCl system
ρ (ohm m)
0.01-molal NaCl
3
2
1.55
2
3
12

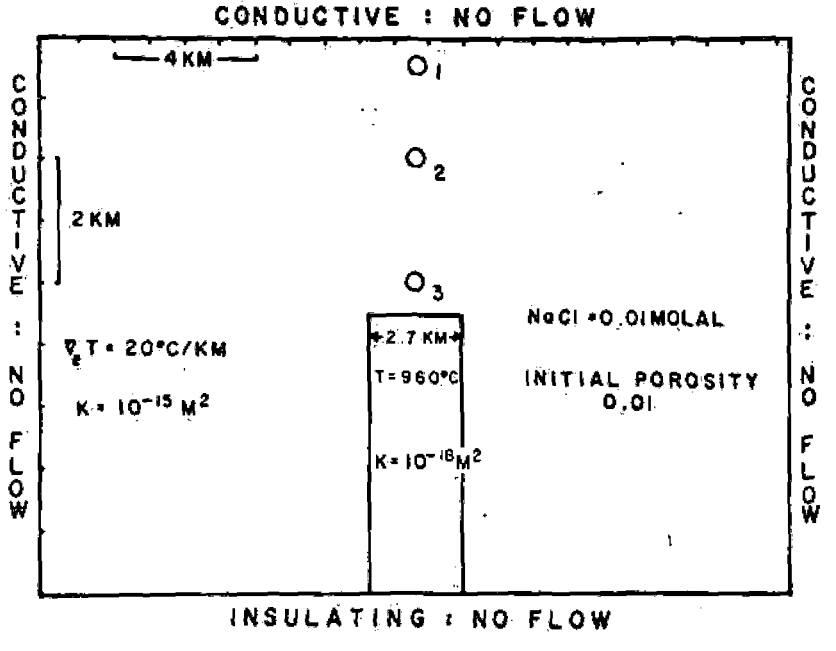
CONDUCTIVE : NO FLOW
4KM
O1
O2
O3
2KM
CONDUCTIVE : NO FLOW
CONDUCTIVE : NO FLOW
∇eT = 20°C/KM
K = 10⁻¹⁵ M²
2.7 KM
T = 960°C
K = 10⁻¹⁸M²
NaCl = 0.01MOLAL
INITIAL POROSITY 0.01
INSULATING : NO FLOW

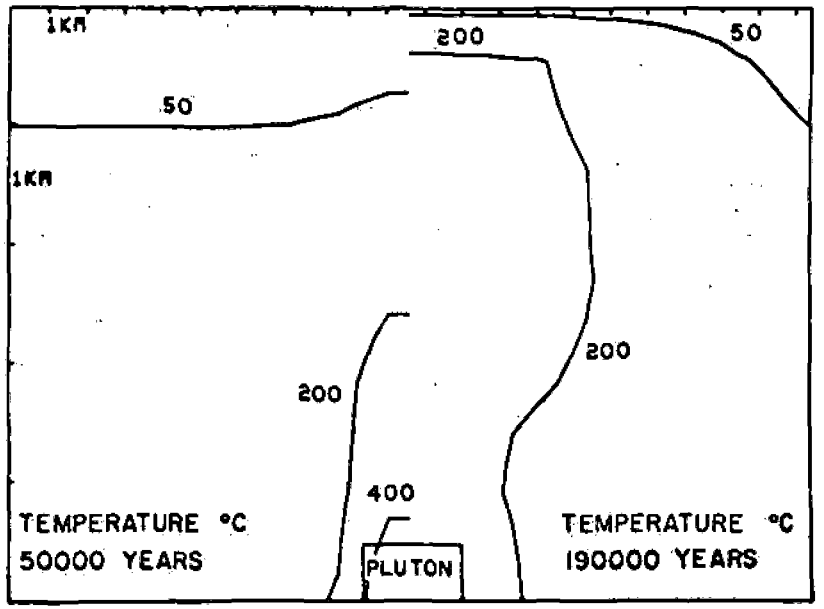
1KM
200
50
50
1KM
200
200
400
PLUTON
TEMPERATURE °C
50000 YEARS
TEMPERATURE °C
190000 YEARS

5

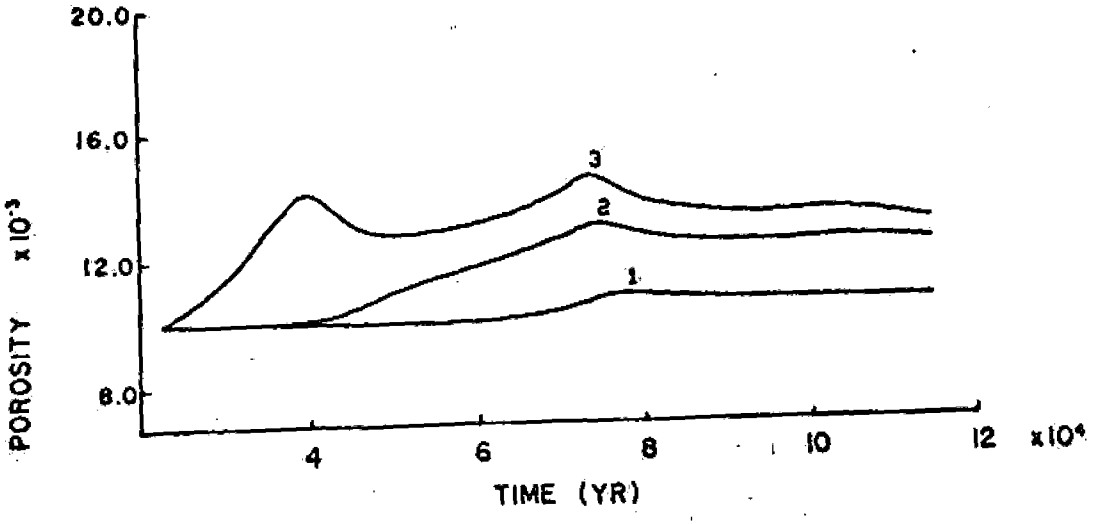
20.0
16.0
12.0
8.0
POROSITY x10⁻³
3
2
1
4
6
8
10
12 x10⁴
TIME (YR)

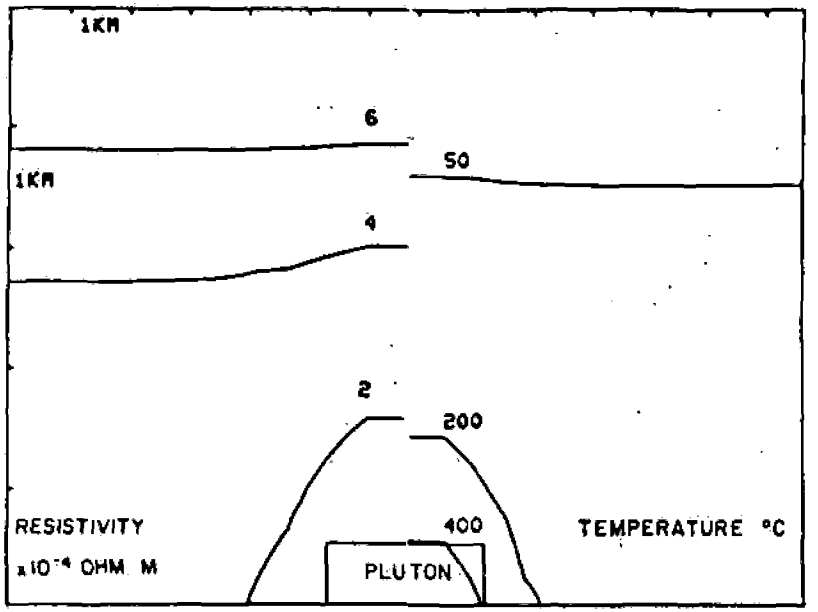
1KM
6
50
1KM
4
2
200
400
RESISTIVITY
x10⁻⁴ OHM M
PLUTON
TEMPERATURE °C

50000 YEARS

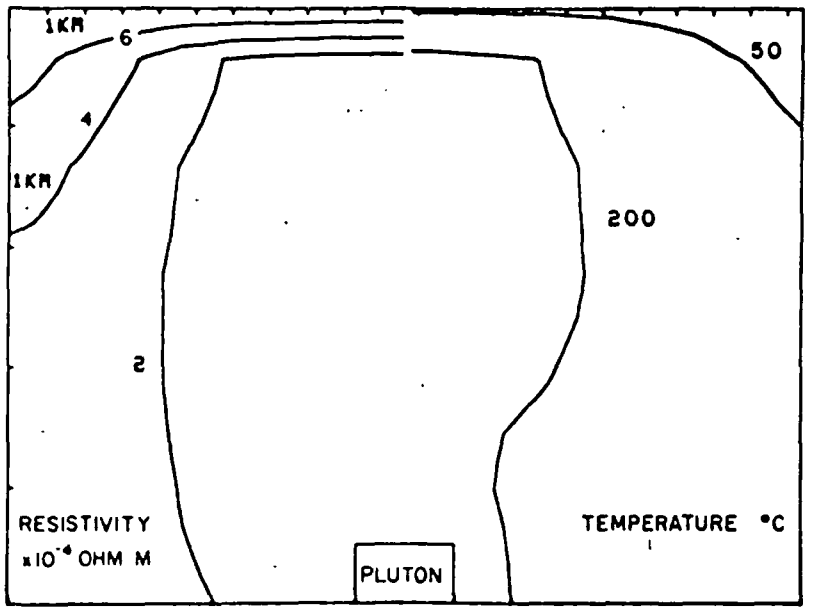

1.9 x 10^5 YEARS

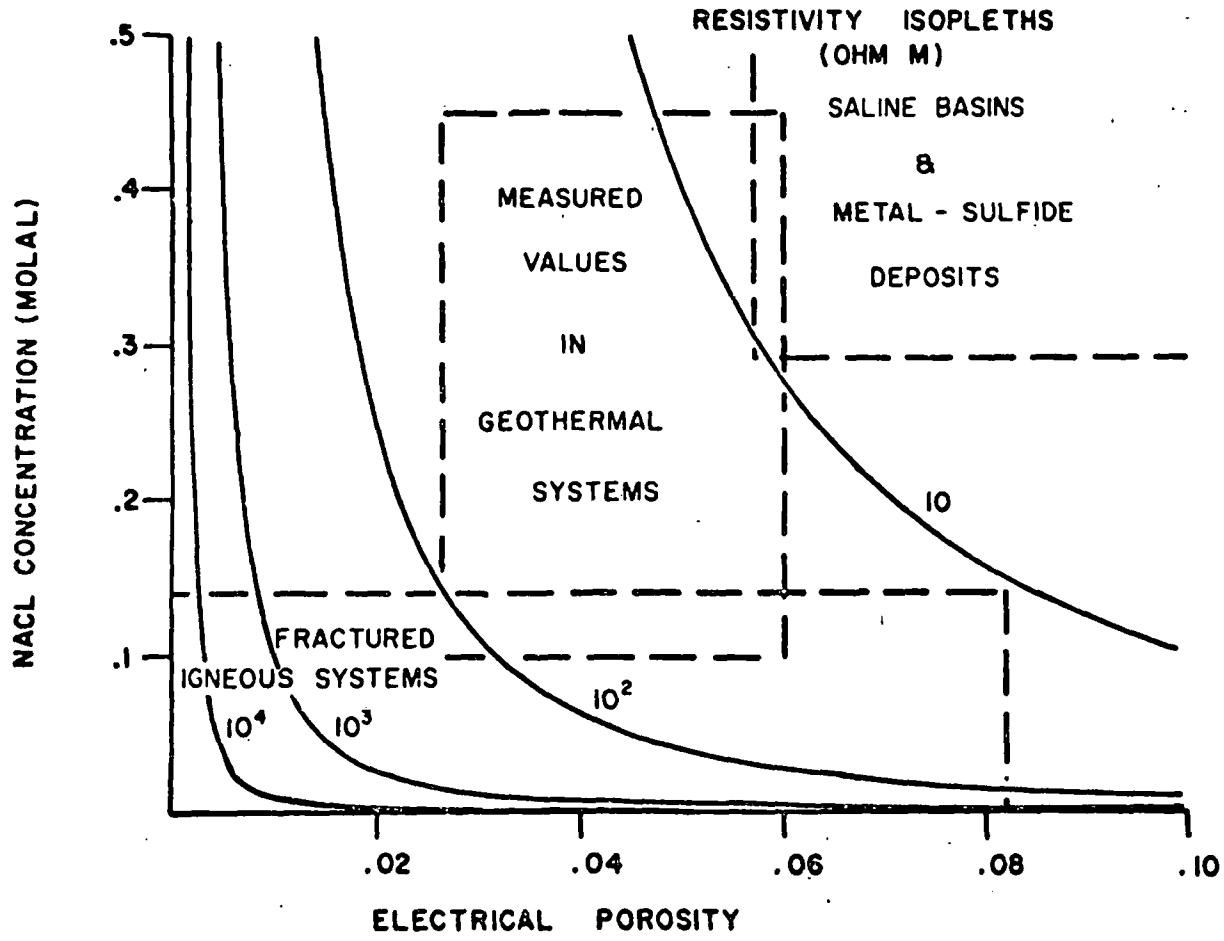
RESISTIVITY ISOPLETHS
(OHM M)
SALINE BASINS
&
METAL - SULFIDE
DEPOSITS
MEASURED
VALUES
IN
GEOTHERMAL
SYSTEMS
FRACTURED
IGNEOUS SYSTEMS
10
10²
10³
10⁴
.5
.4
.3
.2
.1
.02
.04
.06
.08
.10
NACL CONCENTRATION (MOLAL)
ELECTRICAL POROSITY

9

A PRELIMINARY ANALYSIS OF INTRINSIC FLUID AND ROCK RESISTIVITY IN ACTIVE HYDROTHERMAL SYSTEMS

B. Moskowitz and D. Norton

Department of Geology and Geophysics, University of Minnesota, Minneapolis, Minnesota 54421
Department of Geosciences, University of Arizona, Tucson, Arizona 85721

Abstract. Electrical resistivity data are utilized in interpretations of subsurface envitonments and to explore for geothermal and mineral resources. Abnormally low resistivity data are alternatively interpreted to indicate the presence of high-temperature fluids or conductive minerals (metal sulfides) at depth, even though relative contributions of thermal, porosity, and fluid composition effects appear to be poorly known. An analysis of intrinsic rock resistivities, calculated electrical porosities, and two-dimensional heat and mass transfer computations indicates that the host rock resistivity distribution around igneous intrusives is directly related to the mode of dispersion of thermal energy away from the pluton. Comparisons between numerical results and field observations in geothermal areas indicate that resistivity values in the vicinity of thermal anomalies are a complex function of fluid circulation patterns, fluid composition, and the distribution of conductive minerals produced by the reaction between circulating fluids and rocks; therefore in many cases, low near-surface resistivity anomalies cannot be entirely accounted for by hot circulating saline fluids, and observations of high thermal gradients associated with low-resistivity anomalies are not unique indications of a high-energy geothermal resource at shallow crustal depths.

Introduction

The nature of rocks in the upper crust is often deduced from apparent electrical resistivity data. The relationship between these data and the intrinsic resistivities is poorly known, and therefore correlation of the electrical resistivity measurement of rocks with variations in rock and pore fluid properties is usually speculative. Although interpretations are based on resistivity data measured in deep drill holes and laboratory measurements on rocks and fluids, the correlation of laboratory measurements, even in well-controlled laboratory experiments, with rock properties has not been satisfying. Better understanding of this correlation would facilitate mapping subsurface conditions with the aid of electrical survey data and is particularly relevant in regions of active hydrothermal activity, where there is considerable interest in energy resources.

The electrical resistivity variations in upper crustal rocks have been inferred from various electrical methods. The results of these surveys indicate that average resistivity values in stable crustal regions range from 10^5 to 10^2 ohm m [Keller and Frischknecht, 1966; Keller et al., 1966]. An analysis of laboratory experimental data on the resistivity of fluid-saturated crustal rocks coupled with considerations of regional heat flow data predict similar ranges in resistivity to a 40-km depth [Brace, 1971]. Resistivity surveys in regions of geothermal activity indicate anomalously low resistivities, which range between 10 and 100 ohm m [Sato, 1970; Cheng, 1970; Risk et al., 1970; Zohdy et al., 1973; Keller, 1970]. These anomalous values are often attributed to the presence of prospective thermal energy resources.

The properties and conditions in geothermal systems which contribute to resistivity values are fluid and mineral composition, porosity, temperature, and pressure [Brace, 1971; Brace and Orange, 1968; Brace et al., 1965; Keller and Frischknecht, 1966]. The effect of porosity and fluid resistivity on the bulk rock resistivity of sedimentary rocks was deduced by Archie [1942] and extended to crystalline rocks by Brace et al. [1965]. The empirical relationship derived by Archie defines bulk rock resistivity ρ_r as

$$\rho_r = a\rho_f\phi^{-n} \qquad (1)$$

in terms of pore fluid resistivity ρ_f, a proportionality constant a, porosity ϕ, and a factor which depends on the degree of rock consolidation, n. Experimental data by Brace et al. [1965] and Brace [1977] suggest that for fractured media, a = 1 and n = 2, values which apparently agree with theoretical electrical network models of Greenberg and Brace [1969] and Shankland and Waff [1974]. The porosity value normally used in (1) is that of total rock porosity. However, only those pores which contribute to current flow should be included in this term, and in fractured media the total porosity is usually not totally composed of interconnected pores, as is indicated by studies of ion transport in these types of rocks [Norton and Knapp, 1977]. Ranges in rock resistivity of 6 orders of magnitude may be realized for reasonable variations in the abundance of interconnected pores in fractured media [Moskowitz, 1977].

The transient thermal history of rocks in hydrothermal systems related to cooling igneous bodies has been simulated, over large regions and for long time periods, by numerical methods [Norton and Knight, 1977]. Since the variation in resistivity of rocks relates directly to subsurface temperature and pressure conditions, their numerical models provide a basis with which to analyze intrinsic resistivity of hydrothermal systems. The purpose of this communication is to present the results of a first-order approximation to the nature of intrinsic resistivity in such systems. The study considered variations in permeability and porosity, heat sources, rock and fluid properties, including variation in pore fluid resistivity as a function of temperature, pressure, and concentration of components in solution, as well as the time

Paper number 7B0809.

dependence of these parameters in a two-dimensional domain.

Porosity

The distribution of porosity in the crust varies in response to changes in pore fluid pressure. Effective pressure P_e is the difference between confining pressure P_c and pore fluid pressure P_f:

$$P_e = P_c - P_f \tag{2}$$

The variation of effective pressure with depth in the crust shows that in many geologic environments, increases in pore fluid pressure, as a result of temperature increases, will cause the effective pressure to decrease [Knapp and Knight, 1977]. As a consequence of the low tensile strength of rocks, when effective pressure is reduced to zero, the rock will fracture. Thus an increase in porosity is expected at zero effective pressure.

The total porosity in fractured media may be represented by

$$\phi = \phi_F + \phi_D + \phi_R \tag{3}$$

where ϕ_F, the effective flow porosity represents those pores through which the dominant mode of fluid and aqueous species transport is by fluid flow, ϕ_D, the diffusion porosity, represents those pores through which the dominant mode of transport is by diffusion through the aqueous phase, and ϕ_R, the residual porosity, represents those pores not connected to ϕ_F or ϕ_D. Field observations and experimental studies indicate that ϕ_R apparently accounts for more than 90% of the total porosity observed in crystalline rocks at ambient conditions [Norton and Knapp, 1977]. Our studies indicate that when ϕ_R values are used in (1), intrinsic resistivities of saturated rocks are predicted reasonably well, whereas ϕ_F and ϕ_D predict values many orders of magnitude higher than observed values [Moskowitz, 1977].

The correlation between porosity values consistent with electrical diffusivity and ion diffusivity determined by Norton and Knapp [1977] is unclear. We have assumed that pore fluid thermal expansion in residual pores produces fractures which contribute to electrical porosity. The pore characteristics at which the fluid will simply flow from the pore in response to thermal expansion and not increase the porosity are considered to be typical of the flow porosity normally found in crystalline rocks. Therefore any increases in total porosity due to temperature occur approximately as the result of changes in residual porosity. These assumptions are justified by the fact that $\phi_R \simeq 0.9\phi$ and that ϕ is used in Archie's law. Residual porosity is certainly an upper limit to the actual electrical porosity of crystalline rocks, and subsequently, the intrinsic resistivity calculated from these assumptions represents minimum values. Also, conversion of residual porosity to flow or diffusion porosity which relates directly to permeability is not considered in the fluid flow models to be discussed below.

The concept presented by Knapp and Knight [1977] can be used to relate porosity change at zero effective pressure to temperature. The total derivative of the rock-pore volume at constant composition is

$$dV = \left(\frac{\partial V}{\partial T}\right)_P dT + \left(\frac{\partial V}{\partial P}\right)_T dP \tag{4}$$

where $V = V_r + V_f$, V_r is rock volume, and V_f is pore volume. The coefficients of isobaric thermal expansion α and isothermal compressibility β for the bulk rock are defined as

$$\alpha \equiv \frac{1}{V}\left(\frac{\partial V}{\partial T}\right)_P \tag{5a}$$

$$\beta \equiv -\frac{1}{V}\left(\frac{\partial V}{\partial P}\right)_T \tag{5b}$$

Substitution of (5a) and (5b) into (4) defines the total volume change in terms of α and β:

$$dV = V\alpha\, dT - V\beta\, dP \tag{6}$$

This total derivative can also be expressed in terms of the individual thermal expansions and compressibilities of pore fluid and rock:

$$dV = [V_f\alpha_f + V_r\alpha_r]\, dT - [V_f\beta_f + V_r\beta_r]\, dP \tag{7}$$

However, when rocks fracture as a consequence of pore fluid expansion, infinitesimal increases in pore fluid pressure will produce further fracturing. Therefore $dP \cong 0$, and (7) may be simplified to

$$dV = [V_f\alpha_f + V_r\alpha_r]\, dT \tag{8}$$

Typical values for α_r, for common silicate minerals, over a temperature range of 0°-800°C, are of the order of 10^{-6} °C^{-1} [Clark, 1966]. The thermal expansion coefficient for pure water, over the same temperature span, is of the order of 10^{-3} °C^{-1}. As long as pore volume V_f is greater than or equal to 0.01, $V_f\alpha_f >> V_r\alpha_r$, and (8) becomes

$$dV = V_f\, \alpha_f\, dT \tag{9}$$

The total volume change, according to (9), occurs as a result of pore volume changes, the rock volume remaining essentially constant. Rearranging (9) with the approximation that $dV \simeq dV_f$ yields an integral equation relating pore volume and temperature:

$$\int_{V_f^o}^{V_f} \frac{dV_f}{V_f} = \int_{T_b}^{T} \alpha_f(T)\, dT \tag{10}$$

In (1), V_f^o is the initial residual pore volume, and T_b is the temperature at which the rock fractures. Integrating (10) gives the pore volume as a function of temperature:

$$V_f = V_f^o \exp \left[\int_{T_b}^{T} \alpha_f(T)\, dT\right] \quad (11)$$

where $T > T_b$. The initial residual porosity ϕ_R^o is defined as

$$\phi_R^o = \frac{V_f^o}{V^o} = \frac{V_f^o}{V_r + V_f^o} \quad (12)$$

and the fluid and rock volumes are

$$V_f^o = \phi_R^o V^o \qquad V_r = (1 - \phi_R^o)V^o \quad (13)$$

respectively. Substituting (12) and (13) into (11) defines a porosity temperature function in terms of the initial residual porosity:

$$\phi_R = \frac{\phi_R^o F(T)}{(1 - \phi_R^o) + \phi_R^o F(T)} \quad (14)$$

where

$$F(T) = \exp \left[\int_{T_b}^{T} \alpha_f(T)\, dT\right] \quad (15)$$

For the purposes of this discussion we will consider that (14) defines increases in the effective electrical porosity. That is, all porosity increases due to thermal effects are assumed to contribute to increased electrical current flow in the rocks.

The temperature at which the rocks initially fracture, T_b, may be defined as

$$T_b = T_a + \Delta T \quad (16)$$

where T_a is the ambient temperature and ΔT is the temperature increment necessary to reduce effective pressure to zero. The value of ΔT depends on the geothermal gradient, and the maximum value of ΔT along a gradient of 20°C/km is 20°C [Knapp and Knight, 1977].

Porosity, defined by (14), was computed for depths of 1, 2, 3, and 4 km below the earth's surface (Figure 1). At a depth of 1 km and initial temperature of 40°C, large increases in porosity are predicted for temperature changes of the order of 300°C. However, the porosity increases are small for changes in temperatures of less than 100°C at this same depth. At greater depths, e.g., 4 km, much smaller increases in porosity are predicted for these same temperature conditions, owing to increased confining pressure.

The relationship among bulk rock resistivity, fluid resistivity, and electrical porosity is

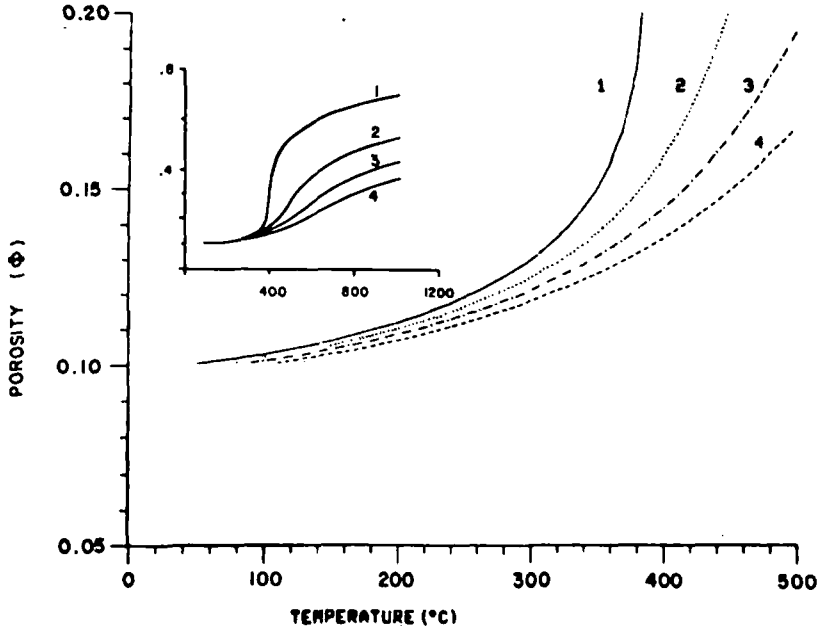

Fig. 1. Porosity as a function of temperature at depths of 1, 2, 3, and 4 km, as computed from (14). Initial porosity ϕ_o is 0.1, and background temperatures are consistent with a surface temperature of 20°C and a temperature gradient of 20°C/km. Pressures were computed for a rock density of 2.75 g/cm^3. Insert shows porosity values consistent with temperatures up to 1200°C.

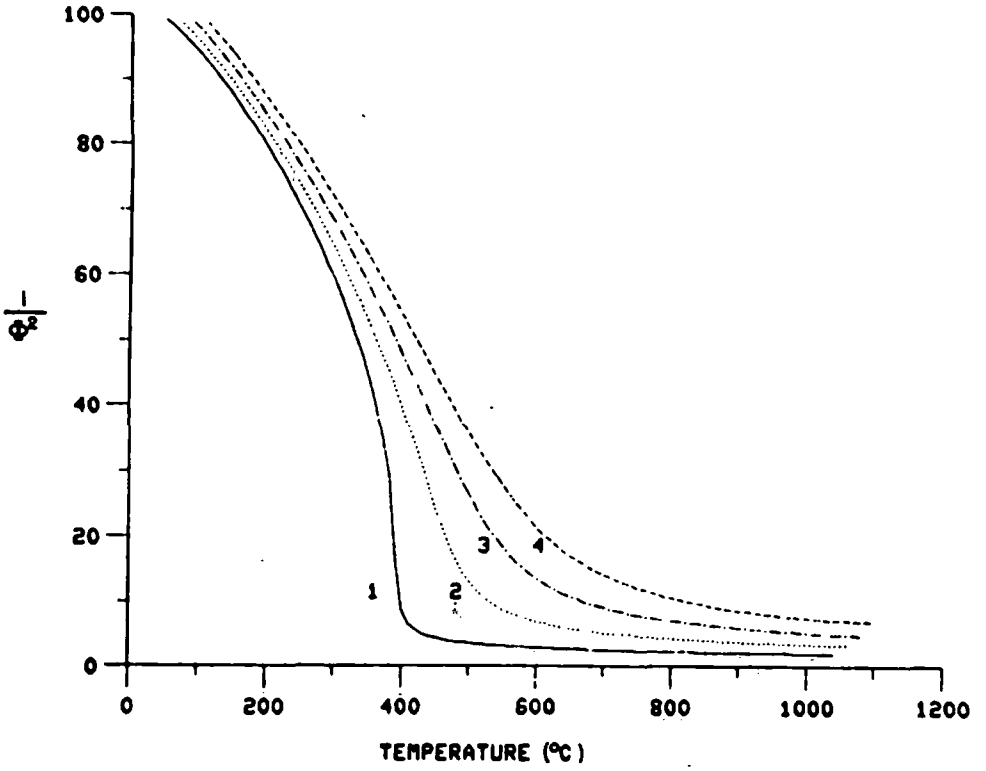

Fig. 2. Parameter ϕ^{-2} as a function of temperature at depths of 1, 2, 3, and 4 km. Parameters used are same as those in Figure 1.

poorly known. Archie's law, equation (1), has been assumed as an adequate first approximation to rock resistivity. Therefore the important parameter in predicting resistivity from (1) is ϕ^{-2}, and therefore small increases in porosity will result in a significant decrease in ρ_R (Figure 2).

Fluid Resistivity

The resistivity of natural groundwaters varies as a function of temperature, pressure, and composition. Since the dissolved constituents in natural waters are often dominated by sodium and chloride, and the resistivity values of NaCl-H_2O fluids are similar, within a factor of 2.5, to those of other common fluids, the compositional effects of fluid resistivity are approximated by the system NaCl-H_2O [Quist and Marshall, 1968; Chambers, 1957; Gunning and Gordon, 1942]. The variation in resistivity of a 0.1 m NaCl solution with temperature and pressure exhibits a steady, pressure independent decrease in resistivity to approximately 300°C, then an order of magnitude increase to 12 ohm m at 500°C and 500 bars (Figure 3). As can be seen, the dominant pressure effect is to shift the resistivity minimum to higher temperatures with increasing pressure. Increasing the NaCl concentration results in a decrease in resistivity that varies from 100 to 0.01 ohm m for concentrations ranging from 10^{-4} to 2 m.

Fluid temperatures in geothermal reservoirs range up to 300°C, and pressures to 1 kbar. Total ionic strength of these fluids ranges from 1 m, such as was observed in the Imperial Valley system [Meidav and Furgerson, 1972] to 10^{-2} m, such as was observed in the Broadlands, New Zealand, system [Browne and Ellis, 1970]. Typical resistivities of geothermal reservoir fluids range from 0.01 to 10 ohm m [Cheng, 1970], which is similar to the range in resistivity of pore fluids in a variety of geologic environments [Keller and Frischknecht, 1966].

Temperature-Pressure Distribution

Notions of temperatures and pressures in geothermal systems are primarily derived from production or exploration wells, and consequently, information is restricted to small portions of the total system. Knowledge of these parameters over the entire hydrothermal system is necessary in order to analyze the time dependence of resistivity in the region of a cooling pluton. Simulation of cooling plutons by numerical methods is one method by which these parameters can be defined for an idealized geothermal system.

Fluid flow caused by thermal anomalies related to igneous plutons is effectively scaled and represented in two dimensions by partial differential equations which describe the conservation of mass, momentum, and energy for the fluid-rock system [Norton and Knight, 1977]:

Conservation of energy

$$\gamma \frac{\partial T}{\partial t} + q\nabla H = \nabla \cdot \kappa \nabla T \qquad (17)$$

Conservation of momentum

$$\nabla \cdot \frac{\nu}{k} \nabla \Psi = R \frac{\partial \rho}{\partial y} \qquad (18)$$

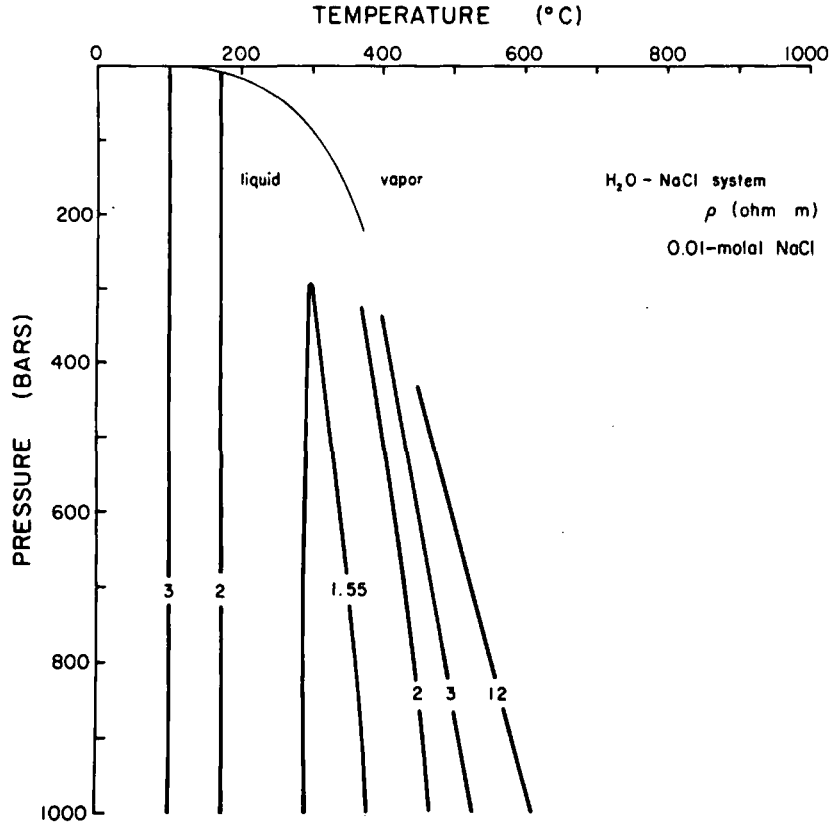

Fig. 3. Temperature-pressure projection of the two-phase surface (liquid and vapor) in the H_2O-NaCl system at 0.01-m NaCl concentration depicting fluid resistivity isopleths.

where T is the temperature, Ψ is the stream function, q is the fluid flux, t is the time, H, ρ, and ν are the enthalpy, density, and viscosity of the fluid, k is the permeability of the rock, κ is the thermal conductivity, and γ is the volumetric heat capacity of the fluid-saturated media, R is the Rayleigh number, ∇ is the gradient operator, and y is the horizontal distance in the two-dimensional section to which these equations apply.

Equations (17) and (18) are approximated by finite difference numerical equations which permit computation of the values of the dependent variables at discrete points in the domain from initial and boundary values specified for the system. The numerical analysis provides the option to include variable transport properties of the fluid (H_2O system) and rock, general boundary and initial conditions, and radioactive and volumetric heat sources in a two-dimensional domain. The transport process related to the transient thermal anomaly is approximated by a time sequence of steady state numerical solutions to (17) and (18), computed at explicitly stable time intervals. An alternating direction implicit finite difference method is used to approximate the spatial derivatives at discrete intervals of the order of 0.1-0.5 of the system height. Fluid pressure in the system is computed at each steady state step by integration of Darcy's law, in which the fluid properties, viscosity and density, are expressed as a function of temperature and pressure.

The methods used by Norton and Knight [1977] were used to define the temperature variation in the environment of a cooling pluton as a function of time. The hypothetical system is characterized by a dominance of convective heat transport over conductive heat transport as a result of relatively large host rock permeabilities (Figure 4). As a consequence of fluid circulation the temperature distribution in the host rocks evolves into a plumose pattern at $\sim 10^5$ years (Figure 5) and results in broad regions of uniform temperature above the pluton.

Initial temperatures in the host rocks at this depth are 110°C, as defined by the 20°C/km geothermal gradient and 20°C surface temperature. At 190,000 years after pluton emplacement the 200°C isotherm is at approximately a 0.5-km depth (Figure 5), and the temperatures between the top of the pluton and the 200°C isotherm have increased by at least 90°C. The pore fluid resistivity reaches a minimum at temperatures between 200°C and 300°C (Figure 3), and the porosity increase defined by (14) is of the order of 15% of the initial value for temperature increases of 100°-200°C. Therefore the zone between the 200°C isotherm and the top of the pluton in the system will be characterized by maximum porosity increase and the maximum decrease in pore fluid resistivity.

Porosities in host rocks at depths of <2 km directly over the pluton have significantly increased approximately 20% of the initial value at 190,000 years after pluton emplacement. This porosity increase persists uniformly to a 4-km depth. Time variations in porosity, calculated

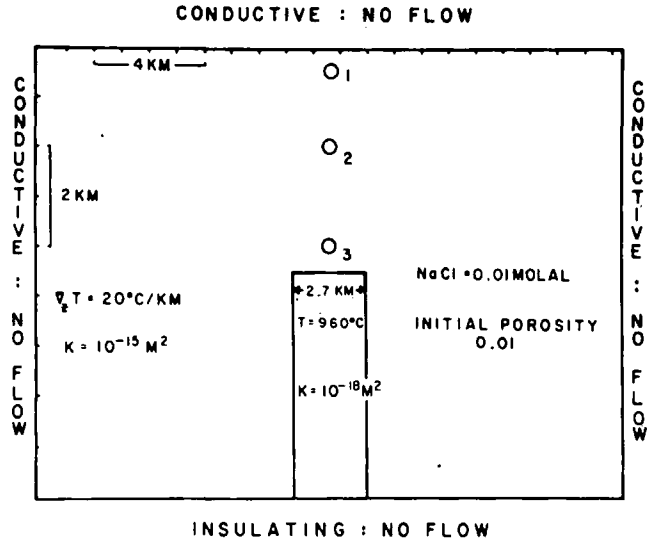

Fig. 4. Two-dimensional cross section of a pluton intruded into uniform permeability host rocks depicting initial and boundary conditions for numerical simulation of heat and mass transfer. Domain was discretized into 120 grid points such that Δz = 0.9 km and Δy = 1.75 km. The initial conditions include a background temperature consistent with a surface temperature of 20°C and a thermal gradient $\nabla_z T$ = 20°C/km. The pluton's initial temperature is 960°C. Permeabilities are 10^{-15} m^2 and 10^{-18} m^2 for the host and pluton rocks, respectively.

at fixed points 4, 2.5, and 0.5 km above the top of the pluton, predict a maximum 0.5 km above the pluton at 4 x 10^4 and 10^5 years after emplacement (Figure 6). However, as a result of convective transport of thermal energy to the surface a porosity maximum is observed at depths of <2 km.

The spatial and temporal distribution of temperature in the system will directly determine the host rock resistivity distribution. The resistivity isopleths closely parallel the isotherms at 50,000 and 190,000 years (Figures 7 and 8, respectively), which also illustrate the displacement in the resistivity isopleths between 50,000 and 190,000 years. By 190,000 years the lateral extent of the isopleth displacement at a 1-km depth spans the entire width of the system (~22 km).

In summary, the calculations indicate that the dispersion of thermal energy away from a pluton will directly affect the host rock resistivity. When pluton emplacement is into permeable host rocks, significant decreases in resistivity between the surface and depths of <0.5 km are predicted. These resistivity values then persist uniformly in a vertical zone, extending from 0.5 km to approximately 4 km above the pluton by 190,000 years after pluton emplacement. The maximum decrease in resistivity is less than a factor of 10, as compared to surface values. The range in host rock resistivity is from 10^4 to 10^5 ohm m. These values are quite high with respect to values obtained on real rocks. However, our calculations only account for a conductive fluid in a nonconductive matrix.

Discussion

The temperature variations in hydrothermal systems account for changes in electrical porosity and electrical resistivity of pore fluids. Results of our analysis suggest that resistivity anomalies caused by thermal events are several times broader in extent than the thermal source, and the lateral resistivity gradients at the margins of the anomaly are much lower than the vertical resistivity gradients directly above the pluton. The side and top margins of the resistivity anomaly correspond closely to the 200° isotherm, as a consequence of the fluid properties. A resistivity minimum occurs at relatively shallow depths, e.g., 0.5 km, and extends to 4 km. However, the magnitude of these resistivities is considerably greater than values measured in geothermal systems.

The magnitude of ρ_R is defined by the pore fluid concentration and initial host rock porosity, while the distribution of ρ_R is defined by the temperature distribution. To determine the change in magnitude of ρ_R, due to varying molality of pore fluids and host rock porosities, a series of calculations was made with different initial values of porosity and NaCl molalities. The isopleths of resistivity as a function of porosity and NaCl molality at constant temperature are defined by (1) and shown for T = 300°C in Figure 9. The results of the calculations summarized as the minimum resistivities predicted for the cooling pluton environment are comparable to actual values realized in geothermal systems and in saline groundwater systems. In order to explain the observed resistivities in geothermal areas (<10 ohm m), high-molality pore fluids and/or high-porosity host rocks must occur for large vertical and horizontal zones within the geothermal system.

The results of this study indicate that rock resistivities characteristic of active hydrothermal systems are considerably less than can be accounted for by simple changes in fluid resistivity or rock porosity. The discrepancies be-

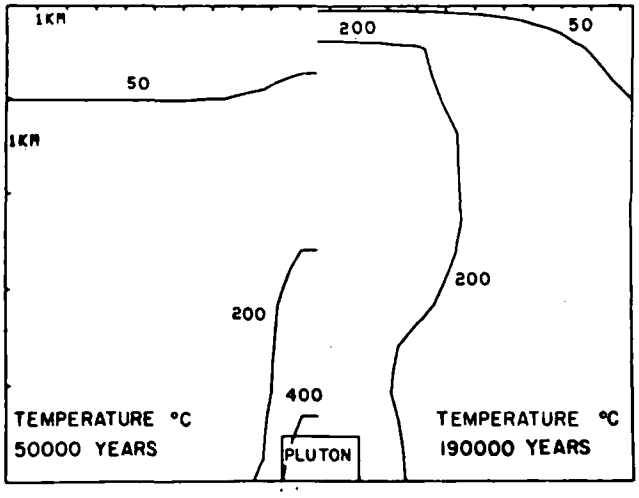

Fig. 5. Temperature distribution in an idealised hydrothermal system, defined by Figure 4, for (left) 5 x 10^4 and (right) 1.9 x 10^5 years elapsed time.

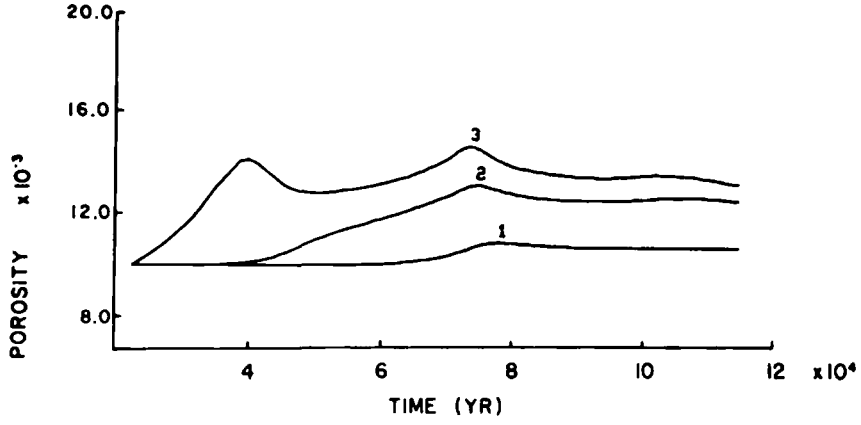

Fig. 6. Porosity as a function of time resulting from thermal energy transport into host rocks from the pluton at positions directly over the pluton, 0.5, 2, and 4 km below the surface (Figure 4).

tween the numerical resistivity models and the field resistivity observations in geothermal systems may be accounted for by the presence of conducting minerals, since pyrite and conductive clay minerals are typically found in the region of hydrothermal systems over the top of the thermal anomaly. If one uses a conservative estimate of a factor of 10 decrease in host rock resistivities resulting from conducting minerals, a geologically reasonable range in porosity and fluid composition can produce the anomalously low resistivity values observed in geothermal areas. Therefore except in anomalously high salinity and high porosity environments the presence of hot fluids alone is not sufficient to generate the low resistivity values observed in geothermal areas.

Considerable interest has been given to exploration techniques that might be useful in detecting high-energy geothermal systems. Commonly used techniques include measurements of heat flow and electrical resistivity. High heat flow in combination with anomalously low electrical resistivity data have been used as a justification for drilling of exploratory wells. Sedimentary basins and young, old, and mature geothermal systems in fractured rocks constitute a set of geologic environments within which the correlation of high thermal gradients, low near-surface resistivities, and surface thermal effects may lead to nonunique interpretations of the potential for geothermal energy resources at moderate depths. In the basin and range province of the western United States, concentrated brines associated with evaporite deposits in the high-porosity basins can produce lateral density gradients which cause fluid circulation. Exothermal hydration reactions that produce local thermal anomalies, coupled with the fluid circulation, are often sufficient to cause high surface heat flux and surface thermal springs. The high salinity and high porosity in these sedimentary basins would result in anomalously low near-surface resistivity. This particular environment appears

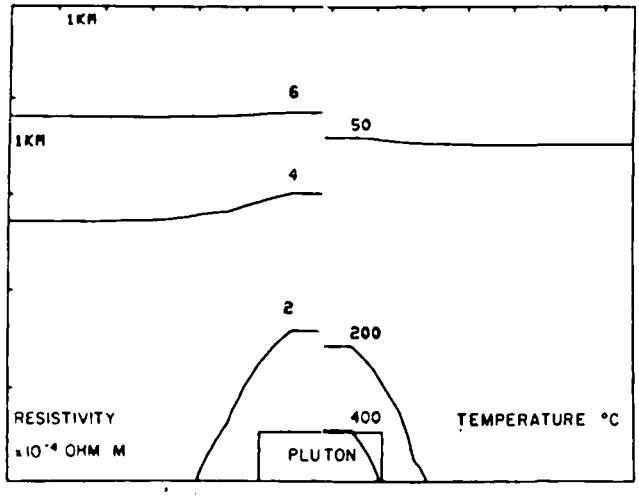

Fig. 7. Resistivity and temperature values in a hydrothermal system at 5 x 10^4 years elapsed time, depicting the temperature control on intrinsic resistivities.

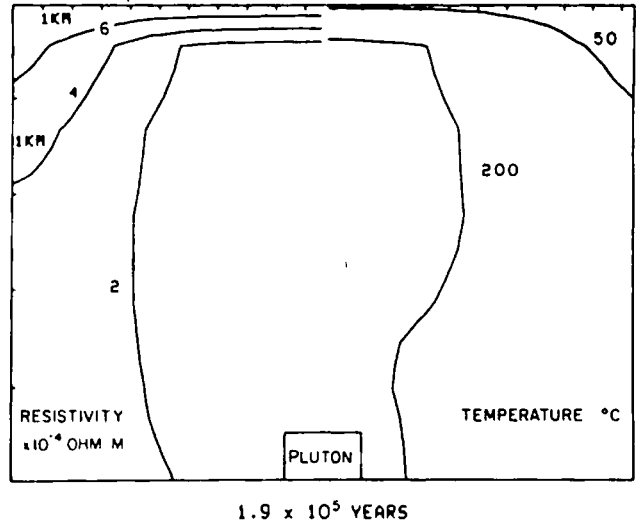

Fig. 8. Resistivity and temperature values in a hydrothermal system at 1.9 x 10^5 years elapsed time, depicting the temperature control on intrinsic resistivities.

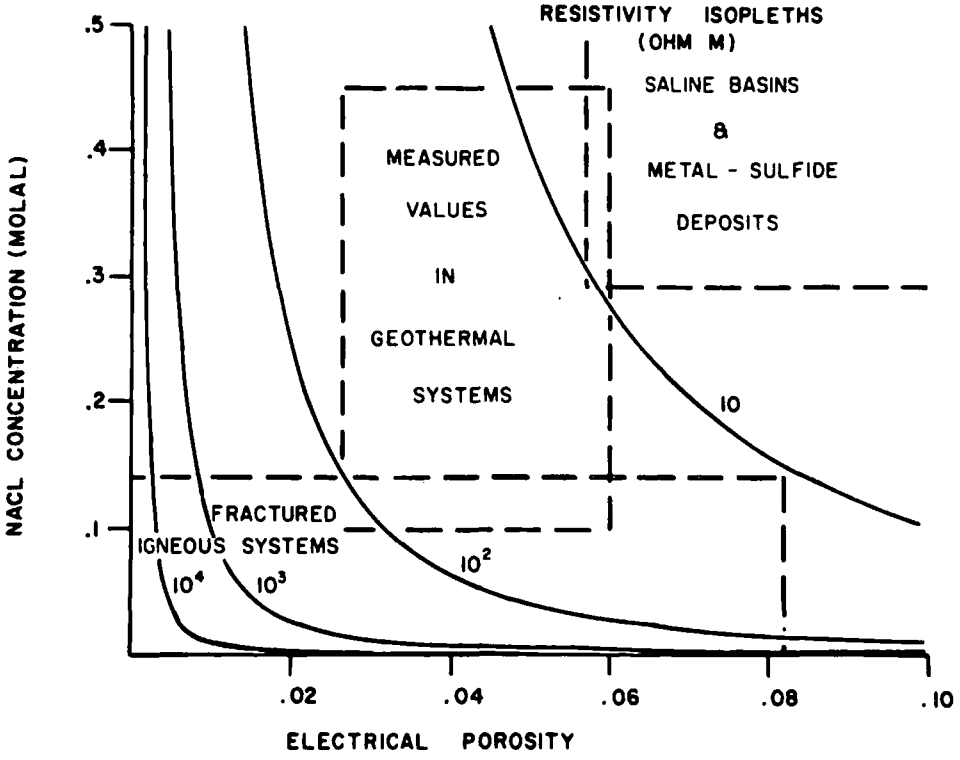

Fig. 9. Concentration of NaCl in pore fluids and electrical porosity effect on intrinsic rock resistivities, with isopleths of 10, 10^2, 10^3, and 10^4 ohm m. Values are for T = 300°C, at which the minimum in fluid resistivity occurs, and for P = 500 bars. Note that the minimum in fluid resistivity is nearly independent of pressures (Figure 3). Regions delimited by dashed lines represent ranges in values of porosity and fluid compositions observed in the respective geologic environments and for idealised systems considered in this study. The latter are labeled 'fractured igneous systems.'

to occur in the Safford Basin, southeastern Arizona [Norton et al., 1975].

Geothermal systems which have nearly cooled to regional background temperatures may be characterized by large conductive heat fluxes [Norton, 1977] as a result of remnant thermal energy that has been transported from the heat source to near-surface environments. Conducting minerals will undoubtedly have been formed above the pluton, and thermal springs will still be prevalent on the surface. In this environment, low resistivity would be associated with the conducting minerals and, in part, with the circulating saline fluids.

Geothermal systems in their early stages of formation have not been studied; however, their characteristics have been numerically simulated. The transport of thermal energy away from a pluton may be rapid with respect to the mass flux of reactive components in solution to the surface. This means that hot saline fluids will dominate changes in host rock resistivities because not enough time has elapsed to produce significant quantities of conducting minerals. High heat flux and surface thermal effects will probably form relatively early in the life cycle of a geothermal system. The calculated resistivity values resulting from increased temperatures are anomalous with respect to background values but are relatively high (10^4-10^5 ohm m). Therefore this environment is characterized by high heat flux and thermal surface effects but probably an undetectable resistivity anomaly, even though there is a high-energy thermal source at depth.

Active, mature geothermal systems are abundant worldwide where high heat flux, thermal surface effects, and low resistivities are associated with a productive thermal source at depth. However, low-resistivity anomalies, <100 ohm m, are probably caused by the presence of conductive minerals which may be coincident with hot thermal fluids.

The four geologic environments presented serve to illustrate the problems which can be encountered in attempting to interpret near-surface resistivity anomalies. Also a combination of heat flux measurements, surface thermal effects, and low resistivity can be characteristic of both productive high-energy geothermal systems and unproductive low-energy geothermal environments. The observations are also manifested in that electrical methods are used in prospecting for both sulfide mineral deposits and thermal energy.

Acknowledgments. We wish to acknowledge the Energy Research Development Administration for support of this study through contract E-11-1-2763. We thank Robert F. Butler, R. Knapp, and J. Knight for discussions and penetrating questions, L. McLean for editing and typing the manuscript, and the University Computer Center personnel for their assistance.

References

Archie, G. E., The electrical resistivity log as an aid in determining some reservoir characteristics, Trans. AIME, 146, 54-62, 1942.

Brace, W. F., Resistivity of saturated crustal rocks to 40 km based on laboratory studies, in The Structure and Physical Properties of the Earth's Crust, Geophys. Monogr. Ser., vol. 14, edited by J. G. Heacock, pp. 243-257, AGU, Washington, D. C., 1971.

Brace, W. F., Permeability from resistivity and pore shape, J. Geophys. Res., 82, 3343-3349, 1977.

Brace, W. F., and A. S. Orange, Further studies of the effect of pressure on electrical resistivity of rocks, J. Geophys. Res., 73, 5407-5420, 1968.

Brace, W. F., A. S. Orange, and T. R. Madden, The effect of pressure on the electrical resistivity of water-saturated crystalline rocks, J. Geophys. Res., 70, 5669-5678, 1965.

Browne, P. R. L., and A. J. Ellis, the Ohaki-Broadlands hydrothermal area, New Zealand: Mineralogy and related geochemistry, Amer. J. Sci., 269, 97-131, 1970.

Chambers, J. F., The conductance of concentrated aqueous solutions of potassium iodide at 25°C and of potassium and sodium chlorides at 50°C, J. Phys. Chem., 62, 1136, 1958.

Cheng, W. T., Geophysical exploration in the Tatun volcanic region, Taiwan, Geothermics, Spec. Issue, 2 (1), 910-917, 1970.

Clark, S. P. Jr., ed., Handbook of Physical Constants, Geol. Soc. America, Mem. 97, New York, Revised edition.

Greenberg, R. J., and W. F. Brace, Archie's law for rocks modeled by simple networks, J. Geophys. Res., 74, 2099-2101, 1969.

Gunning, H. E., and A. R. Gordon, The conductance and ionic mobilities for aqueous solutions of K and NaCl at T = 15°C-45°C, J. Chem. Phys., 10, 1942.

Keller, G. V., Induction methods in prospecting for hot water, Geothermics, Spec. Issue, 2 (1), 318-332, 1970.

Keller, G. V., and F. C. Frischknecht, Electrical Methods in Geophysical Prospecting, Pergamon, New York, 1966.

Keller, G. V., L. A. Anderson, and J. I. Pritchard, Geological survey investigations of the electrical properties of the crust and upper mantle, Geophysics, 31, 1078-1087, 1966.

Knapp, R., and J. Knight, Differential thermal expansion of pore fluids: Fracture propagation and microearthquake production in hot pluton environments, J. Geophys. Res., 82, 2515-2522, 1977.

Meidav, T., and R. Furgerson, Resistivity studies of the Imperial Valley geothermal area, California, Geothermics, 1, 47-62, 1972.

Mitchell, B. J., and M. Landisman, Geophysical measurements in the southern great plains, in The Structure and Physical Properties of the Earth's Crust, Geophys. Monogr. Ser., vol. 14, edited by J. G. Heacock, pp. 77-95, AGU, Washington, D. C., 1971.

Moskowitz, B. M., Numerical analysis of electrical resistivity in hydrothermal systems, M.S. thesis, Univ. of Ariz., Tucson, 1977.

Norton, D., Fluid circulation in the earth's crust, in The Earth's Crust, Geophys. Monogr. Ser., vol. 20, edited by J. G. Heacock, in press, AGU, Washington, D. C., 1977.

Norton, D., and R. Knapp, Transport phenomena in hydrothermal systems: The nature of porosity, Amer. J. Sci., 277, 913-936, 1977.

Norton, D., and J. Knight, Transport phenomena in hydrothermal systems: Cooling plutons, Amer. J. Sci., 277, 937-981, 1977.

Norton, D., T. Gerlach, K. J. DeCook, and J. S. Sumner, Geothermal water resources in Arizona: Feasibility study, technical completion report, project A-054-ARIZ, Office of Water Res. and Technol., Tucson, Ariz., 1975.

Quist, A. S., and W. L. Marshall, Electrical conductances of aqueous sodium chloride solutions from 0°C to 200°C and at pressures to 4000 bars, J. Phys. Chem., 72, 684-703, 1968.

Risk, G. F., W. J. P. MacDonald, and G. B. Dawson, D. C. resistivity surveys of the Broadlands geothermal region, New Zealand, Geothermics, Spec. Issue, 2 (1), 287-294, 1970.

Sato, K., The present state of geothermal development in Japan, Geothermics, Spec. Issue, 2 (1) 155-184, 1970.

Shankland, T. J., and H. S. Waff, Conductivity in fluid-bearing rocks, J. Geophys. Res., 79, 4863-4868, 1974.

Zohdy, A. A. R., L. A. Anderson, and L. J. P. Muffler, Resistivity, self potential, and induced polarization surveys of a vapor-dominated geothermal system, Geophysics, 38, 1130-1144, 1973.

(Received March 15, 1977;
revised August 15, 1977;
accepted August 26, 1977.)

Reprinted from
Economic Geology
Vol. 73, 1978, pp. 21–28

Sourcelines, Sourceregions, and Pathlines for Fluids in Hydrothermal Systems Related to Cooling Plutons

DENIS NORTON

Abstract

Simulation of hydrothermal systems by numerical methods permits computation of the initial positions (sources) of all fluids in the system. The locus of these positions, which are sourcelines, defines an essential link between the theories of irreversible mass transfer and those of thermally driven fluid flow. The concept of a fluid sourceline is introduced to facilitate the quantitative description of the initial composition of fluids which ultimately circulate through rocks in the vicinity of hot plutons.

The mathematical definition of fluid sourcelines and pathlines for hydrothermal systems permits the quantitative prediction of the initial position and, hence, initial compositions of all fluids which circulate through rocks in the vicinity of an igneous intrusion and the variations in temperature, pressure, and rock type along flow paths and, hence, the changes in composition of the fluid as it flows from its source to a position of interest in the system.

Examples of fluid sourcelines, sourceregions, and pathlines defined for inert fluids in an idealized hydrothermal system indicate the predominant source of fluids flowing through permeable hot plutons is from host rock environments adjacent to and above the pluton. These sourceregions in two dimensions include rocks from a 50-km^2 region as far as 5.5 km away from a 2.7-km-wide and 4.5-km-tall pluton.

Introduction

FLUID convection appears to be a universal process related to igneous and volcanic activity in the upper crust. Furthermore, the flow of fluids from one geologic environment into another is suggested by observations of active geothermal systems (Lapwood, 1948; Elder, 1965; Wooding, 1957; Donaldson, 1962), stable-light isotope data (Taylor, 1974), gains and losses of major and minor components from host rocks, and changes in mineralogy (Meyer, 1950; Villas, 1975). Also, calculations which simulate interactions between fluids and rocks (Helgeson, 1970; Norton, 1971) and fluid convection around cooling plutons (Norton and Knight, 1977) indicate that thorough redistribution of large masses of fluids is a natural feature of these environments.

Fluids in the Wairakei geothermal system are estimated to have circulated through permeable rocks for distances of tens of kilometers during the active thermal history of this region (Elder, 1965; Grindley, 1965). Similarly, meteoric water circulation to depths of several kilometers is called upon to account for the oxygen isotope values measured in numerous plutons (Taylor, 1974). The circulation paths of meteoric water through various host rock environments, at moderate temperatures without significant isotopic changes, ultimately flow into many plutons, where exchange reactions result in the depletion of the ^{18}O content of the igneous rocks.

There are numerous references in the literature to rock alteration associated with plutons emplaced into both the upper continental and oceanic crusts; however, only a few typical examples are mentioned herein. Compositional and mineralogical changes in carbonate and noncarbonate rocks around plutons have been noted several kilometers away from the plutons (Cooper, 1957; Brown and Ellis, 1970), as well as in the plutons themselves (Nielson, 1968; Gustafson and Hunt, 1975). Extensive alterations of rock composition clearly occur as a consequence of the large masses of reactive fluids circulating through the rocks.

The simulation of rock alteration processes, using reasonable estimates of initial fluid compositions, further supports the concept of extensive fluid circulation and reactions between fluids and rocks in the temperature range from 25° to 350°C (Helgeson, 1970). Analogous studies of the circulation process have described the style of fluid motion (Wooding, 1957; Ribando et al., 1976; Norton and Cathles, in press; Henley, 1973) and have provided some notion of the masses of fluid in the hydrothermal systems. The description of actual fluid flow paths and effective fluid : rock ratios related to cooling plutons has provided quantitative heuristic models of these systems (Norton and Knight, 1977). The process of fluid circulation and concomitant reaction with rocks is, however, not well enough understood to enable ore deposit geologists either to test hypotheses regarding the sources of fluids and ore-forming com-

ponents or to predict the occurrence of subsurface ore deposits on the basis of limited surface or drill hole data.

The purpose of this communication is to describe the concepts that permit quantitative description of the sources and flow paths of inert fluids which circulate in the vicinity of cooling plutons. These concepts permit the quantitative description of the initial positions of all fluids which ultimately circulate through rocks in the vicinity of an igneous intrusion and the paths along which the fluids flow (including the temperature, pressure, and compositional variations of the path) from the fluid source to any position of interest in the system. Quantitative description of reactive circulation and mineral zoning in hydrothermal systems follows simply from the concepts presented below, when they are coupled with those of irreversible mass transfer between fluids and rocks (Helgeson, 1970). The sources and redistribution of the chemical components in reactive fluids will form the basis of a future communication.

Fluid Circulation around Cooling Plutons

Hydrothermal fluid flow is caused by lateral density perturbations in the fluids confined within the flow porosity of rocks. Fluid density anomalies resulting from thermal and concentration effects are relatively common in upper crustal rocks, especially the large thermal perturbations which occur in pluton environments. Therefore, it is reasonable to expect fluid circulation to be a characteristic feature of these environments, if the rock permeability is sufficiently large.

Fluid circulation in natural systems is not easily studied by direct observation since even the most thoroughly explored geothermal systems are a small sample of the total system and the duration of field studies represents only a small fraction of the time duration of the thermal anomalies. The lack of a quantitative understanding of fluid circulation is, therefore, not surprising.

However, the fluid flow in pluton environments can be effectively scaled and represented by partial differential equations which describe the conservation of mass, momentum, and energy for the fluid-rock system (Norton and Knight, 1977):

$$\gamma \frac{\partial T}{\partial t} + \bar{q} \cdot \bar{\nabla} \bar{H} = \bar{\nabla} \cdot \kappa \bar{\nabla} \bar{T}$$

(conservation of energy) (1)

and

$$\frac{\nu}{k} \bar{\nabla} \cdot \frac{\nu}{k} \bar{\nabla} \bar{\Psi} = R \frac{\partial \rho}{\partial y}$$

(conservation of momentum) (2)

where T is the temperature; Ψ the scalar streamfunction; $\bar{q}$ the fluid flux; H, ρ, and ν are the enthalpy, density, and viscosity of the fluid; k is the permeability of the rock; κ the thermal conductivity and γ the volumetric heat capacity of the fluid saturated media; R the Rayleigh number; t the time; ∇ the gradient operator; and y the horizontal distance in the two-dimensional section to which these equations apply. The conservation of mass is explicitly included in equations (1) and (2). Equations (1) and (2) are approximated by finite difference numerical equations which permit the computation of the values of the dependent variables at discrete points in the domain from the initial and boundary values specified for the system.

The physical meaning of equations (1) and (2) is apparent if one considers that the fluid density gradients, on the right-hand side of equation (2), resulting from a thermal anomaly cause fluid circulation; e.g., they define gradient values of the streamfunction and, therefore, fluid flux since $q_z = -\partial\Psi/\partial y$ and $q_y = \partial\Psi/\partial z$. The fluid flux, $\bar{q}$, in turn transports heat away from the thermal anomaly, i.e., the second term on the left of equation (1); at the same time, thermal energy is conducted away from the thermal anomaly, the right-hand side in equation (1). Both of these processes give rise to a decrease in temperature with respect to time and, therefore, decrease the horizontal fluid density gradients; and, consequently, the thermal anomaly is decreased by the combined convective and conductive heat transfer. The coupled solution of (1) and (2) is achieved by a series of steady-state computations at explicitly stable time steps, thereby defining the temperature and fluid flux as a function of time. The pressure is in turn computed at each steady-state step by integration of the Darcy equation,

$$\bar{q} = -\frac{k}{\nu}[\bar{\nabla P} + \rho \bar{g}], \qquad (3)$$

in which the fluid properties, ν and ρ, are expressed as a function of temperature and pressure, P, and the gravitational force vector, $\bar{g}$, is constant. Fluid velocities are then determined from

$$\bar{V} = \bar{q}/\rho. \qquad (4)$$

Numerical simulation of the equations quantitatively predicts the nature of hydrothermal fluid flow and provides the ore deposit geologist with a key to understanding how these processes operated in the past. The reliability of these computations and their applicability to specific locations is a direct function of the degree to which those parameters that affect heat and mass transport in the hydrothermal system (e.g., permeability, flow porosity, heat source geome-

try, and transport properties of the fluid and rock) are known. The permeability of fossil hydrothermal systems is poorly known and difficult to estimate but is requisite knowledge for understanding the ore-forming process. As a consequence of the inadequate data base, especially with regard to permeability, computer stimulation requires estimation of these data; numerical results are therefore obtained for geologically reasonable ranges of parameters. The reliability of the computations for a given set of transport parameters depends directly on the number of discrete points used and on the convergence and stability of the numerical algorithm.

Analysis of idealized pluton environments using the above procedure indicates that in systems where permeabilities are greater than 10^{-14} cm^2 convective fluid circulation accounts for 10 percent or more of the total heat transport. Permeabilities of this order are realized in fractured rocks where the fracture frequency is on the order of one fracture per meter and the fracture aperture is ~ 2 μm. The abundance of fractures commonly observed in pluton environments suggests that many of these rocks are host to extensive fluid circulation. The most significant aspect of these computer experiments for the subsequent discussion is that the fluid flux and velocity (of inert fluids, e.g., fluid approximated by the H_2O system) can be quantitatively determined for idealized pluton environments.

The Sourceline Concept in Hydrothermal Systems

Fluid velocities may be computed for thermal or solute perturbations that cause fluid flow in geologic systems for which rock permeabilities are known or can be estimated. These fluid velocities in turn permit the quantitative description of fluid pathlines. Consider a fluid packet of some arbitrary position in the system, then the fluid path is defined by

$$d\bar{l} = \bar{V}dt, \tag{5}$$

where $\bar{V}$ is the Darcy velocity and $d\bar{l}$ is the incremental distance along the path traveled during time interval, dt. Since the velocity is known as a function of time from equations (1), (2), and (4), equation (5) may be integrated for the *nth* such fluid packet during time interval $t - t_0$ in the system,

$$\bar{l}_n = \int_{t_0}^{t} \bar{V}_n(t)dt, \tag{6}$$

where $\bar{V}_n(t)$ is the average velocity of the *nth* particle during the discrete time interval Δt (Fig. 1). Along the *nth* such path, variations in temperature and pressure are also defined from the transport equations (1) and (2), and variations in the rock

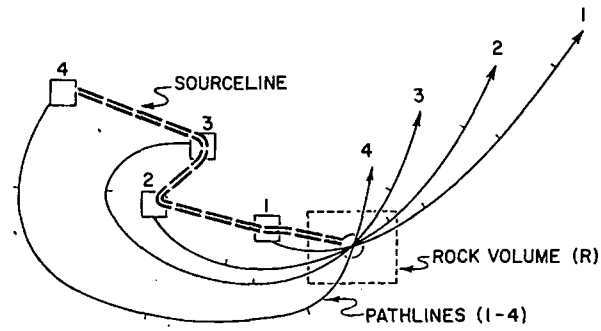

FIG. 1. A schematic of fluid pathlines and sourcelines. Pathlines are defined by equation (6) for $n = 4$ fluid packets where the box indicates the initial position, $\bar{l}_n = 0$, of each fluid packet at time $= 0$, and their respective positions are indicated by tic marks which represent equal elapsed times. The variation in distance between the tics along a pathline reflects the fluid velocity variations. The fluid packets flow sequentially through a common rock volume in this schematic example; however, this is a special case. The line connecting the original positions, boxes, of this special set of pathlines defines the fluid sourceline for the rock volume, R. The sourceline may be computed directly from equation (9) for $n = 4$. Note that the sourceline for the rock volume defines the fluid source, but the sourceline is significantly different from the paths followed by the fluids from their sources to the rock volume. Since tht simulation is computed in two dimensions, the rock volume has an arbitrary unit depth.

environment are determined by geologic data. Therefore, the reaction history of each fluid packet may be explicitly determined on the basis of its initial composition and subsequent flow path. However, as a packet moves from one position to another it flows through rocks which may have already reacted with fluid which flowed through earlier and probably altered the initial composition or mineralogy of the rock. This requires, then, a concept by which to simulate the flow-reaction processes at discrete points in the system instead of following the fluid circulation.

The concept of a fluid sourceline is introduced in order to study the circulation-reaction process with respect to fixed positions in the system. A fluid sourceline is the locus of points of all fluid packets whose pathline intersect a fixed position of interest in the system. Consider such a position in a rock volume, R (Fig. 1). The position vector $\bar{S}_{ij}$, of a fluid sourceline for this position is defined in terms of the individual fluid packet position vectors:

$$\bar{S}_{ij} = \bar{r}_i + [\bar{r}_{i+1} - \bar{r}_i]\xi_j, \quad \begin{matrix} 0 \le \xi_j \le 1 \\ i = 1, N-1 \end{matrix} \tag{7}$$

where $\bar{r}_i$ and $\bar{r}_{i+1}$ are the position vectors for the fluid packets at an initial time, t_0, which flow through the rock volume, and ξ_j is an interpolation factor which varies continuously from 0 to 1 as j increases. The individual vectors are in turn defined by equation (6), but since we are tracing back along the flow

path, the integration limits are reversed with respect to equation (6):

$$\bar{r}_i = \int_{t_i}^{t_0} \bar{V}_i(t)dt, \qquad (8)$$

where t_i is the time at which particle i was at the position of interest, R. The sourceline position vector in equation (7) becomes

$$\bar{S}_{ij} = \int_{t_i}^{t_0} [\bar{V}_i(t) + (\bar{V}_{i+1}(t) - \bar{V}_i(t))\xi_j]dt. \qquad (9)$$

The definition of a sourceline, for an arbitrary time interval prior to the end of a thermal event, follows directly from equation (9) (Fig. 1).

A fluid sourceline may be defined at each discrete point in the system at which the variation in fluid velocity is known for the elapsed time interval of interest. Since hydrothermal fluid velocities around cooling plutons typically vary over several orders of magnitude throughout the cooling event, sourcelines may accordingly be very sinuous lines.

Examples of Sourcelines and Pathlines

Fluid pathlines and sourcelines for a hydrothermal system in the region of a cooling pluton which was emplaced into a stratified permeable host rock environment have been calculated. Although the concept of sourcelines and pathlines is quite independent of extenuating geologic circumstances, the extension of this concept to natural systems is not. Therefore, the following example is merely a first approximation to nature. One natural analog to this system is the stratified host rock environment in southeastern Arizona that many plutons have intruded (Fig. 2A). The thermal history of this system, for a period of $\sim 2 \times 10^5$ years, has been simulated by the methods summarized above. The details of this analysis are thoroughly described in Norton and Knight (1977). Those aspects of the system relevant to this discussion are the initial and boundary conditions (Fig. 2B) and the time variation of the pluton permeability (Fig. 3). The fluid velocities computed at discrete time intervals permit the calculation of fluid pathlines and sourcelines of the inert fluid assumed to be in the system.

First we examine examples of pathlines in the system and the temperature-pressure variations encountered along the flow paths. Pathlines for fluid packets (Fig. 4), 1, which occurs in the relatively permeable rocks and is initially several kilometers away laterally and above the pluton, 2, which is adjacent to the pluton near the contact between low and high permeability rocks, and 3, which is adjacent to the pluton in the low permeability rocks near the pluton side contact and deep in the system,

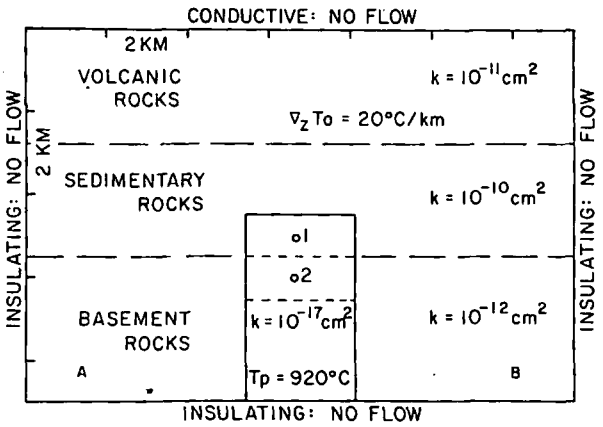

FIG. 2. A two-dimensional cross section of pluton environment. A. Hypothetical geologic units representing stratified host rocks around magma initially at 920°C. B. Initial and boundary conditions appropriate for an idealized system for which host rock permeabilities were assigned on the basis of estimates, Norton and Knapp (1977). The level of emplacement of the pluton was selected by an analog to Tertiary plutons which occur in southeastern Arizona. The bottom boundary conditions for flow and energy simulate decreases in permeability and increases in temperature with depth, and the conditions at the top of the system simulate conductive energy loss and no loss of fluid to surface hot springs. Side boundaries are selected for convenience and do not significantly affect the results discussed herein. Pluton permeability is 10^{-17} cm², or effectively zero, in order to represent an initially unfractured magma. The domain is symmetrical with respect to a vertical centerline through the pluton. The domain was discretized into 144 points for the numerical solution of equations, resulting in a spatial error on the order of 5 percent of the system height. Discrete time steps were computed such that the computations converge to within approximately ten percent of the true value defined by the differential equations.

are considered. The length and shape of these circulation paths are directly related to the spatial and temporal variation in the fluid velocities. The fluid

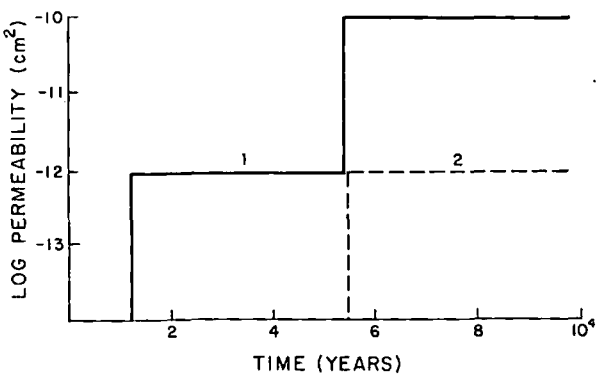

FIG. 3. Permeability variations with respect to time in the upper portion of the pluton, Figure 1, points 1 and 2. Values of $k = 10^{-11}$ cm² are equivalent to a millidarcy. Instantaneous permeability variations were used to simulate fracturing of pluton as it crystallizes and cools to below solidus temperatures, circa 800°C. These variations are in accord with the observation that plutons in these types of systems are thoroughly fractured.

paths are initially through host rock environments then into the pluton, where packet 3 remains for the 2×10^5-year duration of the event while 1 and 2 move out the pluton top and through host rocks again. The Darcy velocities of the fluids along their respective paths range from an average of 10^{-6} cm/sec for packet 2 to $< 10^{-8}$ cm/sec for packet 3.

Representing the path of the fluid packets through temperature-pressure space with respect to the phases in the H_2O system permits quantitative prediction of the solution properties of the circulating fluid packets (Fig. 5). Packet 1 flows downward along a nearly normal temperature-pressure gradient, then its temperature increases at constant pressure as it flows into the pluton. The pluton temperature by this time has decreased to ~ 200°C. This packet then flows out the pluton top and upward into overlying host rocks subparallel to a nearly normal gradient. Packets 2 and 3 have similar paths except that they are initially at higher pressures than they subsequently encounter along their paths. The solution properties of liquid and supercritical fluid along these types of paths vary in a manner that undoubtedly has a profound affect on fluid-rock reactions along the path (Helgeson and Kirkham, 1974a, 1974b).

Sourcelines for fluids which flow through positions 1 and 2 in the pluton indicate that during the initial 5,000- to 15,000-year cooling period fluid sources occurred entirely within the solidified and permeable pluton, but that at times $> 10^4$ years fluids were derived from the surrounding host rocks (Fig. 6A). An implicit assumption in the computation is that the fractures which form in the pluton are

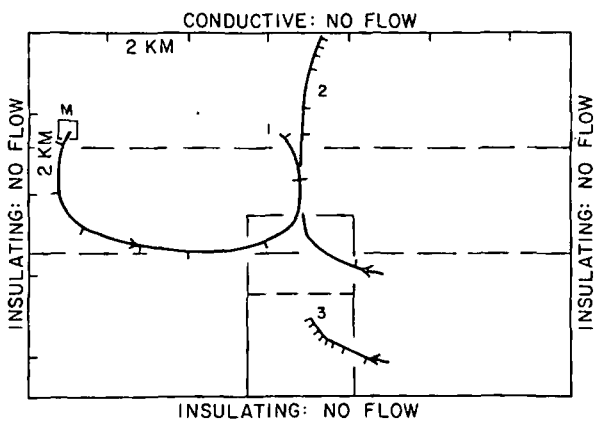

FIG. 4. Fluid pathlines 1–3 after 2×10^5-years elapsed time: 1, for fluids whose initial positions are in relatively permeable host rocks and far away from the pluton; 2, in low permeability host rocks, near the side contact of the pluton and adjacent to the portion of the pluton which has time dependent permeability; and 3, near the base of the system adjacent to the pluton. Tic intervals along the pathlines are at 25,000-year increments, and arrows represent the direction of fluid packet motion.

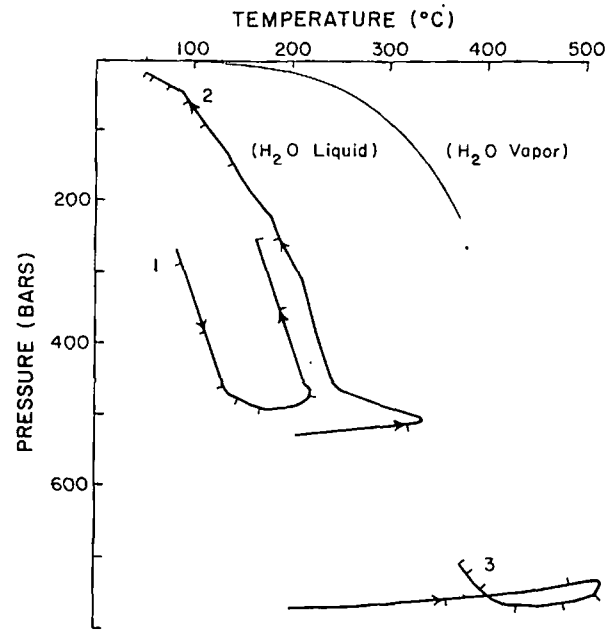

FIG. 5. Fluid pathlines after 2×10^5-years elapsed time, 1–3, from Figure 4 projected onto a temperature-pressure section of the H_2O system, illustrating variations in conditions encountered along flow paths with respect to the liquid-vapor surface. Arrows represent direction of flow and tic marks represent 25,000-year time increments.

filled with fluids derived from the magma crystallization process. These fluids are analogous to magmatic fluids but are approximated by the H_2O system. Relatively large concentrations, > 15 weight percent, of dissolved components in this fluid phase might temporarily alter the flow pattern as a result of the higher density of these fluids with respect to lower concentrations in the surrounding host rock fluids. The important point here is that during the cooling period fluids derived from the host rock environments are the predominant fluids which flow through the pluton. Fluid sources within the host rocks, however, occur as far as 2 km above and 5 km laterally away from the pluton (Fig. 6A, sourceline 1, source point M) but are dominantly from within the 2.7-km-thick permeable layer. The inflections in sourceline 1 between position (1) and the tic mark at 25,000 years reflect both the fracture of the pluton, simulated by a sudden increase in its permeability, and the shift in the fluid density perturbation upward as the rocks and fluids above the pluton become heated.

Sets of sourcelines defined for the pluton describe a sourceregion from which all fluids circulating through the pluton for some time interval were derived. The sourceregion in the host rocks for fluids which flowed through the example pluton extends over a ~ 50 km^2 cross-sectional area (Fig.

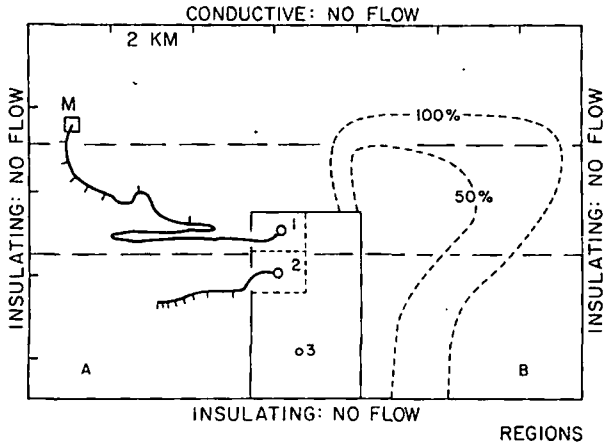

FIG. 6. Sourcelines and sourceregions for fluids which flow through the pluton. A. Sourcelines for positions 1 and 2 for the system in Figure 2, for all fluids which flow through these positions in 2×10^5 years elapsed time. Tic marks on the sourcelines are at 2.5×10^4-year intervals, starting at the end of the line marked with the position number. Position 3 represents a region of effectively zero permeability and therefore cools predominantly by conductive heat transfer for comparison with 1 and 2. The box, M, represents the fluid source farthest from position 1 and coincides with M in Figure 4 on pathline 1. Note the difference between the sourcelines and the actual pathlines that fluids flow along. The regions around the positions (indicated by dashed lines) denote the effective volume (1.25 km² and 1 cm deep) used in computing mass flux in the vicinity of a respective position. B. Sourceregions for all fluids flowing through the pluton. Regions are delimited by contours depicting 100 and 50 percent of those fluids whose source are in the host rocks and were defined by 25 independent sourcelines.

6B). During the initial 5×10^4-year cooling period the fluid mass that circulates through the pluton from host rock sources is derived entirely from between the 50 percent contour and the pluton margins, Figure 6B. The fluid from these sources amounts to approximately 95 percent of the fluid flowing through the upper 2 km of the pluton during the 5×10^4-year time interval; the other 5 percent of the fluid flowing through the upper 2 km of the pluton was derived from sources within the pluton. At an elapsed time of 2×10^5 years, only 2 percent of the fluid was derived from sources within the pluton, and 98 percent was derived from between the 100 percent host rock contour value and the pluton margins. Also, more than 75 percent of the fluid flowing through the upper 2 km of the pluton was derived from the permeable stratigraphic unit in the host rocks.

Sourcelines for fluids which flow through positions in the host rocks are considerably more diversified than for fluids through positions in the pluton. At positions in the relatively permeable host rocks, typified by 4, Figure 7, a considerable amount of fluid recirculation is evident, even to the degree that fluid originating in the vicinity of 4 circulates back through 4 in 4×10^5 years. This recirculation is characteristic of horizontally stratified host rocks within confined permeable units. Positions directly above the pluton, 5, 6, and 8, have sourcelines which indicate a portion of the fluids were derived from sources within the pluton; however, a predominance of these fluids is from sources within host rocks. Because of the thorough redistribution of fluids from host rocks adjacent to the pluton to regions above the pluton, the effect of fluids from magmatic sources is probably obscured.

Sources for hydrothermal fluids in natural systems analogous to the model system analyzed herein are predicted to be predominantly from the host rocks adjacent to and above the pluton. These sourceregions encompass rocks up to 5.5 km away from the side of the pluton. A portion of the fluids is derived from within the pluton, but it only accounts for less than a few weight percent of the total fluid mass that ultimately circulates through the pluton. The compositions of these fluids are a function of conditions at their sources prior to pluton emplacement, as well as temperature-pressure variations and the compositions of fluids and rocks along their pathlines.

The nature of fluid sourcelines in other types of systems, such as those with uniformly permeable host rocks, vertical fracture zones over the pluton, impermeable plutons, and boundary conditions open to flow, have been examined. The sourcelines in these systems are similar to the model systems discussed. However, in systems with impermeable plutons, $k < 10^{-14}$ cm², a minor amount of fluids circulate through the hot plutons. Variations in boundary conditions, permeabilities (for values $> 10^{-14}$ cm²), and pluton geometry result in variations in the shape of the sourcelines and pathlines, but the over-

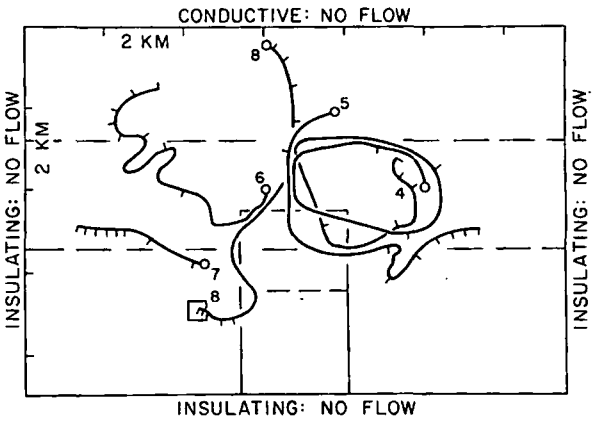

FIG. 7. Sourcelines for fluids which flow through host rocks. The sourcelines for positions 4–8, marked by small circles, indicate a diversity of sourcelines and sourceregions in the domain and a thorough mixing of fluids. Tic marks occur at every 2.5×10^4 years.

all conclusions discussed above are not significantly different for other systems.

The nature of fluid-rock reactions may be predicted if the temperature, pressure, fluid velocity, and amount of fluid flowing through the positions of interest are known. Therefore, these variables were defined for regions in the pluton coincident with sourcelines positions, as represented in Figure 6A. The temperature variation with time at position 3 in the pluton is included since it is analogous to a pluton which cools by simple conduction, whereas the variations at positions 1 and 2 are affected by the large convective heat transport (Fig. 8A). At position 1, Figure 6A, temperatures decrease rapidly to 250°C at $\sim 6 \times 10^3$ years, coincident with a second fracture event. At position 2 temperatures decrease to < 400°C at $> 3 \times 10^4$ years, suggesting that relatively low temperatures are common for the major portion of the cooling time in relatively permeable plutons (Fig. 8A). In general, the increase in pluton permeability to $\geq 10^{-12}$ cm^2 results in the rapid cooling of the upper portion of the pluton to a few tens of degrees above the regional temperature at the corresponding depth. Pressure does not vary significantly during the cooling event and tends to remain at about hydrostatic pressure. However, the fluid velocity increases rapidly in response to the initial conditions and the permeability changes. Darcy velocity maximums of 5×10^{-5} cm/sec and 5×10^{-6} cm/sec are realized at positions 1 and 2, respectively, Figure 8B. A subsequent decrease in velocity follows this initial peak and then a gradual increase to a second maxima. This second maxima in velocities occurs at $\sim 3 \times 10^4$ years, as a consequence of fluid transport properties (Norton and Knight, 1977). As a consequence of these large velocities, 60 percent of the fluid which circulates through these regions does so in $\sim 10^5$ years elapsed time (Fig. 8C).

Conclusions

The redistribution of fluids in hydrothermal systems can be effectively estimated on the basis of numerical solutions to partial differential equations which simulate the cooling of a pluton. The amount and velocity of the fluid flowing through a reference position in the system can also be simulated. The source and flow path of all the fluid which flows through the reference position can be quantitatively determined from the numerical data and the concept of fluid pathlines and sourcelines. These concepts are applicable in any environment where fluids circulate through rocks but appear particularly useful in studies of hydrothermal systems. A detailed approximation of the sourcelines in real systems obviously requires estimations of bulk rock permeability, a geometric description of the geologic units,

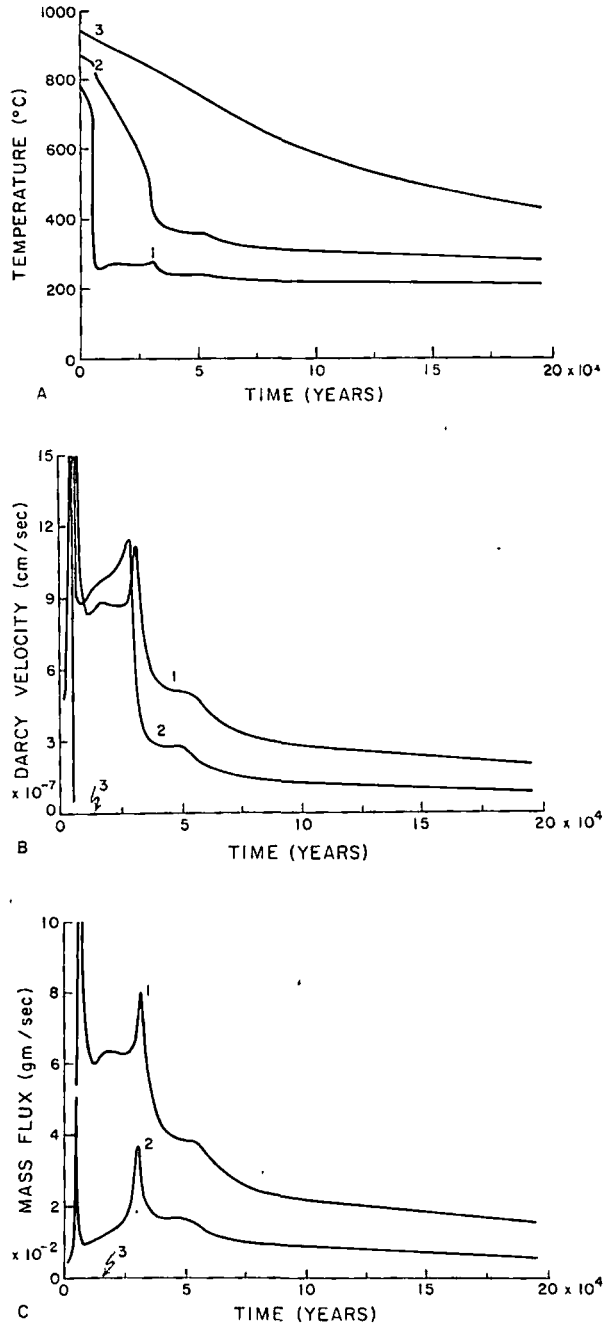

FIG. 8. Transient values for transport variables in the region around sourceline positions 1, 2, and 3 in the pluton, Figure 6A; note tic marks on the ordinate occur at 2.5×10^4-year increments, similar to sourceline tics. A, temperature, B, Darcy velocity, and C, mass flux as a function of time through a 1.25 km^2 area around a respective position. The velocity and mass flux for position 3 plot along the ordinate at the scale of these plots. The maxima on the velocity and mass flux plots near 3×10^3 years result from the emplacement of the pluton. The subsequent decrease is a result of the permeability increase of the pluton. The maxima around 3×10^4 years are the result of the system evolving to temperature-pressure conditions at which the transport properties of the fluid are optimized. Mass flux is computed for 1 cm depth extent into cross section.

and equations of state for saline fluids. There appears to be ample qualitative evidence to suggest that permeabilities in natural systems exceed the 10^{-14} cm^2 minimum in many instances, but by how much is unknown. The scanty data on saline fluids suggest that, as the concentrations of salts approach ~3 molal, significant variations in circulation patterns may be expected, but these effects are highly dependent on the initial distribution of the fluids. The importance of obtaining data on the transport properties of natural systems is clear from the theoretical considerations discussed above.

The example pluton system analyzed suggests that many notions regarding the source of fluid in hydrothermal systems can be quantitatively tested. In particular, the quantity of fluid derived from outside the plutons which cool in permeable host rocks and are themselves permeable appears to be even greater than has been indicated by stable isotope data. Perhaps this is because these data clearly indicate where fluid is not in equilibrium with the rocks it flows through, but once fluid and rock are in isotopic equilibrium the isotopes are no longer a viable tracer.

A definition of the fluid sources and the initial compositions of fluids together with their flow paths are necessary conditions required to simulate the mass transfer of components between fluids and rocks. The previous reaction history of rocks with earlier packets of fluid is then sufficient to define the conditions that prevail during fluid-rock reactions in a hydrothermal system.

Acknowledgments

This research was supported by NSF-GA41136 and its continuation, EAR74-03515 A01. The topic of this manuscript has enjoyed the critique of several colleagues, particularly R. Beane, S. R. Titley, and R. Capuano. I am grateful to J. Knight, R. Knapp, and B. Moskowitz for their thorough discussions and numerous contributions and to L. McLean for her editorial assistance in preparing the manuscript.

Department of Geosciences
University of Arizona
Tucson, Arizona 85721
August 31, 1976; February 23, 1977

REFERENCES

Browne, P. R. L., and Ellis, A. J., 1970, The Okaki-Broadlands hydrothermal area, New Zealand: Mineralogy and related geochemistry: Am. Jour. Sci., v. 268, p. 97–131.

Cooper, John R., 1957, Metamorphism and volume losses in carbonate rocks near Johnson Camp, Cochise County, Arizona: Geol. Soc. America Bull., v. 68, p. 577–610.

Donaldson, I. G., 1962, Temperature gradients in the upper layers of the earth's crust due to convective water flows: Jour. Geophys. Research, v. 67, p. 28–48.

Elder, J. W., 1965, Physical processes in geothermal areas, chap. 8, *in* Lee, W. H. K., ed., Terrestrial heat flows: Geophys. Mon. Ser. No. 8, Baltimore, Am. Geophys. Union, 276 p.

Grindley, G. W., 1965, The geology, structure, and exploitation of the Wairakei geothermal field, Taupo, New Zealand: New Zealand Geol. Survey Bull. 75, p. 131.

Gustafson, L. B., and Hunt, John P., 1975, The porphyry copper deposit at El Salvador, Chile: Econ. Geol., v. 70, p. 857–912.

Helgeson, H. C., 1970, A chemical and thermodynamic model of ore deposition in hydrothermal systems: Mineralog. Soc. America Spec. Paper 3, p. 155–186.

Helgeson, H. C., and Kirkham, D. H., 1974a, Theoretical behavior of aqueous electrolytes at high pressures and temperatures: I. Summary of thermodynamic/electronic properties of the solvent: Am. Jour. Sci., v. 274, p. 1089–1198.

—— 1974b, Theoretical behavior of aqueous electrolytes at high pressures and temperatures: II. Debye-Hückel parameters for activity coefficients and relative partial molal properties: Am. Jour. Sci., v. 274, p. 1199–1261.

Henley, R. W., 1973, Some fluid dynamics and ore genesis: Inst. Mining Metallurgy Trans., v. 2, sec. B, p. B1–B8.

Lapwood, E. R., 1948, Convection of a fluid in a porous medium: Cambridge Philos. Soc. Proc., v. 44, p. 508–521.

Meyer, Charles, 1950, Hydrothermal wall rock alteration at Butte, Montana: Unpub. Ph.D. thesis, Harvard Univ. 329 p.

Nielson, R. L., 1968, Hypogene texture and mineral zoning in a copper-bearing granodiorite porphyry stock, Santa Rita, New Mexico: Econ. Geol., v. 63, p. 37–50.

Norton, D., 1971, Concepts relating anhydrite deposition to solution flow in hydrothermal systems: Internat. Geol. Cong., 24*th* Montreal, sec. 10, p. 237–244.

Norton, D., and Cathles, L., in press, Thermal aspects of ore formation, *in* Barnes, H. L., ed., Geochemistry of hydrothermal ore deposits: New York, John Wiley and Sons Inc.

Norton, D., and Knapp, R., 1977, Transport phenomena in hydrothermal systems: Nature of porosity: Am. Jour. Sci., v. 277, p. 913–936.

Norton, D., and Knight, J., 1977, Transport phenomena in hydrothermal systems: Cooling plutons: Am. Jour. Sci., v. 277, p. 937–981.

Ribando, R. J., Torrance, K. B., and Turcotte, D. L., 1976, Numerical models for hydrothermal circulation in the oceanic crust: Jour. Geophys. Research, v. 81, p. 3007–3012.

Taylor, Hugh P., Jr., 1974, The application of oxygen and hydrogen isotope studies to problems of hydrothermal alteration and ore deposition: Econ. Geol., v. 69, p. 843–883.

Villas, Netuno R., 1975, Fracture analysis, hydrodynamic properties, and mineral abundance in altered igneous rocks at the Mayflower mine, Park City district, Utah: Unpubl. Ph.D. thesis, Univ. Utah.

White, D. E., 1974, Diverse origins of hydrothermal ore fluids: Econ. Geol., v. 69, p. 954–973.

Wooding, R. A., 1957, Steady state free thermal convection of liquid in a saturated permeable medium: Jour. Fluid Mech., v. 2, p. 273–285.

Geothermics (1970) - SPECIAL ISSUE 2

U. N. Symposium on the Development and Utilization of Geothermal Resources, Pisa 1970. Vol. 2, Part 1

Some Theoretical Considerations on Hydrothermal System Due to Cracks

T. NOGUCKI *, K. NISHIKAWA *, T. ITO * AND K. USHIJIMA *

ABSTRACT

It has been disclosed in Otake geothermal field, as the result of the latest deep boring, that there exist Miocene sediments at the depth of more than 1000 meters. This is the most porous stratum we have encountered so far in this field and it is expected to reserve hot water. Many cracks are contained in the volcanic complex covering the Miocene sediments. The upper part of the complex is in an advanced stage of alteration, while the lower part remains unaltered, forming the cap rock to the Miocene sediments.

Since the permeability of the altered volcanic complex is not so large as to make it possible to pass through enough water, the greater part of the well output should be supplied from the cracks connected to the well. The inside fluid pressure of the operating well as well as the cracks connected to it is smaller than the pore water pressure in the stratum of the same level. In order to have water balance maintained, therefore, underground water has to permeate into the cracks from the stratum and be supplied to well through the hot water reservoir.

With the aim of studying the fundamental problems concerning such hydrothermal system, we carried out some calculations by assuming a horizontal hot water reservoir of infinite extent and taking several combinations of cracks and wells into consideration. The velocity distribution, equipotential surface and stream function fo each case were determined and represented graphically. The characteristics of the velocity field were also discussed further.

Hydrogeology of Otake

The stratigraphic units of the Otake region can be grouped into three complexes according to their hydrological significance. From top to bottom they are:

Complex I	permeable	Middle or Upper Pleistocene
Complex II	upper part permeable lower part impermeable	Lower Pleistocene
Complex III	permeable	Miocene

Complex I

The Kuju volcanic complex is mainly composed of hornblende andesite containing augite or hyperstene. In the middle of the activity, it is intercalated with pumice flow of the same rock type. This complex contains many cracks and it is in an advanced stage of alteration. Though the permeability of rock itself is very small, the complex as a stratum may be said to be permeable because of the abundant fissures and fractures that are contained in it. The complex is distributed nearly all over this area and its surface is covered with the Holocene volcanic ash.

Complex II

This complex is named the Hohi volcanic complex and in this area it is developed locally at the surface. It is composed of the alternation of two-pyroxene lavas and their tuff breccias. There is no clear-cut boundary between it and the overlying complex I, since the rocks show gradual change in their texture and mineral compositions. The upper part of this complex is permeable since alteration has advanced as in the case of complex I. But with the increase of depth the alteration becomes weaker and more impermeable, and near the base, the alteration is confined close to fault or fissure, forming a cap rock for the underlying complex III.

Complex III

It has been disclosed by the latest deep boring that there exist Miocene sediments under the complex II. This complex is composed of volcanic pyroclastics, forming the basement of this area. This complex is the most porous stratum we have encountered so far in this field. The extension of the complex is not well known yet because the number of borings is insufficient, nevertheless many geologists believe that this stratum is acting as a hot water reservoir for this field.

The hydrothermal system

While the well's output of this field is of meteoric origin, we cannot deny the existence of a meager amount of magmatic water.

Since the permeability of altered rock itself is small, the greater part of the well output should be supplied from the cracks connected to the well. It was already proved that the fluid pressure inside the operating well, as well as the cracks connected to it, is smaller than the pore water pressure in the stratum (complex I) of the same level. In such a case, it is expected that ground water should permeate into the cracks from stratum. Since the surface area of fault or fissure is considerably large, it can supply sufficient water even if the permeability of the stratum is small.

* Faculty of Engineering, Kyushu University, Fukuoka, Japan.

It is however difficult to expect heat balance only by such a water circulation.

To discuss the water circulation by assuming a horizontal hot water reservoir, we have to consider two types of crack through which water flows in and out. The ground water that permeated from the wall surface of a flowing-in crack comes down as far as the hot

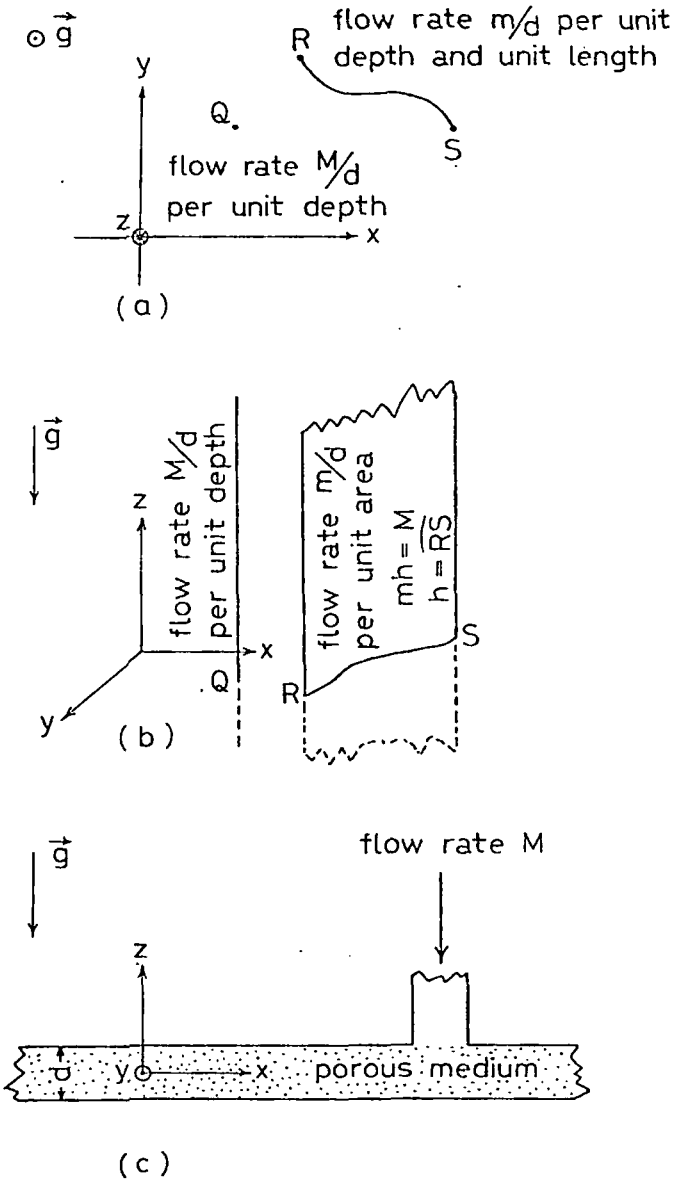

FIG. 1. — *Simplification of problem*

water reservoir and then reaches to a flowing-out crack, passing through the porous medium of the reservoir. The flowing-out crack is connected to the well and serves as a channel of an upward flow of hot water. The calculation of water balance is difficult because of the existence of faults, but the water supply is considered to be sufficient at present because the ground water level of —140 m has remained unchanged after the development.

As to the heat balance, it is not enough to depend only on the conduction of heat energy from the deeper part, as already proved by FUKUDOMI. The authors surmise that the heat should be supplied to the hot water reservoir by the steam which comes up through the weak zone from magma reservoir.

PROPOSITION OF PROBLEMS AND FUNDAMENTAL ASSUMPTIONS

Little is known about the geometry of complex III, the hot water reservoir. Accordingly, rather drastic assumptions have to be made to accomplish any analysis on flow configuration in it. First of all the reservoir was imagined as a horizontal slot of infinite extent. In reality any flow space of infinite area cannot exist, of course. Nevertheless similar assumptions are frequently made for a wide range of physical problems. In doing so we are always anticipating that the solution obtained on the basis of such assumptions might provide us with sound knowledge about physical quantities in the range not far from the origin of the co-ordinate system, if the outer boundary of the real physical space is located sufficiently far from the origin. Another necessary assumption is the uniform thickness of the slot. It was accepted simply because there was no reason to assume any more complicated profile for unknown real slot geometry. In addition to the above-mentioned assumptions all the openings of cracks on the reservoir were treated as a point or a curve. This the present authors considered a reasonable simplification, since details of flow structure near the openings were not needed.

Now we can suppose that there is an isotropic homogeneous porous stratum (hot water reservoir) which is extended infinitely under the ground with thickness d, where the inlet and the outlet of hot water are connected. The hydrological problems in the stratum are to be solved now, since they are considered to be applicable to general cases as the fundamental problems of the hydrothermal system owing to cracks. On the basis of the above consideration, for the convenience of mathematical treatment, we will simplify such a crack opening of finite area as shown in Figure 1c to a line source in Figure 1b. That is, the opening whose amount of flow per unit time is M is replaced by a line source with the amount of outflow M/d per unit depth, which is extended infinitely in $\pm z$ direction. Thus we infer that there exists a point source at point Q on $x-y$ plane, as shown in Figure 1a.

In any case where fault is considered as an opening, it is natural to consider a two-dimentional source extended infinitely in $\pm z$ direction, where the amount of outflow per unit depth and unit length on $x-y$

plane is m/d. In this case, the line source of curve RS is considered to be on $x-y$ plane as shown in Figure 1a.

Description of the flow field and two basic solutions

It is empirically known that Darcy's law is applicable to the macroscopic velocity of the fluid in the isotropic porous medium.

$$\vec{w} = (K/\mu)\nabla\Phi \tag{1}$$

$$\Phi = -P - \rho g z \tag{2}$$

Here $\vec{w}$: velocity vector, K: permeability of porous medium, μ: viscosity of hot water, Φ: potential, P: pressure, ρ: density of fluid, g: magnitude of vector of gravitational acceleration.

Since it is possible to consider hot water as incompressible, we may assume in the present problem the volume of fluid as conserved property. Accordingly, divergence of velocity $\vec{w}$ ought to vanish. If porous medium is homogeneous and the temperature variation of viscosity is ignored, the conservation law will be represented by the following equation (3).

$$\Delta\Phi = 0 \tag{3}$$

Accordingly, the potential satisfies Laplace's equation in a region in which no fluid is generated. Thus the solution of the present problem on steady flow of hot water may be constructed from known results in electrostatics, hydrodynamics, and other subjects. In two-dimentional problems so many solutions are obtained by one for point source. Essentially this results from the fact that Laplace's equation is linear and the superposition principle holds for it. The solution for a point source is called singularity function.

However complicated the configurations of the crack openings are, it is possible to construct potential functions for them, provided the contour integrations of the singularity function can be made.

a) *Point source of intensity N*

The potential, in the case where the source of intensity N exists at $N(\xi_q, \eta_q)$, as Figure 2a, will be

$$\Phi_Q(x, y; \xi_q, \eta_q) = N \ln \sqrt{(x-\xi_q)^2 + (y-\eta_q)^2} \tag{4}$$

This is the singularity function associated to Laplace's equation in plane. All the solutions in the present paper are simply obtained by superposition of this function. Equation (4) satisfies equation (3) at a point other than point Q, while substituting it in equation (1) we can calculate $\vec{w}$. This becomes zero vector when $x^2 + y^2 \to \infty$. This potential therefore satisfies condition at infinity. If we calculate the efflux concerning an arbitrary closed curve surrounding point Q, the result will be $2\pi KN/\mu$. So M and N must be related as follows:

$$2\pi KN/\mu = M/d \quad \text{or} \quad M = 2\pi KNd/\mu \tag{5}$$

Therefore, equation (4) is to give the necessary flow amount at point Q. The stream function in this case may easily evaluated from the equation of Cauchy-Riemann as follows:

$$\Psi_Q(x, y; \xi_q, \eta_q) = N \arctan \frac{x-\xi_q}{y-\eta_q} \tag{6}$$

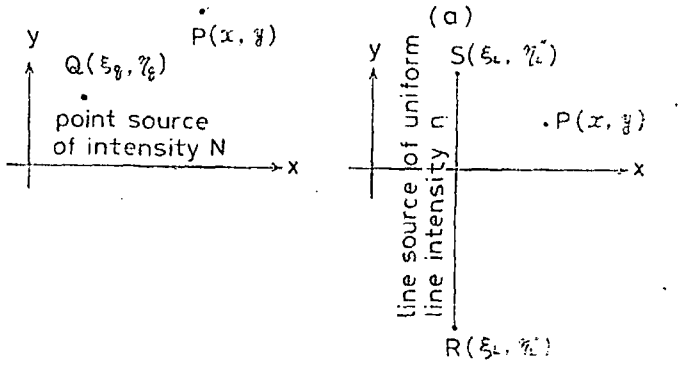

Fig. 2. — *Physical models for two basic solutions*

b) *Line source of uniform line intensity n*

Let us consider a case where there is a line source that has uniform intensity n on line segment RS in Figure 2b. The line segment RS is assumed to be parallel to y axis. The potential in this case can be determined as the superposition of equation (4) from the linearity of equation (3).

$$\Phi_L(x, y; \xi_L, \eta_L', \eta_L'') = n\Big[(y-\eta_L')\ln\sqrt{(x-\xi_L)^2 + (y-\eta_L')^2} - (y-\eta_L'')\ln\sqrt{(x-\xi_L)^2 + (y-\eta_L'')^2} + (\eta_L''-\eta_L') + (x-\xi_L)\Big\{\arctan\frac{y-\eta_L'}{x-\xi_L} - \arctan\frac{x-\eta_L''}{x-\xi_L}\Big\}\Big] \tag{7}$$

The relation between m and n corresponding to equation (5) is as follows,

$$2\pi Kn/\mu = m/d \quad \text{or} \quad m = 2\pi Knd/\mu \tag{8}$$

Stream function will be evaluated as follows:

$$\Psi_L(x, y; \xi_L, \eta_L', \eta_L'') =$$

$$= n\left\{(\alpha-\xi_L)\ln\sqrt{\frac{(x-\xi_L)^2+(y-\eta_L')^2}{(x-\xi_L)^2+(y-\eta_L'')^2}}+\right.$$

$$-(y-\eta_L')\ \arctan\frac{y-\eta_L}{x-\xi_L}+$$

$$\left.+\ (y-\eta_L'')\ \arctan\frac{y-\eta_L'}{x-\xi_L}\right\} \qquad (9)$$

SOLUTION FOR FIVE FLOW SYSTEMS

Five cases as shown in Figure 3 are introduced here as highly simplified models for real flow system, and analyses will be made on them. In case 1, one point source and one point sink are located at interval l. This is an imaginary configuration, of course, but is a limiting situation for case 2 and 4 when the length of each line source and line sink tends to zero, and is useful to discuss the degree of asymmetry of case 2 - 5.

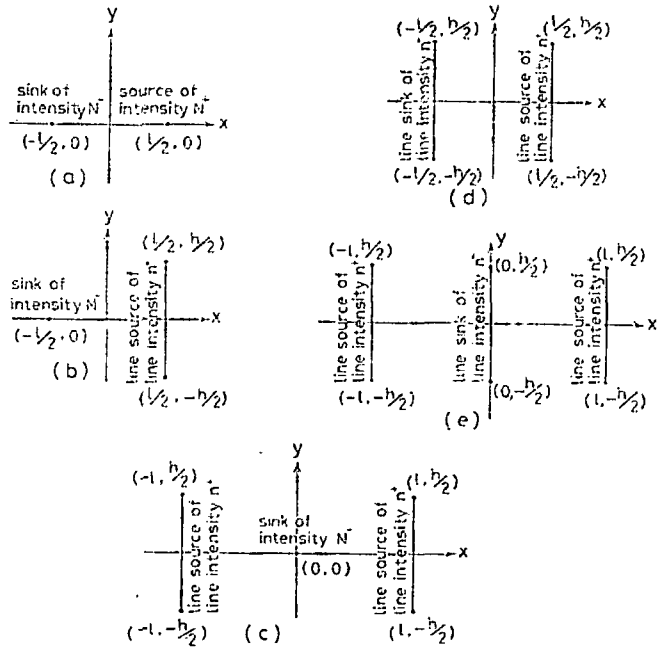

FIG. 3. — *Five flow systems worked out*

(a) case 1, $N^- = -N^+$ (b) case 2, $N^- = -n^+ h$
(c) case 3, $N^- = -2n^+ h$ (d) case 4, $n^- = -n^+$
(e) case 5, $n^- = -2n^+$

In case 3 - 5, line source and line sink run parallel to each other. This certainly has no positive reason. But it has also no positive motivation to deal with lines that do not run parallel. It will be assumed in each case that the relative relation of the magnitude of intensity is determined so that the sum of flowing-in amount and that of flowing-out may be made equal. According to the superposition principle we can express the potential and the stream function for these five cases as follows.

Case 1

$$\Phi_1(x, y) = (N^+/N)\Phi_Q(x, y; l/2, 0) - (N^+/N)\Phi_Q(x, y; -l/2, 0) \qquad (10\text{-}1\text{ a})$$

$$\Psi_1(x, y) = (N^+/N)\Psi_Q(x, y; l/2, 0) - (N^+/N)\Psi_Q(x, y; -l/2, 0) \qquad (10\text{-}1\text{ b})$$

Case 2

$$\Phi_2(x, y) = (n^+/n)\Phi_L(x, y; l/2, -h/2, h/2) - (n^+ h/n)\Phi_Q(x, y; -l/2, 0) \qquad (10\text{-}2\text{ a})$$

$$\Psi_2(x, y) = (n^+/n)\Psi_L(x, y; l/2, -h/2, h/2) - (n^+ h/n)\Psi_Q(x, y; -l/2, 0) \qquad (10\text{-}2\text{ b})$$

Case 3

$$\Phi_3(x, y) = (n^+/n)\Phi_L(x, y; l, -h/2, h/2) + (n^+/n)\Phi_L(x, y; -l, -h/2, h/2) - (2n^+ h/n)\Phi_Q(x, y; 0, 0) \qquad (10\text{-}3\text{ a})$$

$$\Psi_3(x, y) = (n^+/n)\Psi_L(x, y; l, -h/2, h/2) + (n^+/n)\Psi_L(x, y; -l, -h/2, h/2) - (2n^+ h/n)\Psi_Q(x, y; 0, 0) \qquad (10\text{-}3\text{ b})$$

Case 4

$$\Phi_4(x, y) = (n^+/n)\Phi_L(x, y; l/2, -h/2, h/2) - (n^+/n)\Phi_L(x, y; -l/2, -h/2, h/2) \qquad (10\text{-}4\text{ a})$$

$$\Psi_4(x, y) = (n^+/n)\Psi_L(x, y; l/2, -h/2, h/2) - (n^+/n)\Psi_L(x, y; -l/2, -h/2, h/2) \qquad (10\text{-}4\text{ b})$$

Case 5

$$\Phi_5(x, y) = (n^+/n)\Phi_L(x, y; l, -h/2, h/2) + (n^+/n)\Phi_L(x, y; -l, -h/2, h/2) - (2n^+/n)\Phi_L(x, y; 0, -h/2, h/2) \qquad (10\text{-}5\text{ a})$$

$$\Psi_5(x, y) = (n^+/n)\Psi_L(x, y; l, -h/2, h/2) + (n^+/n)\Psi_L(x, y; -l, -h/2, h/2) - (2n^+/n)\Psi_L(x, y; 0, -h/2, h/2) \qquad (10\text{-}5\text{ b})$$

These solutions will be reduced dimensionless respectively as follows.

$$\Phi_I(X, Y) \equiv \Phi_I(x, y)/N^+ \qquad (11\text{-a})$$

$$\Psi_I(X, Y) \equiv \Psi_I(x, y)/N^+ \qquad (11\text{-b})$$

$$\Phi_i(X, Y; \tau) \equiv \Phi_i(x, y)/n^+ h, \quad i = 2, 3, 4, 5 \qquad (11\text{-A})$$

$$\Psi_i(X, Y; \tau) \equiv \Psi_i(x, y)/n^+ h, \quad i = 2, 3, 4, 5 \qquad (11\text{-B})$$

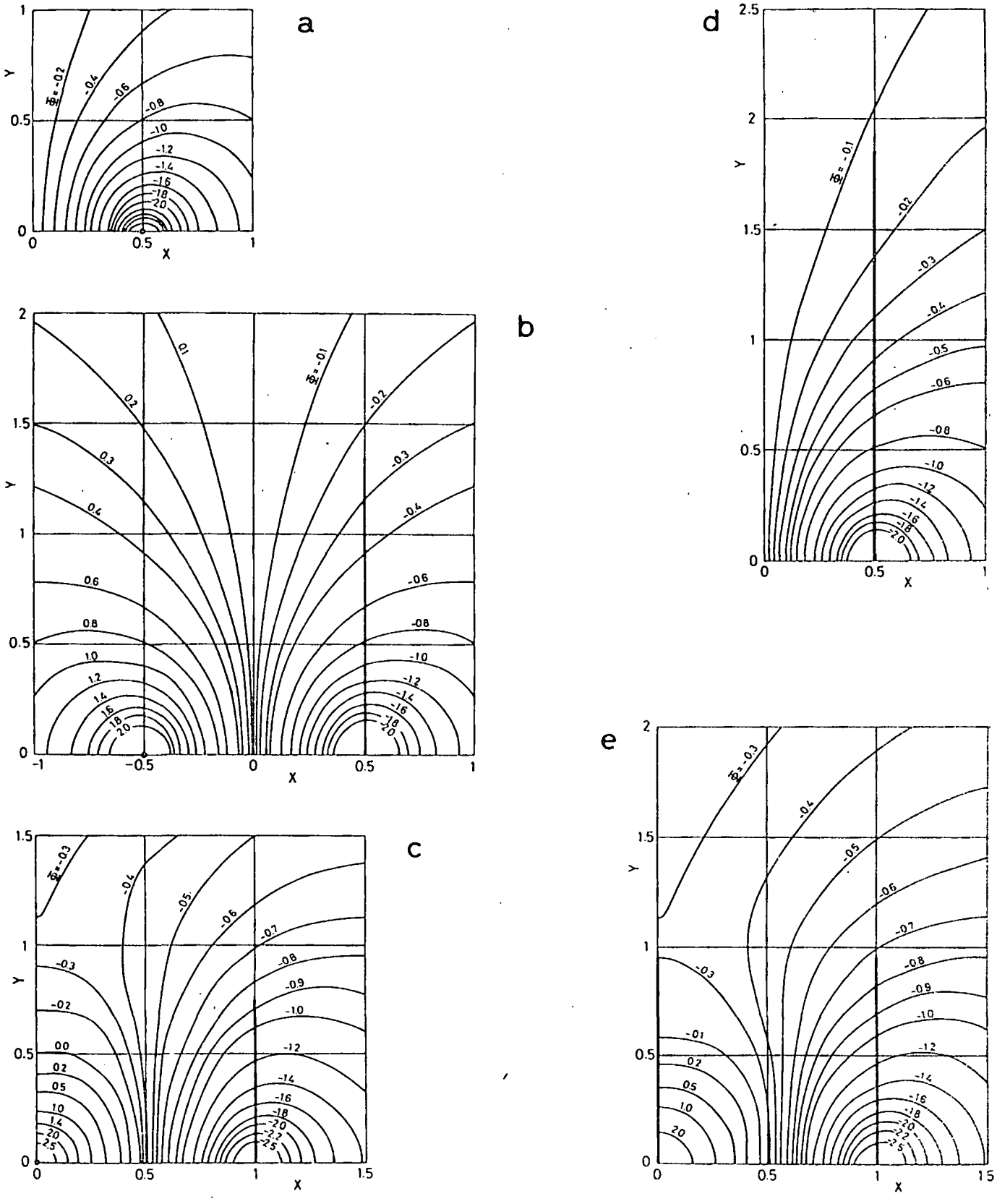

FIG. 4. — *Potentials*

(a) case 1 (b) case 2, $\tau = 2.75$ (c) case 3, $\tau = 1.50$ (d) case 4, $\tau = 3.69$ (e) case 5, $\tau = 1.88$

provided that X, Y and τ are defined in these expressions as follows.

$$X \equiv x/l, \quad Y \equiv y/l, \quad \tau \equiv h/l \tag{12}$$

The distribution of the potential calculated by equation (10) was reduced without dimension as indicated by equations (11) and (12), and was pictured in Figure 4. For cases 2 - 5 the distribution for τ of a specific value is shown, the meaning of which will be explained in the following point.

A CONSIDERATION ON EFFLUX PARTITION

In order to know definitely through which part of the space the largest amount of flow from a certain source passes, or the rate of flow amount which will pass through a certain part of space we will make the following tentative calculation. First of all, the amount of flow that runs along line segment RS of Figure 5 in x direction will be calculated. Namely, defining such $M(x_0, h)$ as follows,

$$M(x_0, h) = -\int_{-h/2}^{h/2} u(x, y)\, dy \tag{13}$$

we will put $x_0 = 0$ in Case 1, $x_0 = l/2$ in Case 2 and Case 4 and $x_0 = l - 0$ in Case 3 and Case 5. The value of equation (13) evaluated thus will be divided by the total amount of flow from the source ($2\pi KN^+/\mu$ in Case 1 and $2\pi Kn^+h/\mu$ in other cases) and then defined it as σ. This flow amount ratio σ is a function only of τ and will be expressed concretely as follows.

Case 1

$$\pi\sigma/2 = \arctan\tau \tag{14-1}$$

Case 2

$$\pi(2\sigma - 1)/2 = \arctan(\tau/2) \tag{14-2}$$

Case 3

$$\pi(2\sigma - 1)/2 = (1/\tau)\ln\{1 + (\tau/2)^2\} + \arctan(\tau/2) \tag{14-3}$$

Case 4

$$\pi(2\sigma - 1)/2 = \arctan\tau - (1/2\tau)\ln(1 + \tau^2) \tag{14-4}$$

Case 5

$$\pi(2\sigma - 1)/2 = (1/\tau)\ln[\{1 + (\tau/2)^2\}/(1 + \tau^2)] - \arctan(\tau/2) + 2\arctan\tau \tag{14-5}$$

The relation between σ and τ to be calculated by equation (14) is shown in Figure 6. For all cases of the Figure we have $\tau \to \infty$ when $\sigma \to 1$. We also have $\sigma = 0.8$ at the black point in the Figure. That is, 80% of the total amount of flow (one half of the total amount of flow in Case 3 and Case 5) passes the part of length h in each case. The value of τ in the case when the above condition is satisfied is shown in Table 1. Cases 2 - 5 of Figure 4 correspond to these values

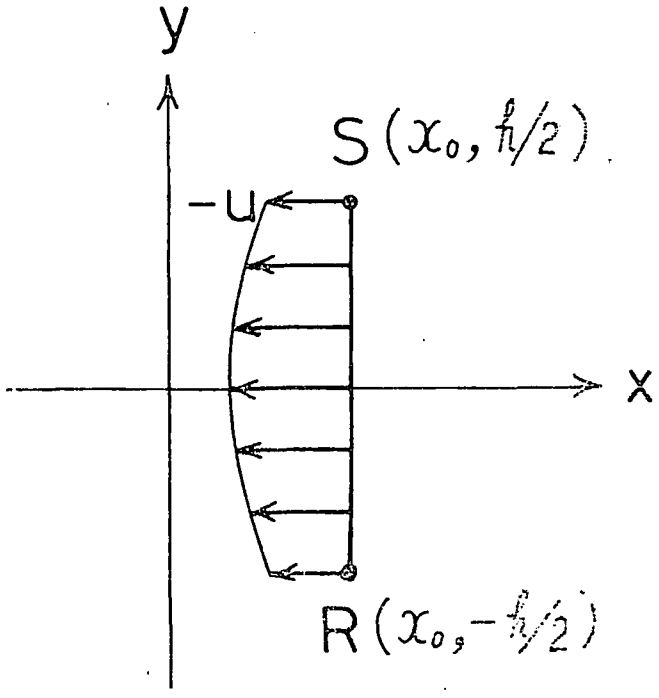

FIG. 5. — *Contour of integration for* (13)

of τ. Case 3 and Case 5 have τ especially small namely this fact implies that, for such an arrangement, the amount of flow is especially concentrated close to the origin. Furthermore, with Cases 2 - 5, we have $\sigma \to 1/2$ for $\tau \to 0$ ($h \to 0$ or $l \to \infty$), which signifies that at least one half of the flow amount flows out of the left side of the line source, even if the interval between the source and sink is infinitely large. Incidentally, in Case 1 when $\sigma \to 1/2$, τ tends to unity, i.e. $l = h$.

TABLE 1.

	τ when $\sigma = 0.8$
case 1	3.08
case 2	2.75
case 3	1.50
case 4	3.69
case 5	1.88

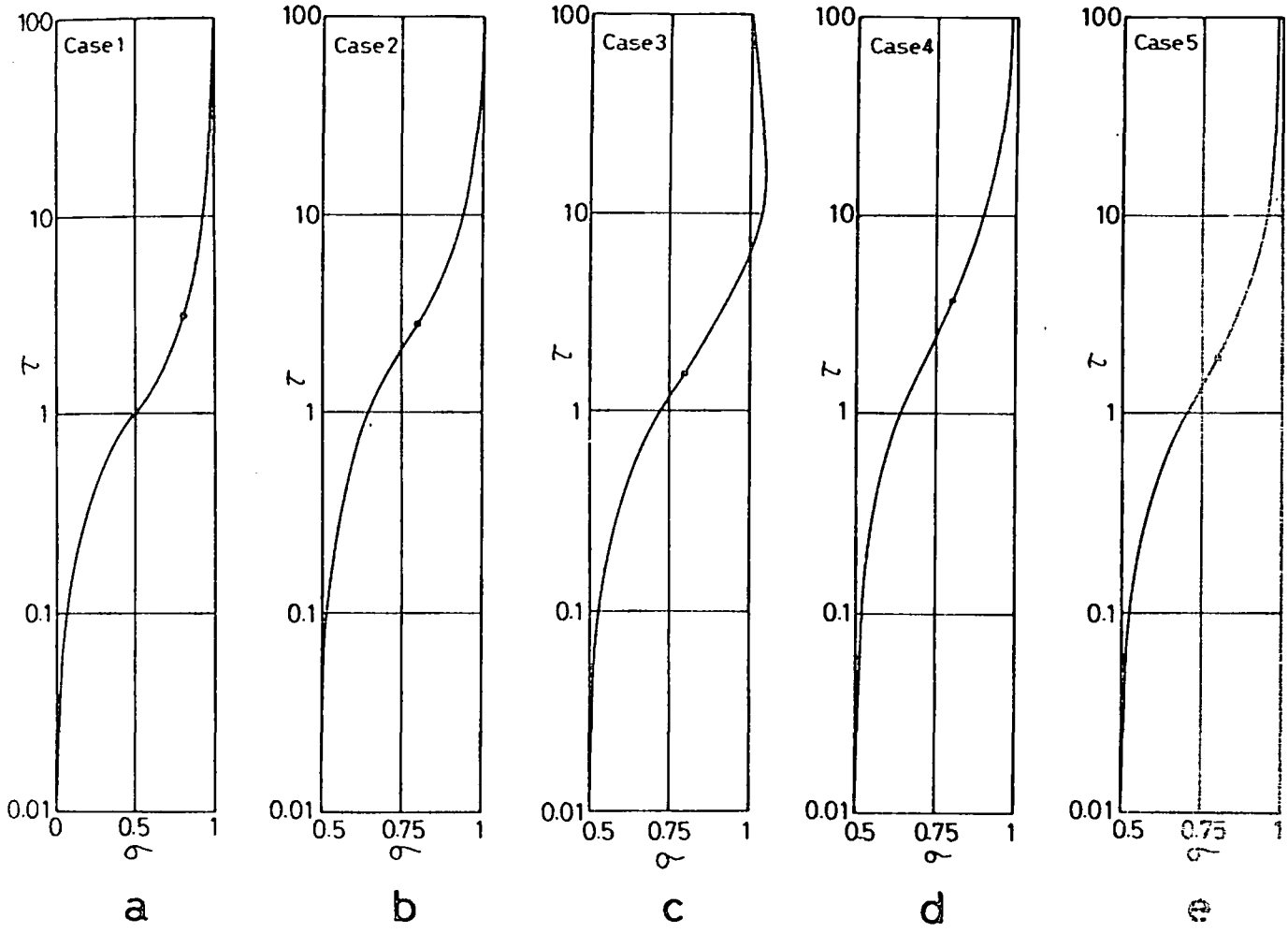

FIG. 6. — *Efflux partition* (a) case 1 (b) case 2 (c) case 3 (d) case 4 (e) case 5

Economic Geology
Vol. 73, 1978, pp. 1556–1566

Hydrothermal Convection and Uranium Deposits in Abnormally Radioactive Plutons *

U. Fehn, L. M. Cathles, and H. D. Holland

Abstract

Hydrothermal uranium deposits are often closely associated with granites of abnormally high uranium content. We have studied the question as to whether the heat generated within such granites can cause fluid convection of sufficient magnitude to develop hydrothermal uranium deposits. Numerical models of flow through porous media were used to calculate temperatures and fluid flow in and around plutons similar to the Conway Granite, New Hampshire, i.e., with a half-width of 17 km, a thickness of 6.25 km, and a uniform internal heat generation rate of 20×10^{-13} cal/cm³-sec. Fluid convection was computed for plutons with permeabilities between 0.01 and 5 millidarcies (1×10^{-15}cm² to 5×10^{-11}cm²).

Flow rates and the size and location of convection cells in and around radioactive plutons like the Conway Granite were found to depend critically on the permeability distribution within the pluton and in adjacent country rocks. The depth of burial, the distribution of heat sources within the pluton, and the small rates of heat generation in the country rock are only of minor importance. Topographic relief is unlikely to affect flow rates significantly but can have a major influence on the distribution of recharge and discharge areas.

Within a few million years, the mass of water transported by steady state convection through such radioactive plutons can equal the mass of water which can convect through them during initial cooling from magmatic temperatures. If the permeability in a Conway-type pluton is on the order of 0.5 millidarcies, then the rate of fluid convection is probably sufficient to develop a hydrothermal ore deposit containing 10,000 tons of uranium in a period of two million years. Such a uranium deposit is most likely to develop in an area of strong upwelling or strong downwelling flow.

Introduction

Hydrothermal uranium deposits are often found in close association with granites containing more than 10 ppm uranium (e.g., Bräuer, 1970; Gangloff, 1970). This close association and the high percentage of leachable uranium in many granites suggest that granitic rocks may well have been the source of uranium in such deposits (Rich et al., 1977). In general, the driving force for the hydrothermal redistribution of metals within granitic plutons is either the initial heat content of the plutons or the later addition of heat from nearby thermal disturbances. Plutons with a high content of radioactive elements are subject to a third driving force: the thermal anomalies within and near such plutons produced by the radioactive decay of potassium, uranium, thorium, and their daughter products. We have investigated the question whether this driving force can generate hydrothermal flow regimes of sufficient magnitude to transport the quantities of uranium found in hydrothermal uranium deposits associated with abnormally radioactive plutons.

We chose as our standard pluton an intrusive of dimensions and composition similar to those of the Conway Granite in New Hampshire. The Conway Granite covers an area of approximately 30×50 km². Birch et al. (1968) found a conductive heat flow between 1.95 and 2.21 HFU (1 HFU = 10^{-6}cal/cm²-sec) associated with radioactive heat generation between 17.5 and 20.9 HGU (1 HGU = 10^{-13}cal/cm³-sec) generated by approximately 15 ppm U, 57 ppm Th, and 4 percent K. Heat flow not produced by radioactivity within the pluton was estimated to be 0.9 HFU. A linear correlation between heat generation in near-surface rocks and heat flow at the surface was observed, and a thickness of 6 km was inferred for the pluton, assuming that the radioelements have a uniform distribution within the pluton.

The Computational Method

The computations of the temperature distribution and convective flow patterns in and near abnormally radioactive plutons were based on the equations for fluid flow through porous media:

$$-\nabla p + \rho g - \frac{\nu}{k} q = 0 \quad \text{(Darcy's law)} \qquad (1)$$

* To Professor Hans Fehn on the occasion of his seventy-fifth birthday.

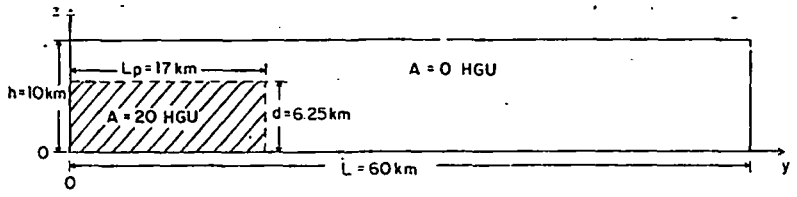

FIG. 1. The computational domain; the point $y = 0$, $z = 0$ is located at the center of the base of the pluton.

$$\nabla \cdot q = 0 \qquad \text{(mass balance)} \quad (2)$$

$$\rho_m c_m \frac{\partial T}{\partial t} = A - \nabla \cdot q c_f T - K_m \nabla^2 T \qquad \text{(heat balance)} \quad (3)$$

where A = radioactive heat generation (cal/cm³-sec), c_f = heat capacity of fluid (cal/g-°C), c_m = heat capacity of fluid-saturated rock (0.2 cal/g-°C), g = gravitational acceleration (980 cm/sec²), H = enthalpy of water (cal/g) ($c_f = H/T$), k = permeability (cm²), K_m = thermal conductivity of fluid-saturated rock (6×10^{-3}cal/cm-°C), p = pressure (dynes/cm²), q = fluid mass flux (g/cm²-sec), ν = kinematic viscosity of water (cm²/sec), ρ = fluid density (g/cm³), and ρ_m = density of fluid-saturated rock (2.7 g/cm³).

Cathles' (1977) program was used to solve this system of equations by means of finite difference methods. Solutions were calculated for two-dimensional models such as that shown in Figure 1. The computational grid contained 20 points in the vertical direction and 30 points in the horizontal direction. Values for the kinematic viscosity, density, and enthalpy of the convecting fluid were assumed to be those of pure water at the appropriate temperatures and pressures of each time step and grid point. The following boundary conditions were used: $q = 0$ (no flow) for $z = 0$, $y = 0$, $y = L$; $q = 0$ (no flow) or $\partial q/\partial z = 0$ (free flow) for $z = h$; $j = K_m \partial T/\partial y = 0$ (insulating) for $y = 0$ and $y = L$; $j = -K_m \partial T/\partial z = 1$ HFU for $z = 0$; and $T = 20$°C for $z = h$. Most of our solutions were obtained for hypothetical plutons of dimensions similar to those of the Conway Granite, i.e., a half-width of 17 km and a thickness of 6.25 km; the burial depth was generally taken to be 3.75 km; zero heat generation in the country rock was assumed, and the heat flow from below the computational domain of 10 km × 60 km was taken to be 1.0 HFU.

In most of our calculations we assumed that the radioelements were uniformly distributed within the pluton and that they generated heat at a rate of 20 HGU. Lachenbruch (1970) and Albarede (1975) have suggested that the linear relationship between radioactive heat generation in near-surface rocks and surface heat flow which has been observed in the region of the Conway Granite and in several other areas (e.g., Lachenbruch, 1968; Jaeger, 1970) is better explained if the concentration of heat sources is assumed to decrease exponentially with depth within the crust. However, differences between the temperature distribution produced by an exponentially decreasing heat source and the temperature distribution produced by a uniform heat source within a Conway-sized pluton were found to be small compared to the magnitude of the temperature anomalies themselves and to produce only second order effects on the patterns and intensity of convective flow. Our results can thus be applied to cases where a linear relationship between heat generation in near-surface rocks and surface heat flow is observed.

Temperatures in and around Impermeable Plutons

The distribution of heat flow and the location of isotherms in and near an impermeable, Conway-type pluton at steady state are shown in Figure 2. At the center of the base of the intrusion, the steady state temperature is 326°C. This temperature is about 140°C higher than the temperature at the same depth beyond the influence of the pluton. The surface heat flow is 2.2 HFU above the center and 1.7 HFU above the edge of the pluton. Temperature and heat-flow anomalies disappear approximately 35 km from the center of the pluton.

The gradual decrease of the heat flow above this pluton outward from its center indicates that heat losses through the sides of the pluton are significant. In a one-dimensional model, i.e., if heat flow through the sides of the pluton is neglected, the surface heat flow j at steady state is the sum of the heat generation in the pluton, Ad (d = thickness of pluton), and the heat flow from below, j_0:

$$j = \mathrm{Ad} + j_0 \quad (4)$$

We have calculated the heat flow above two-dimensional plutons of various sizes and heat generation rates and have compared our results with the results obtained with (4). The steady state heat flow above the center of a pluton was found to be given by the expression

$$j = b_p \mathrm{Ad} + j_0 \quad (5)$$

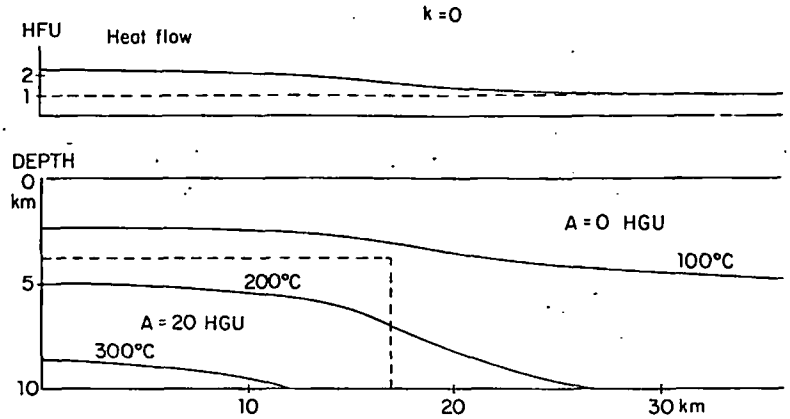

FIG. 2. Steady state distribution of temperatures and surface heat flow in a Conway-type pluton without convection; the broken line indicates the limits of the pluton.

where the coefficient b_c is smaller than unity. The value of b_c depends largely on the ratio of the half-width, L_p, to the thickness, d, of a pluton and is independent of A and nearly independent of the depth of burial. In Figure 3, calculated values of b_c are plotted as a function of the aspect ratio, L_p/d. The heat flow above the center of a Conway-type pluton ($L_p/d = 2.7$) is reduced by only 3 percent by the flow of heat through the sides of the pluton. The values of b_c for plutons with aspect ratios smaller than 1 are less than 0.5; more than half of the heat generated within such plutons is therefore lost through their sides. Consequently, temperatures within, as well as conductive heat flow above, plutons with low aspect ratios or above vertical uranium veins are significantly lower than would be expected on the basis of one-dimensional calculation.

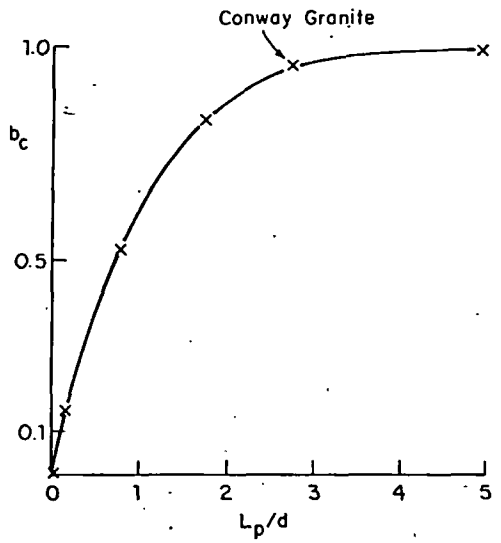

FIG. 3. Values of the coefficient b_c in equation (5) as a function of the aspect ratio L_p/d of the plutons.

Temperatures and Convective Flow in and around Permeable Plutons

Unfractured granites have very low permeabilities, on the order of 10^{-3} millidarcies (1 md $= 10^{-11}$cm^2) (Davis, 1969) at surface conditions. Measurements on Westerly Granite (Brace et al., 1968) show that the permeability decreases by two orders of magnitude over the depth range we are considering here. These bulk permeabilities are too low to allow any significant convection through the granite. In order to generate hydrothermal convection the presence of fractures in the granite has to be postulated. Fractured granites can have permeabilities several orders of magnitude greater than unfractured granites even under increased pressure (Pratt et al., 1977). In our calculations of convective flow through Conway-type plutons, we have used permeabilities between 0.01 md and 5 md.

The distribution of temperature in such plutons depends on the temperature distribution at the time of fracturing, on the permeability, and on the openness of flow through the surface. The curves in Figure 4 illustrate the effects of these variables on the time variation of the temperature at the center of the base of a Conway-type pluton after the onset of convective flow. The temperature-time curves (a) through (e) were computed for the initial temperature distribution (conductive steady state) shown in Figure 2. Curve (f) was computed for a domain with an initial temperature distribution corresponding to a heat flow of 1 HFU from below and no heat generation in the domain before the onset of convection. The broken curves (a) and (c) show the variation of the temperature at the base of intrusions of permeability 0.1 md and 0.5 md, respectively, if no flow takes place through the surface. If the formation lies slightly below sea level or if a strong interaction between surface water and ground water oc-

curs, as in some geothermal fields (e.g., Elder, 1965), boundary conditions permitting free flow through the surface are more realistic. The solid curves (b), (c), and (e) show how the temperature at the center of the base of the intrusion varies with time if free flow takes place through the surface.

Steady state is reached more rapidly in plutons of high than in plutons of low permeability, but in all cases a new near-steady state temperature is reached 1.5 m.y. after the onset of fluid flow. The temperature at the center of the base of the pluton increases slightly along curve (a) when the permeability of the pluton is only 0.1 md and no flow through the surface is permitted. In cases (b) through (e), the temperature decreases with time, more so at higher permeabilities and if free flow takes place through the surface. Along curve (f) the temperature first increases, then declines, and finally becomes indistinguishable from the temperature along curve (d) after about 0.8 m.y.

Steady state isotherms, streamlines, and heat-flow distributions are shown in Figures 5a through e for five different permeability distributions. All these cases were calculated to a time of 1.7 m.y. after the onset of convection. If the permeability is uniformly 0.5 md, and if no flow takes place through the surface (Fig. 5a), then two convection cells develop within the pluton. The center of the larger cell is close to the center of the pluton, and upwelling flow is most intense at the center of the pluton. A second, smaller cell is located near the edge of the pluton. The surface heat flow distribution is related to the flow pattern. A maximum heat flow of 4.6 HFU is reached over the center of the pluton; a second maximum of 2.1 HFU is located above the edge of the pluton.

If free flow through the surface takes place above a pluton of the same uniform permeability of 0.5 md, the flow pattern is drastically different (Fig. 5b) There is a single, large convection cell covering the entire area of the pluton; the intake area is broad and the discharge area over the center of the pluton is narrow. At a distance of 30 km from the center of the pluton, a weak counter cell develops. Heat flow reaches a maximum of 17 HFU in the discharge area of the main convection cell but is sharply depressed below 1 HFU due to downward convection in the area between 4 and 30 km from the center of the pluton.

It is rather unlikely that the permeability of a Conway-type pluton is independent of depth below the surface, and we have determined the effects of an exponential decrease in the permeability with depth on the pattern of convective flow through plutons. We have set the permeability, k, equal to

$$k = k_0 \exp[-f(h - z)/h] \qquad (6)$$

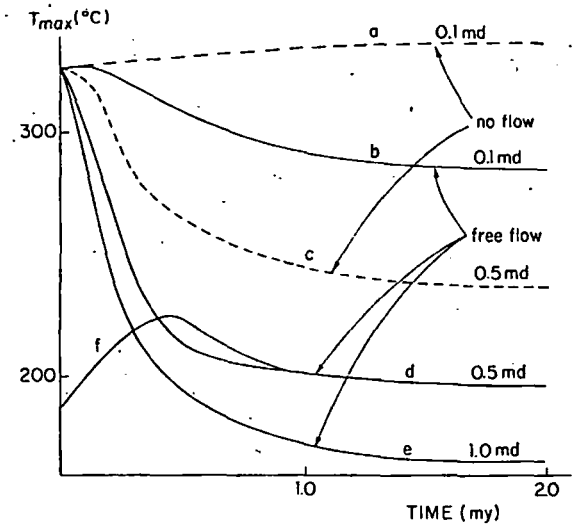

FIG. 4. The temperature at the center of the base of a Conway-type pluton as a function of time after the onset of convective flow; see text for explanation of the individual curves.

where k_0 is the permeability at the surface ($z = h$), and where the permeability k_b at the base of the pluton ($z = 0$) is

$$k_b = k_0 e^{-f}. \qquad (7)$$

If $k_0 = 0.5$ md and $f = 2.3$ in a domain without flow through the surface (Fig. 5c), a single convection cell develops at the center of the pluton with a weak extension to the edge of the pluton. Heat flow is affected above the center of the pluton only, where a maximum of 4.5 HFU is reached. In the rest of the domain, heat flow is similar to that in the absence of fluid flow.

If the surface permeability is taken to be 5.0 md, and if it decreases by two orders of magnitude within the domain ($f = 4.6$), a rather different flow pattern is generated (Fig. 5d). Three quite strong convective cells develop, whose centers are located just above the intrusion at a depth of 3 km. These cells give rise to a second upwelling zone 12 km from the center of the pluton, and there are two maxima in the heat flow distribution with values of 4.5 and 4 HFU, respectively.

The permeability of many plutons is smaller than that of the surrounding country rock. The flow pattern and heat flow distribution in Figure 5e show that large differences between the permeability of the country rock and the pluton affect the pattern of fluid flow considerably. The permeability of the pluton has been taken to be uniformly 0.05 md, the permeability of the country rock ten times greater. Free flow through the surface has been assumed. Two circulation cells develop, a rather shallow one above the pluton and a deeper one just outside the pluton.

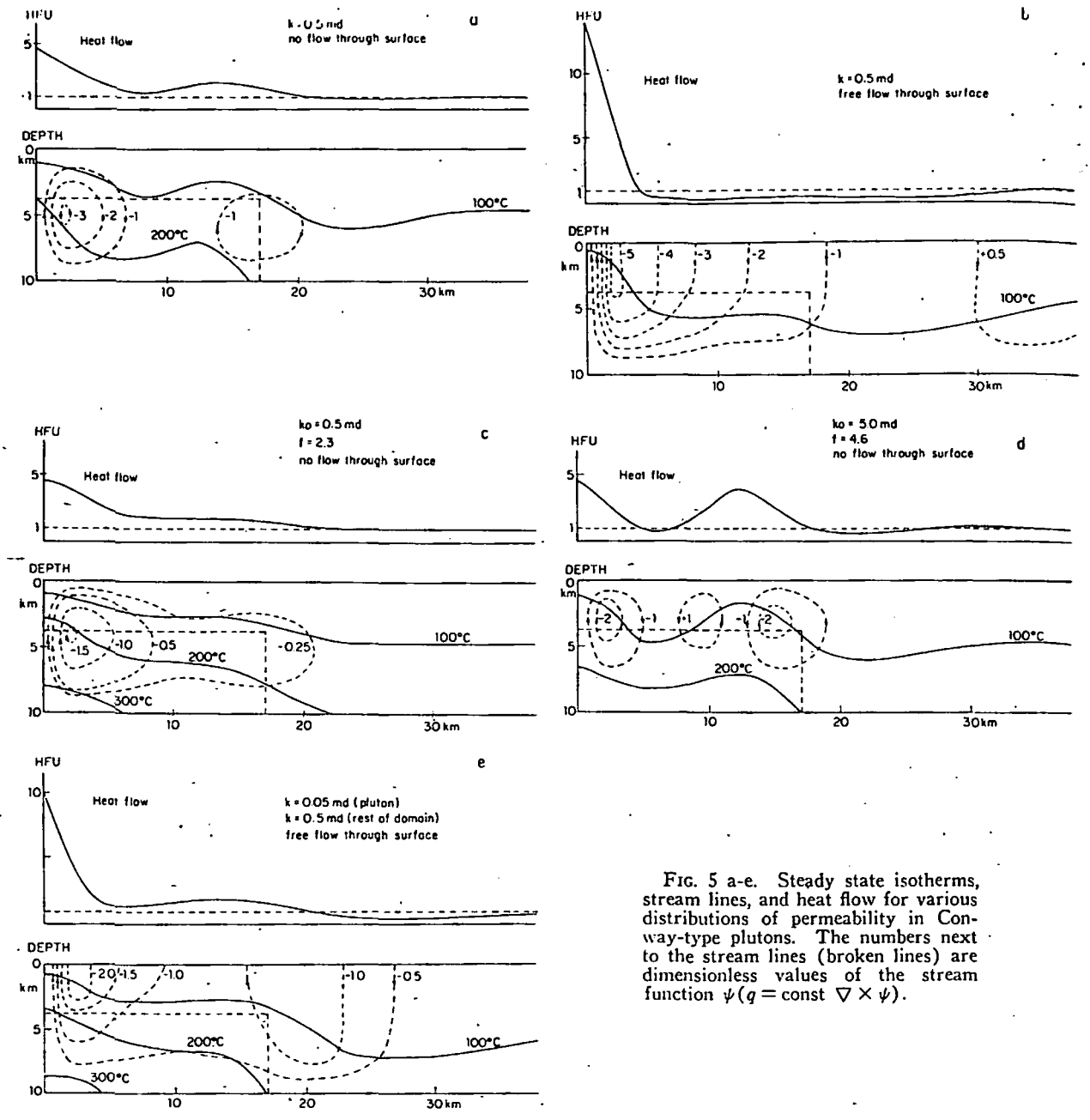

FIG. 5 a-e. Steady state isotherms, stream lines, and heat flow for various distributions of permeability in Conway-type plutons. The numbers next to the stream lines (broken lines) are dimensionless values of the stream function $\psi (q = \text{const}\ \nabla \times \psi)$.

The heat flow maxima are considerably smaller, and the shape and position of the cells are somewhat different from those in Figure 5b, where a uniform permeability of 0.5 md was taken for both the pluton and the country rock.

Convective Mass Fluxes

Figures 5a through e show that the steady state rate of fluid flow through the top of the pluton varies considerably from place to place. In Figure 6 the maximum steady state rate of fluid flow through the top of the pluton is plotted against the permeability of the pluton. When the permeability in the domain is uniform, the maximum flow rate is always found over the center of the pluton. Fluid flow increases rapidly with increasing permeability and is higher in a pluton of a given permeability if free flow is permitted through the surface than if no flow takes place through the surface. In both cases, maximum flow rates are between 1 and 5 gm/cm²-yr in the upper part of the permeability range investigated.

A useful measure of the efficiency of steady state convective flow driven by radioactive heat generation is the time, t_p, required to convect through the sur-

face of the pluton a mass of solution equal to the mass of the pluton itself. Since upward flow prevails only in part of the pluton, t_p is considerably longer than the time computed using the maximum flux rates of Figure 6. In Figure 7, values of t_p are shown for all cases calculated in this study; the closed symbols represent cases where free flow through the surface of the domain was permitted, the open symbols represent cases with a closed surface. Cases calculated for permeabilities exponentially decreasing with depth are plotted at their respective surface permeability.

For permeabilities between 0.5 and 1.0 md, values of t_p fall between 3 and 5 m.y. In plutons of lower permeabilities, the flux time t_p can exceed 100 m.y. Because the major part of the convection in domains of exponentially decreasing permeabilities (triangles in Fig. 7) takes place in the upper part of the domain, *the flux times t_p are usually longer for these cases* than for comparable cases with uniform permeabilities. Higher permeability in the surrounding country rock than in the pluton (closed square in Fig. 7) causes faster convection not only in the country rock but also within the pluton, so that the flux time t_p is shorter by 3.7 m.y. than t_p when the permeability is 0.05 md in the entire domain.

The flux time t_p is not particularly sensitive to the value of heat generation in the country rock. If heat generation in the country rock is raised from 0 to 3 HGU, then t_p is reduced by less than 5 percent. It is also little influenced by the thickness of cover above the pluton. Complete elimination of the 3.75 km cover increases t_p by 2 percent. One case was calculated for a pluton of a uniform permeability of 0.5 md, without flow through the surface, in which the concentration of radioelements decreased exponentially with depth (Lachenbruch, 1970). If such a pluton has the same heat generation in near-surface rocks and the same surface heat flow as a pluton in which the radioelements are uniformly distributed (Birch pluton), then the Lachenbruch pluton has to be thicker than the Birch pluton. Although this increased thickness of the pluton was entered into our calculations, fluid flow was restricted for the sake of consistency to the same 10 km depth as in the comparable Birch pluton. The time t_p obtained for the Lachenbruch pluton was 4.0 m.y., which differed by only 0.2 m.y. from the value of t_p calculated for the comparable Birch pluton.

Discussion

A comparison of the values of t_p calculated for various plutons shows that permeability dominates the development of convection cells in a pluton of a given size and heat generation rate. Depth of burial, heat generation in the surrounding country rock, and the distribution of radioelements in the

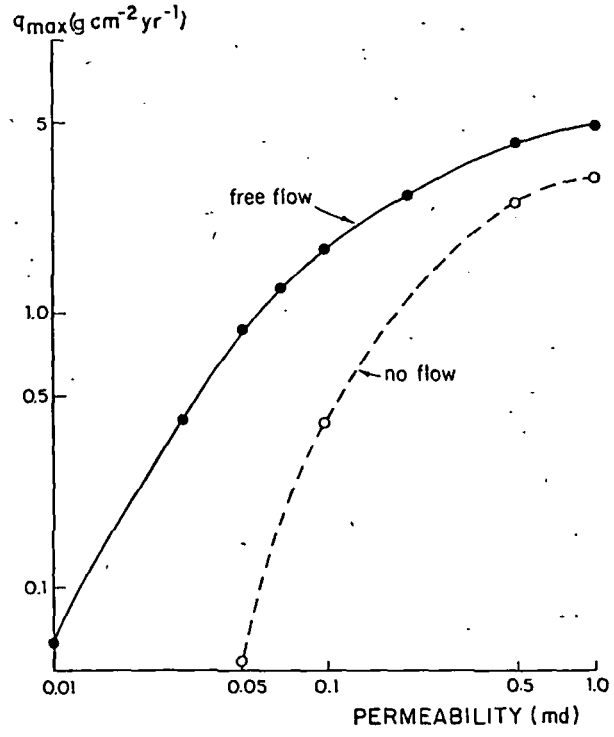

FIG. 6. Maximum steady state flow rates through the tops of Conway-type plutons as a function of uniform permeability in the domain.

pluton exert only a minor influence on the speed and geometry of fluid convection driven by radioactive heat generation. All the flux times were computed using steady state flow rates. During the transient phase after the onset of convection, flow rates are considerably higher than steady state rates; the integrated mass of fluid convected through the pluton during the transient phase can be up to 20 percent larger than the mass calculated using steady state rates. However, since the flux times t_p are at least twice as long as the time required to reach steady state, errors in t_p incurred by neglecting transient flow are probably no greater than 10 percent.

In the calculations described above, temperatures and fluid flow were determined for two-dimensional models where heat losses in the third direction are neglected. Horizontal heat losses through a vertical cylinder are twice as large as horizontal heat losses through a vertical plate (Carslaw and Jaeger, 1959); the temperature and fluid flow distribution in and around plutons of equal x- and y-dimensions are therefore somewhat different from those in and around the plutons discussed above. If heat losses in the x-direction are taken into account in a cylindrical Conway-sized pluton, heat flow above the center of the pluton is reduced by an additional 3 percent of the heat flow produced within the pluton, by 15 percent at a distance of 12 km from the center of the

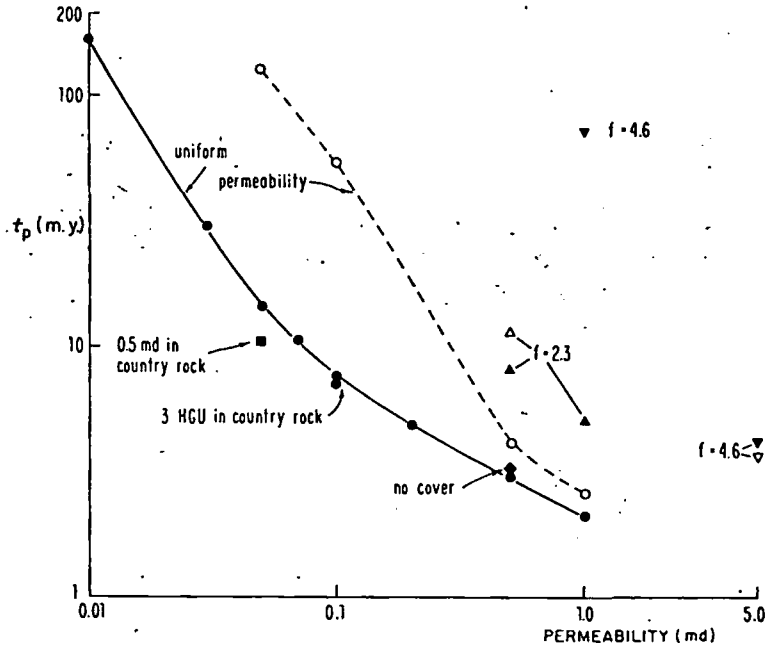

FIG. 7. Flux times t_p for various permeability distributions in Conway-type plutons; t_p is the time required to convect through the surface of the pluton a mass of solution equal to the mass of the pluton itself. Closed symbols = free flow through the surface; open symbols = no flow through the surface; circles = uniform permeability; triangles = permeability exponentially decreasing with depth, plotted at surface permeability.

pluton, and by 35 percent at the edge of the pluton. Since more than 80 percent of the fluid circulation takes place within the inner 11 km of the pluton considered in this paper, heat losses in the x-direction are unlikely to reduce the calculated flow rates by more than 10 percent.

The principal flow direction in our two-dimensional models is toward the center of the pluton. Since the highest temperatures in any pluton with a horizontally uniform distribution of heat sources are necessarily in the center of the pluton, the principal flow direction in plutons with a finite third dimension is also toward the center of the pluton, as long as no cross rolls or other, more complicated, three-dimensional flow patterns develop. Such complications are unlikely at the low Rayleigh numbers (Ra < 60) of our models (Holst and Aziz, 1972; Combarnous and Bories, 1975). The results for two-dimensional flow are therefore probably applicable to plutons with a finite third dimension.

Equations (1) through (3) are specifically applicable to domains in which water convects through a uniformly permeable medium, but they are also applicable to domains in which water moves through a system of fractures, provided the fracture spacing is small enough so that temperatures within matrix blocks between fractures are close to those of a homogeneous porous medium. Relaxation times of matrix blocks with diameters smaller than a few hundred meters are short enough so that this assumption is valid even during the transient phase after the onset of convection.

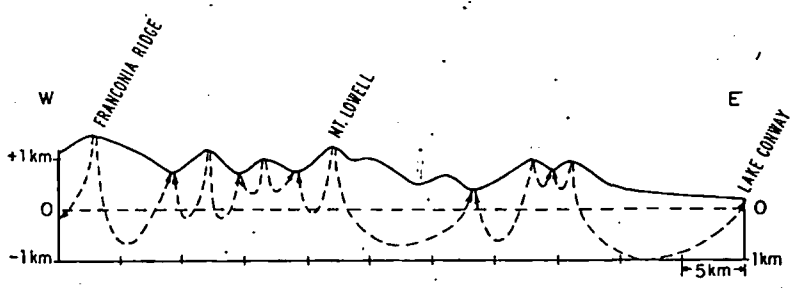

FIG. 8. East-west profile through the Conway area, New Hampshire after Billings (1956); vertical exaggeration 4:1. Broken lines indicate depth below which ground-water flux is smaller than 0.4 g/cm²-yr; $k = 0.5$ md in equation (8); $d = 6$ km in equations (9) and (10), see Appendix.

If distances between fractures are larger than a few hundred meters, the convective system should be modeled in terms of zones of high permeability embedded in a matrix of low or intermediate permeability. Examples of convective flow through domains of this kind have been calculated in a similar investigation of hydrothermal convection at mid-ocean ridges (Fehn and Cathles, in press). There it was shown that a fracture which attracts the fluid flow of an area 3 km wide carries a mass flux which is not significantly different from the mass flux through a similar domain with the same average, but uniform, permeability. The uniform permeabilities used in the present paper can therefore represent the average of high and low permeability zones; flux times and flow rates are likely to remain reasonably unchanged, even if a major part of the fluid flow occurs in fractures spaced as much as several kilometers apart.

A flat surface and a horizontal water table were assumed in all of the calculations. In areas with nonzero topographic relief, the water table is likely to follow the topography. Ground-water movement normally occurs in response to differences in water table elevation. It can be shown, however, that a topographic relief such as that of the Conway area (Fig. 8) does not cause ground-water movement at depths below 1,500 m of a magnitude comparable to that driven by radioactive heat generation (see appendix). Thus, topographic relief of this magnitude does not change the calculated flux times significantly, but it could well influence the geographic distribution of discharge and recharge areas.

Application to the Development of Uranium Deposits

The purpose of our study was to determine whether convection caused by radioactive heat generation in plutons similar to the Conway Granite is of sufficient magnitude to produce ore deposits of uranium. Typical hydrothermal uranium deposits contain on the order of 10^{10}g (10,000 tons) of uranium (Rich et al., 1977), an amount of uranium which is small compared to the 10^{14}g of uranium present in a Conway-type pluton. The uranium in these deposits is typically concentrated in veins with a surface area of around 1 m × 1 km. If 10^{10}g U are contained in a vein 1 m wide in the y-direction and 1 km long in the x-direction, 10^5 g of uranium have been deposited per cm in the x-direction. For a uniform permeability of 0.5 md (no flow through the surface, see Fig. 5a), a steady state flow of 5×10^5 g/cm-yr was found through the top of the pluton. If we assume a content of 0.1 ppm U in the convecting solution—a concentration which is probably common in hydrothermal solutions associated with highly radioactive granites (Rich et al., 1977)—then 5×10^{-2} g U/cm-yr can be precipitated from the fluid in the convection cell. At this rate of uranium precipitation, 2 m.y. are necessary to deposit 10^5 g U/cm. Radioactive heat generation can thus cause convection of sufficient magnitude to develop typical hydrothermal uranium deposits in a reasonably short period of time.

This statement gains strength when one observes that the integrated mass of water convected by radioactive heat generation becomes comparable within a few million years to the mass of water convected during the cooling of a hot intrusive. The cooling of a pluton from 700° to 100°C sets free an energy of approximately 120 cal/g; the heat released by exothermic chemical reactions between fluids and the cooling pluton can increase this amount to approximately 150 cal/g (Norton and Cathles, in press). During the cooling of a pluton of permeability of 0.25 md, a half-width of 1.8 km, and a thickness of 2.25 km from 700° to 100°C, a mass of water equal to about half the mass of the pluton is circulated through the pluton (Cathles, 1977). A radioactive pluton generating 20 HGU needs 4.5 m.y. to attain the same water-to-rock ratio (see Fig. 7) if its permeability is 0.25 md. This period of time is of the same magnitude as the 6.5 m.y. required for a pluton with a heat generation rate of 20 HGU ($=20 \times 10^{-13}$ cal/cm^3-sec) to generate the 150 cal/g which a cooling pluton releases. The mass of water convected through radioactive granite plutons in a few million years is thus as large as the quantity which is potentially convected during the initial cooling of the plutons.

Support for the hypothesis that uranium deposits are sometimes formed as a result of convection driven by radioactive heat generation is provided by the observed distribution of pitchblende ages in hydrothermal uranium deposits found in the vicinity of abnormally radioactive granites. Pitchblendes are often considerably younger than the associated granites. In Haut Limousin, France, for example, the granites are 320 m.y. old; the uranium mineralization apparently took place about 250 m.y. ago (Duthou and Vialette, 1972). Darnley et al. (1965) report ages of 290, 225, 160, and 50 m.y. for uranium ore in Cornwall that is associated with 290 m.y. old granites (Miller and Mohr, 1964). In the Erzgebirge, granites approximately 320 m.y. old (Haake, 1972) contain uranium ores which were apparently deposited 250, 150, 90, and 60 m.y. ago (Leutwein, 1957; Legierski and Sattran, 1967). Some of the later episodes of uranium mineralization in these areas seem to be related to igneous events; others are apparently unrelated to such events. Hydrothermal convection caused by radioactive heat generation is a mechanism which could have formed the uranium deposits which are unrelated to igneous or other known external

thermal events. The beginning and ending of the necessary convective circulation depends mainly on changes in the permeability distribution in plutons of sufficient size and rate of heat generation. Convection can follow the opening of fractures by tectonic events and can be stopped by the closing of fractures, for example, by quartz precipitation. Unlike the cooling of an intrusive, which can cause hydrothermal convection only during a limited period of time after intrusion, heat generated by radioactive decay within a pluton can drive hydrothermal convection at any time and repeatedly in the same location.

It is of interest to inquire where in such convection cycles uraninite or pitchblende is likely to be deposited. Solubility data for UO_{2+x} are still quite incomplete (see, for instance, Rich et al., 1977, and Nguyen and Poty, 1976), but it is clear that UO_{2+x} precipitation can follow both the reduction of U^{+6} complexes in aqueous solutions and a drop in the temperature of aqueous solution which are saturated with respect to UO_{2+x}. Reduction of U^{+6} and U^{+4} takes place whenever uranium-bearing hydrothermal solutions encounter suitable reducing agents. Oxidized ground waters, which have assimilated U^{+6} either before or after entering a homogeneous granite, tend to become gradually more reducing. Progressive reduction may therefore lead to UO_{2+x} precipitation during the downward movement of the solutions. Reduction may, however, be sufficiently far advanced only after a batch of solution is close to the completion of a flow cycle through a granite; UO_{2+x} precipitation then takes place during the rising and cooling of the solutions. Supersaturation of the solutions with respect to UO_{2+x} due to cooling alone is apt to lead to UO_{2+x} precipitation in the rising part of the cycle.

Unequivocal evidence for the flow direction of solutions during the precipitation of UO_{2+x} in hydrothermal uranium deposits is generally lacking. However, the occurrence of quartz in these deposits may be used as an indicator of the flow direction. In approximately 50 percent of the hydrothermal uranium deposits studied in Rich et al. (1977), quartz is closely associated with pitchblende both in time and space. Quartz deposition normally accompanies falling rather than rising temperatures in hydrothermal systems. It seems likely, therefore, that in these hydrothermal uranium deposits, UO_{2+x} deposition also took place in solutions which were cooling during upward flow. In the other half of the hydrothermal uranium deposits, pitchblende was deposited alone or together with minerals other than quartz. In these deposits, pitchblende may have been deposited per descensum. Since the cycling of solutions through a Conway-type granite could produce uranium deposits in both the downwelling and upwelling portions of a convective system driven by heat generation within the granite, prospecting for uranium deposits should be directed both at areas of potential intense downflow and of intense upflow during periods of hydrothermal convection.

Conclusions

Heat generation in large plutons like the Conway Granite, which contain abnormal amounts of radioactive elecents, can cause rather intense hydrothermal convection. Flow rates and the size and location of circulation cells depend critically on the permeability distribution in the pluton and in its environs. Burial depth, distribution of heat sources within the pluton, and small heat generation rates in the surrounding country rock were found to exert only a second order influence on the development of fluid convection within and around the pluton. Ground-water flow due to topographic relief is unlikely to change significantly the amount of hydrothermal convection but can influence the location of discharge and recharge areas.

Within a few million years, the integrated fluid mass circulated through a Conway-type pluton is of the same magnitude as that which can circulate through such a pluton during cooling shortly after intrusion. If the permeability of a Conway-type pluton and that of the surrounding country rock is on the order of 0.5 millidarcies, fluid flow driven by radioactive heat generation is sufficient to develop a hydrothermal deposit of 10^{10}g (10,000 tons) of uranium in a period of 2 m.y., provided 0.1 μg of uranium is precipitated from each gram of solution in the area of ore deposition. Hydrothermal uranium deposits commonly found associated with radioactive granites could therefore be produced by convection driven by radioactive heat generated in the intrusive itself. The age distribution of such uranium deposits supports this hypothesis.

Pitchblende deposition is apt to take place in response to reduction of U^{+6} to U^{+4} and to cooling of the solutions. Although these conditions could be met anywhere in the cycling of the solutions through a granitic pluton, they are most likely to occur during vertical movement of the solutions. Prospecting for such deposits should therefore be concentrated in areas of intense upward or downward solution flow.

Acknowledgments

This research was funded in large part by the U.S. Energy Research and Development Administration under Contract 76-005-E. The second author (L.M.C.) wishes to thank the Kennecott Copper Corporation for its support of his part of the project.

U. F. AND H. D. H.
DEPARTMENT OF GEOLOGICAL SCIENCES
HARVARD UNIVERSITY
CAMBRIDGE, MASSACHUSETTS 02138
L. M. C.
DEPARTMENT OF GEOSCIENCES
PENNSYLVANIA STATE UNIVERSITY
UNIVERSITY PARK, PENNSYLVANIA 16802
April 6, July 11, 1978

REFERENCES

Albarede, F., 1975, The heat flow/heat generation relationship: an interaction model of fluids with cooling intrusions: Earth Planet. Sci. Letters, v. 27, p. 73–78.
Billings, M. P., 1956, The geology of New Hampshire, Part II: Bedrock geology: Concord, New Hampshire State Plan. Devel. Comm., 203 p.
Birch, F., Roy, R. F., and Decker, E. R., 1968, Heat flow and thermal history in New England and New York, *in* Zen, E., White, W. S., Hadley, J. B., and Thompson, J. B., eds., *Studies of Appalachian geology: Northern and maritime*: New York, Interscience Pub., p. 437–451.
Brace, W. F., Walsh, J. B., and Frangos, W. T., 1968, Permeability of granite under high pressure: Jour. Geophys. Research, v. 73, p. 2225–2236.
Bräuer, H., 1970, Spurenelementgehalte in granitischen Gesteinen des Thüringer Waldes und des Erzgebirges: Freiberg. Forschungshefte, v. C 259, p. 83–139.
Carslaw, H. S., and Jaeger, J. C., 1959, Conduction of heat in solids: Oxford, Clarendon Press, 510 p.
Cathles, L. M., 1977, An analysis of the cooling of intrusives by ground-water convection which includes boiling: ECON. GEOL., v. 72, p. 804–826.
Combarnous, M. A., and Bories, S. A., 1975, Hydrothermal convection in saturated porous media: *in* Chow, Ven Te, ed., Advances in hydroscience: New York, Academic Press, v. 10, p. 231–307.
Darnley, A. G., English, T. H., Sprake, O., Preece, E. R., and Avery, D., 1965, Ages of uraninite and coffinite from southwest England: Mineralog. Mag., v. 34, p. 159–176.
Davis, S. N., 1969, Porosity and permeability of natural materials, *in* DeWiest, R. J. M., ed., Flow through porous media: New York, Academic Press, p. 54-89.
Duthou, J. L., and Vialette, Y., 1972, Age namurien du leucogranite de Saint-Sylvestre-Saint-Goussaud-Haut Limousin (Massif Central français): Acad. sci. [Paris] Comptes rendus, v. 274, p. 650–652.
Elder, J. W., 1965, Physical processes in geothermal areas, *in* Lee, W. H. K., ed., Terrestrial heat flow: Geophys. Mon. Ser. 8, Baltimore, Am. Geophys. Union, p. 211–239.
Fehn, U., and Cathles, L. M., in press, Hydrothermal convection at slow-spreading mid-ocean ridges: Tectonophysics, v. 55.
Gangloff, A., 1970, Notes sommaires sur la géologie des principaux districts uranifères étudiés par la C.E.A., *in* Uranium exploration geology: Vienna, Internat. Atomic Energy Agency, p. 77–105.
Häake, R., 1972, Zur Altersstellung granitoider Gesteine im Erzgebirge: Geologie, v. 21, p. 641–676.
Holst, P. H., and Aziz, K., 1972, Transient three-dimensional natural convection in confined porous media: Internat. Jour. Heat Mass Transfer: v. 15, p. 73–90.
Jaeger, J. C., 1970, Heat flow and radioactivity in Australia: Earth Planet. Sci. Letters, v. 8, p. 285–292.
Lachenbruch, A. H., 1968, Preliminary geothermal model of the Sierra Nevada: Jour. Geophys. Research, v. 73, p. 6977–6989.
——, 1970, Crustal temperature and heat production: Implications of the linear heat-flow relation: Jour. Geophys. Research, v. 75, p. 3291–3300.
Legierski, J., and Sattran, V., 1967, Blei-Isotope in Galeniten des Böhmischen Massivs: Freiberg. Forschungshafte, v. C 209, p. 73–85.
Leutwein, F., 1957, Alter und paragenetische Stellung der Pechblende erzgebirgischer Lagerstätten: Geologie, v. 6, p. 797–805.
Miller, J. A., and Mohr, P. A., 1964, Potassium-argon measurements of the granites and some associated rocks from southwest England: Jour. Geology, v. 4, p. 105–126.
Nguyen Trung, C., and Poty, B., 1976, Solubilité de UO_2 en milieu aqueux à 400 et 500°, et 1 kilobar: Nancy, Rapport Annuel 1976 du Centre de Recherches Pétrographiques et Géochimiques, p. 37–39.
Norton, D. L., and Cathles, L. M., in press, Thermal aspects of ore deposition, *in* Barnes H. L., ed., Geochemistry of hydrothermal ore deposits, 2nd ed.: New York, Wiley-Interscience.
Pratt, H. R., Swolfs, H. S., Brace, W. F., Black, A. D., and Handin, J. W., 1977, Elastic and transport properties of an in situ jointed granite: Internat. Jour. Rock Mechanics Mining Sci., v. 14, p. 35–45.
Rich, R. A., Holland, H. D., and Petersen, U., 1977, Hydrothermal uranium deposits: Amsterdam, Elsevier Sci. Pub. Co. 264 p.
Toth, J., 1963, A theoretical analysis of groundwater flow in small drainage basins: Jour. Geophys. Research, v. 68, p. 4795–4812.
Warrick, A. W., and Lomen, D. O., 1974, Seepage through a hillside; the steady water table: Water Resources Research, v. 10, p. 279–283.

APPENDIX

Effect of Topography on Ground-Water Flux

Ground-water movement normally occurs in response to inclined water tables. The relationship between topographic slope and the slope of the water table is mainly a function of rock permeability and of the recharge rate. If permeabilities are similar to those used in our calculations ($k \sim 0.5$ md), the water table follows the topography very closely as long as rainfall exceeds 10 cm/yr (Warrick and Loman, 1974). The near-surface ground-water flux due to a water table slope, dh/dL, in a formation of permeability k is given by Darcy's law (1) which can be written in the form

$$q_0 = \frac{k\rho g}{\nu} dh/dL. \qquad (8)$$

A water table slope of 0.15, for instance, produces a mass flux of 2.25 g/cm²-yr in a formation of 0.5 md permeability. This flux is similar to the mass flux found in our calculations for rock units of the same permeability. If a layer of high permeability exists at or close to the surface, as is the case in many formations, the flux due to a water table slope is *essentially restricted to this high-permeability layer* (Selim, 1975). In areas of uniform permeability, fluid flow occurs throughout the permeable layer, but fluid velocities decrease strongly with depth. The decrease in the two components of fluid mass flux can be approximated by the following expressions (Toth, 1963):

$$q_z(z) = q_{z0} \sinh(\pi z/L)/\sinh(\pi d/L) \quad (0 < z < d) \qquad (9)$$

$$q_v(z) = q_{v0} \cosh(\pi z/L)/\cosh(\pi d/L) \quad (0 < z < d) \tag{10}$$

where L is the distance between recharge and discharge area and d is the thickness of the permeable layer.

L is not necessarily the distance between topographic highs and adjacent topographic lows. Ground-water flow in regions of irregular topography can be classified according to the distribution of recharge and discharge areas (Toth, 1963). Local zones have recharge areas at topographic highs and discharge areas at adjacent topographic lows; intermediate zones have recharge and discharge areas which are separated by one or more topographic highs and lows but do not occupy the highest and lowest places in a region; finally, regional zones connect the highest and lowest places in a region. The distribution of flow between such zones depends on the regional topography: if the general inclination of a region is large compared to local irregularities in the topography, intermediate and regional zones will account for a substantial portion of the ground-water flow. In regions where the height differences between adjacent topographic highs and lows are of the same magnitude as the regional height difference, intermediate and regional zones are practically absent.

The ground-water flow due to topography in the Conway area can be estimated reasonably well (see Fig. 8). Since the elevation difference between the highest and lowest point of the Conway pluton is of the same magnitude as the local differences in elevation, the effects of intermediate and regional zones are probably negligible for ground-water flow. Slopes in the Conway area are generally smaller than 0.15; steeper slopes exist only over small distances. If we assume that the Conway area is of uniform permeability ($k = 0.5$ md), ground-water movement due to water table slopes in that area is essentially restricted to the upper 500 to 1,500 m. Below 1,500 m, fluid velocities due to water table slopes are small compared to those caused by radioactive heat generation.

[AMERICAN JOURNAL OF SCIENCE, VOL. 277, OCTOBER, 1977, P. 937-981]

TRANSPORT PHENOMENA IN HYDROTHERMAL SYSTEMS: COOLING PLUTONS

D. NORTON and J. KNIGHT

Department of Geosciences, University of Arizona, Tucson, Arizona 85721

ABSTRACT. The nature of heat and mass transport in pluton environments has been described by partial differential equations and simulated by numerical approximations to these equations. A series of heuristic models computed on the basis of these equations describes the general features of fluid circulation in the vicinity of an intrusive igneous body within the upper 10 km of the Earth's crust.

Analysis of these models indicates that fluid circulation is an inevitable consequence of the emplacement of magmas in the crust. The magnitude of this fluid circulation generates convective heat fluxes which predominate over conductive heat fluxes when host rock permeabilities exceed 10^{-14} cm^2. However, cooling rates for the pluton are not significantly shortened unless the pluton permeability is also $> 10^{-14}$ cm^2. The geometries of fluid circulation and isotherms are directly affected by variations in pluton size, width, level of emplacement, and permeability, as well as the distribution of permeable zones in the host rocks. Most striking, however, is the effect of the fluid properties on heat and mass transport. The overall style of fluid circulation is effectively controlled by coincident maxima of the isobaric thermal coefficient of expansion and heat capacity with the viscosity minima in the supercritical region of the H_2O-system.

Waters in natural pluton systems are predicted to move from their points of origin to positions several kilometers away in a few hundred thousand years. This redistribution affects magmatic fluids and fluids in host rocks up to several kilometers away from the pluton. Typically, temperature and pressure changes along the fluid flow paths produce dramatic changes in solvent properties. Hence, the fluid-rock interactions along the pathlines should generate diagnostic mineral assemblages and shifts in isotopic compositions. Average fluid:rock mass ratios of 0.4 are realized over the entire permeable portions of the systems.

This analysis reveals the extent of fluid circulation, and magnitude of convective heat flux over broad crustal regions and along crustal plate boundaries where igneous activity is voluminous may be much greater than heretofore realized.

INTRODUCTION

Heat and mass transport processes associated with the emplacement of magmas into the Earth's crust are continually referred to by geologists in their studies of igneous and volcanic rocks. Inferences as to the temperature and pressure conditions within the crust are made mostly on the basis of conductive heat flow, mineral stability data, and analogies to modern environments. In particular, the crystallization and cooling paths of igneous melt systems are inferred from mineral assemblages and experimentally derived phase diagrams. These methods have led to much understanding of the nature of the crust and subcrustal environment, but they require a considerable extrapolation of information derived from a rather complex process.

Magmatic processes may be described by simple physical laws which relate all relevant variables in a set of coupled partial differential equations. Such a description is appealing, primarily because it provides an analysis that is independent of traditional methods and permits consideration of the process at the crustal scale.

Emplacement of magma bodies into the Earth's crust results in large thermal perturbations which are dispersed by a combination of heat conduction and fluid circulation. Generation of a fluid potential field is

the inevitable consequence of a thermal or solute induced pore fluid density anomaly along a horizontal plane in the crust. Recognition of this fact then raises the question of the extent and nature of fluid flow associated with both thermal and "salinity" anomalies in the crust. The magnitude of fluid flux is directly related to rock permeability and transport properties of the fluid. Geophysical evidence suggests that rocks fail by fracture and have interconnected pore spaces to at least 15 km in the crust, and, therefore, convective heat transport may be considerably more significant on a crustal scale than heretofore realized.

This communication derives the partial differential equations that represent the heat transfer process associated with thermal perturbations in the crust, discusses the physical significance of these equations, presents the numerical approximations to these equations, and analyzes how geologic variations in pluton environments affect the cooling history of the pluton. A series of heuristic cooling models that demonstrate the effect of various initial and boundary values on temperature, pressure, fluid velocities, fluid pathlines, and cooling rates are presented.

Large scale fluid circulation around plutons has been actively discussed by students of mineral deposits since the earliest recognition of vein minerals (Ssu-hsiao, 1250; Van Hise, 1901; and Lindgren, 1907). Stable light isotope distribution in pluton environments suggests that fluid derived locally from the surrounding host rocks and ultimately from the local meteoric waters has circulated through most plutons (Taylor, 1971). On the basis of trace element and mineral occurrences, one predicts that a tremendous mass of fluid is required to achieve the mineralogical and bulk composition changes observed in hydrothermal systems.

Analysis of fluid circulation in the crust by mathematical methods has been a topic of study for many years. Lord Rayleigh's original work (1916) defined the fundamental problem which, together with advances in computing technology, encouraged many subsequent efforts (Wooding, 1957; Holst and Aziz, 1972; Elder, 1967; Donaldson, 1962, 1968; Lister, 1974; Ribando, Torrance, and Turcotte, 1976). The common occurrence of high salinity fluids in shallow crustal environments has also been recognized as a probable cause of fluid circulation (Nield, 1968; Veronis, 1968; Rubin, 1973). These studies have defined many of the basic governing differential equations that describe thermal and solute driven fluid circulation. However, each has dealt with idealized equations of state for the fluid and rock phases and with uniform properties in dimensionless systems. In order to relate the processes to geologic features, real fluid and rock properties have been used in this study.

Notation

a — volumetric heat sources (cal cm^{-3} $°C^{-1}$)
A — area (cm^2)
C_f — isobaric heat capacity of the fluid (cal g^{-1} $°C^{-1}$)

C_m — heat capacity at constant pressure of the media (cal g^{-1} °C^{-1})
C_p — heat capacity at constant pressure (cal g^{-1} °C^{-1})
D_1 — matrix coefficient in Poisson equation
D_2 — matrix coefficient in Poisson equation
D_3 — matrix coefficient in Poisson equation
E — internal energy (cal g^{-1})
g — gravitational force vector (cm sec^{-2})
$\bar{i}$ — unit vector in x-direction
$\bar{j}$ — unit vector in y-direction
K — η divided by k
$\bar{k}$ — unit vector in z-direction
k — permeability (cm^2)
k_m — thermal conductivity (cal (cm sec °C) $^{-1}$)
M — mass (g)
M_f — mass of fluid (g)
M_r — mass of rock (g)
P — pressure (bars)
P_r — reference pressure (bars)
q — thermodynamic heat (cal g^{-1})
q_1 — magnitude of fluid flux in x-direction (g cm^{-2} sec^{-1})
q_2 — magnitude of fluid flux in y-direction (g cm^{-2} sec^{-1})
q_3 — magnitude of fluid flux in z-direction (g cm^{-2} sec^{-1})
Q_{ADV} — nonlinear advection term
$\bar{Q}_{conduction}$ — conductive component of heat flow vector (cal cm^{-2} sec^{-1})
$\bar{Q}_{convection}$ — convective component of heat flow vector (cal cm^{-2} sec^{-1})
$\bar{Q}_n$ — component of heat flow vector normal to the surface (cal cm^{-2} sec^{-1})
Q_P — nonlinear density perturbation term
Q_{total} — total heat flux (cal sec^{-1})
$\bar{r}$ — position vector (cm)
R — arbitrary region
R_a — Rayleigh number
S — surface
t — time (sec)
T — temperature (°C)
T_0 — background temperature (°C)
T_r — reference temperature (°C)
$\bar{u}$ — fluid flux vector (g cm^{-2} sec^{-1})
$\bar{u}_x$ — x-component of fluid flux vector (g cm^{-2} sec^{-1})
$\bar{u}_y$ — y-component of fluid flux vector (g cm^{-2} sec^{-1})
$\bar{u}_z$ — z-component of fluid flux vector (g cm^{-2} sec^{-1})
u — variable at known time step
u^* — variable at half time step
u^{p+1} — variable at new time step
$\bar{v}$ — velocity vector (cm sec^{-1})

v_1 — magnitude of velocity in x-direction (cm sec^{-1})
v_2 — magnitude of velocity in y-direction (cm sec^{-1})
v_3 — magnitude of velocity in z-direction (cm sec^{-1})
$\bar{v}_i$ — velocity vector of interest (cm sec^{-1})
$\bar{v}_t$ — tangential velocity vector (cm sec^{-1})
V — volume (cm^3)
w — thermodynamic work (cal g^{-1})
x — cartesian coordinate
y — cartesian coordinate
z — cartesian coordinate
α — coefficient of isobaric thermal expansion ($°C^{-1}$)
β — coefficient of isothermal compressibility (bar^{-1})
Ψ — streamfunction (g cm^{-1} sec^{-1})
ϕ — flow connected porosity
ν — viscosity (cm^2 sec^{-1})
ρ — density (g cm^{-3})
ρ_m — density of the media (g cm^{-3})
γ_1 — boundary equation constant
γ_2 — boundary equation constant
γ_3 — boundary equation constant
∇x — curl

$$\nabla - \frac{\partial}{\partial x} + \frac{\partial}{\partial y} + \frac{\partial}{\partial z}$$

HEAT AND MASS TRANSPORT

Thermal anomalies in the Earth's crust are dispersed by a combination of conductive and convective heat transfer. Thermal energy transfer away from regions of anomalous temperature at depths below 15 to 20 km is apparently by pure conduction, whereas in shallower crustal environments heat transfer by the circulation of fluids augments and, in certain instances, may predominate over conductive heat transfer. Equations sufficiently general to permit a reasonable analysis of temperature distribution and fluid flow in a variety of pluton environments have been developed for a two-dimensional region of the crust into which a thermal energy source has been instantaneously emplaced. The region is treated as a fluid saturated permeable media, and all properties of the fluid phase are described with respect to the H_2O–system and Newtonian mechanisms. Constraints of energy, mass, and momentum conservation are utilized to represent the heat and mass transfer process.

Energy

Energy content of a one component single phase, constant mass system is defined by the first law of thermodynamics:

$$\int_C (dq - dw) = 0. \tag{1}$$

For a reversible process, the work done by the system defines a path independent function, E, called internal energy.

$$E(T,P) - E(T_oP_o) = \int_{T_oP_o}^{T,P} [C_p - PV\alpha T]\, dT + [V P\beta - T\alpha]\, dP. \quad (2)$$

For single phase fluid system eq (2) can be simplified to

$$E(T,P) - E(T_oP_o) = \int_{T_oP_o}^{T,P} C_p dT, \quad (3)$$

where C_p may be either the heat capacity of the fluid phase, C_f, or the average heat capacity of the fluid saturated media, C_m. This simplification introduces a few percent error in the energy content of the system in the vicinity of the fluid critical endpoint.

Consider a permeable, temperature anomalous region, R, in the crust at some temperature, T. Thermal energy transferred from this region across the enclosing surface, S, and to the surroundings can be described in terms of the heat flow normal to the surface, $\bar{Q}_n$ [cal cm^{-2} sec^{-1}]. The conduction contribution to total heat flux is proportional to the negative thermal gradient:

$$\bar{Q}_{conduction} = -k_m \nabla T. \quad (4)$$

Fluids flowing across the surface will also transport thermal energy in direct proportion to their heat content and mass flux,

$$\bar{Q}_{convection} = \bar{u}\, C_f T. \quad (5)$$

Total heat flow, $\bar{Q}_n$, is the sum of eqs (4) and (5):

$$\bar{Q}_n = -k_m \nabla T + \bar{u}\, C_f T. \quad (6)$$

Total heat flux is then the product of the infinitesimal area and the heat flow vector integrated over the entire surface:

$$\bar{Q}_{total} = \int_S \bar{Q}_n dA. \quad (7)$$

The heat lost from the entire region is obtained by transforming vector eq (7) into volumetric integrals by means of the Gauss divergence theorem:

$$\bar{Q}_{total} = \int_S \bar{Q}_n dA = \int_R \nabla \cdot \bar{Q}_n\, dV. \quad (8)$$

Combining eqs (6) and (8) results in the general expression for heat loss from the entire region:

$$\bar{Q}_{total} = \int_R (-\nabla \cdot (k_m \nabla T) + \bar{u} \nabla \cdot (C_f T) + C_f T \nabla \cdot \bar{u})\, dV. \quad (9)$$

Several different natural heat sources or sinks, for example, radioactive decay, heat of crystallization, hydrolysis reactions, or mixing reactions, may be contained in the region. Our treatment will focus on the thermal energy associated with magma bodies in the upper portion of the Earth's crust. We consider here a fairly specific formulation which includes a term, a, for volumetric heat sources and sinks in the region. Total thermal energy content in the region is then

$$E_R = \int_R (C_m \rho_m T + aT)\, dV. \tag{10}$$

The rate at which this heat is depleted is merely the derivative of eq (10) with respect to time,

$$\frac{\partial E_R}{\partial t} = -\int_R (C_m \rho_m + a) \frac{\partial T}{\partial t} dV, \tag{11}$$

where the heat capacity and density of the media and the volumetric source or sink term are assumed to be constant with time.

The rate at which heat leaves the region, defined by eq (9), must equal the rate at which heat is depleted within the region, eq (11), in order to maintain conservation of energy. Since eqs (9) and (11) hold for any portion of the region, the volumetric integrals are zero everywhere, and they become

$$(C_m \rho_m + a) \frac{\partial T}{\partial t} + \bar{u} \nabla \cdot C_f T + C_f T \nabla \cdot \bar{u} = \nabla \cdot (k_m \nabla T). \tag{12}$$

Eq (12) is the partial differential equation describing thermal energy transport in a one component single fluid phase, constant mass, system undergoing reversible changes.

Conservation of Mass, Divergence of $\bar{u}$

Consider fluid flow through a representative volume in which the velocity vector, $\bar{v}$, is described by

$$\bar{v} = v_1 \bar{i} + v_2 \bar{j} + v_3 \bar{k}. \tag{13}$$

And since $\rho \bar{v} = \bar{u}$, the fluid flux vector is

$$\bar{u} = \rho \bar{v} = q_1 \bar{i} + q_2 \bar{j} + q_3 \bar{k}. \tag{14}$$

For unit volume, ΔV, the fluid flux through face $\Delta x \Delta z$ is

$$q_2 (y)\, \Delta x \Delta z, \tag{15}$$

and the fluid flux leaving the opposite face $(y+\Delta y)$ is

$$q_2 (y+\Delta y)\, \Delta x \Delta z. \tag{16}$$

The difference in fluid flux in the y direction is, therefore, given by the difference between eqs (15) and (16),

$$\Delta q_2 \frac{\Delta V}{\Delta y} = [q_2(y) - q_2(y + \Delta y)]\, \Delta x \Delta z. \tag{17}$$

Similarly, the difference in the mass flux for the other faces can be derived. Therefore, the net mass loss or gain from the entire volume over time Δt is

$$M = \left(\frac{\Delta q_1}{\Delta x} + \frac{\Delta q_2}{\Delta y} + \frac{\Delta q_3}{\Delta z} \right) \Delta V \Delta t. \tag{18}$$

Changes in fluid density or the connected flow porosity (Norton and Knapp, 1977) may produce changes in fluid mass in the volume.

$$M = \frac{\partial \rho \phi}{\partial t} \Delta V \Delta t. \tag{19}$$

Combining eqs (18) and (19) and letting Δx, Δy, Δz, and Δt approach zero give

$$\frac{\partial \rho \phi}{\partial t} = \frac{\partial \bar{u}}{\partial x} + \frac{\partial \bar{u}}{\partial y} + \frac{\partial \bar{u}}{\partial z}, \tag{20}$$

which is the conservation of mass or continuity equation for compressible fluid flow. For steady state flow

$$\nabla \cdot \bar{u} = 0. \tag{21}$$

This conservation of mass equation is used to obtain the conservative form of eq (12).

$$(C_m \rho_m + a) \frac{\partial T}{\partial t} + \bar{u} \nabla \cdot C_f T = \nabla \cdot (k_m \nabla T). \tag{22}$$

Momentum Equations

The necessary condition for no fluid flow, $\bar{u} = 0$, is

$$\rho \bar{u} + \nabla P = 0, \tag{23}$$

which is the familiar equation of hydrostatics. Eq (23) can be written in vector form:

$$\begin{bmatrix} 0 \\ 0 \\ \rho \bar{u} \end{bmatrix} + \begin{bmatrix} \partial P/\partial x \\ \partial P/\partial y \\ \partial P/\partial z \end{bmatrix} = \begin{bmatrix} 0 \\ 0 \\ 0 \end{bmatrix} \tag{24}$$

For no flow conditions, eq (24) requires $\partial P/\partial x = \partial P/\partial y = 0$; that is, pressure can only vary with depth, and fluid density must be constant over any horizontal plane. Ergo, lateral variations in fluid density associated with plutons require fluid flow. The magnitude of this flow is determined by the permeability and fluid viscosity, as indicated by Darcy's Law:

$$\bar{u} = \frac{-k}{\nu} (\rho g + \nabla P). \tag{25}$$

Density perturbations may be due to temperature variation, which is defined by the isobaric constant molality coefficient of thermal expansion,

$$\alpha \equiv \frac{-1}{\rho_o} \left(\frac{\partial \rho}{\partial T} \right)_{P, m_i} \tag{26}$$

or to solute content. Considering for the moment only the thermal effects and that α is not a function of temperature[1], eq (26) is integrated:

$$\rho = \rho_o \left[1 - \alpha \left(T - T_o\right)\right], \tag{27}$$

where T_o is the temperature distribution for no flow conditions. The Darcy equation for fluid flow then becomes

$$\bar{u} = \frac{-k}{\nu} \left[\rho_o \left(1 - \alpha \left(T - T_o\right)g\right) + \nabla P\right]. \tag{28}$$

The gradient in pressure with respect to the z axis is $-\rho_o g$; therefore, eq (28) becomes

$$\bar{u} = \frac{k}{\nu} \left[\alpha T - T_o)g\rho_o + \nabla_{xy} P\right]. \tag{29}$$

Eq (29) describes the mass flow due to a thermal anomaly in the Earth's crust.

Combined Equations

The energy balance, conservation of mass, and momentum equations can be treated in one of several possible ways to obtain a numerical solution. We will utilize the conservative form, where the equations are reduced to two independent scalar quantities, streamfunction and temperature.

The circulation tendency of a fluid around the surface is a vector quantity, defined as the product of the average tangential velocity and the distance around the closed surface,

$$\text{Circulation} = \bar{v}_t ds. \tag{30}$$

From Stokes Theorem we have

$$\int_S (\nabla x\, \bar{v})_n dA = \bar{v}_t ds, \tag{31}$$

where $(\nabla x\, \bar{v})_n$ is the component of $\nabla x\, \bar{v}$ in the direction of a unit vector, $\bar{n}$. Applying the circulation concept to eq (29) gives

$$\nabla x \frac{\nu}{k} \bar{u} = \nabla x \left(\alpha(T - T_o)g\rho_o\right) + \nabla x \left(\nabla_{xy} P\right) \tag{32}$$

and, since $\nabla_{x,y} P$ is a gradient field and the curl of a gradient field is zero, the fluid flow equation reduces to

$$\nabla x \frac{\nu}{k} \bar{u} - \nabla x \left(\alpha(T - T_o)g\rho_o\right) = 0. \tag{33}$$

A packet of fluid circulating through permeable rocks reacts with the enclosing rock mass and changes composition along its flow path. A description of this flow pathline is necessary to study the chemical varia-

[1] α indeed varies considerably with P and T, but this modification will be accounted for later.

tions in time of any given fluid packet. Consider a fluid packet in a permeable media and represent its position at time t_o with position vector r_i, where i denotes the particle of interest. As time varies, movement of the packet and changes in its fluid properties can be followed. The velocity of the packet is simply

$$\bar{v}_i = \frac{dr}{dt}. \tag{34}$$

Transforming to orthogonal coordinates and recalling that the fluid flow $\bar{u}$ is defined by $\bar{u} = \rho\bar{v}$,

$$\frac{\rho dx}{q_x} = \frac{\rho dy}{q_y} = \frac{\rho dz}{q_z} = dt, \tag{35}$$

where eq (35) describes the position after time increment dt.

At every instant in time, dt = 0, fluid flux vectors can be related to the streamfunction, which is tangent to these vectors. The parametric equation for this function in three dimensions is:

$$\frac{dx}{q_x} = \frac{dy}{q_y} = \frac{dz}{q_z}, \tag{36}$$

and in two dimensions eq (36) becomes

$$q_z dy - q_y dz = 0, \tag{37}$$

which is an exact differential equation since $\nabla \cdot q = 0$. Eq (37) defines the streamfunction, which can also be written as an exact differential:

$$d\Psi = \frac{\partial \Psi}{\partial y} dy + \frac{\partial \Psi}{\partial z} dz = q_z dy - q_y dz = 0. \tag{38}$$

This leads to the definition of fluid flux in terms of the streamfunction:

$$q_y = -\frac{\partial \Psi}{\partial z}\ ;\ q_z = \frac{\partial \Psi}{\partial y}. \tag{39}$$

Introducing the streamfunction into eq (33) gives

$$\nabla_y x \frac{\nu}{k} \nabla_y \Psi - \nabla_z x \frac{\nu}{k} \nabla_z \Psi - \nabla_y (g\rho_o \alpha(T - T_o)) = 0. \tag{40}$$

Eq (40) reduces to the familiar Poisson equation: $\nabla^2\Psi = f(y,z,t)$, if ν/k is constant.

Eq (33) can now be rewritten, and the operator (∇x) expanded with respect to the y–z plane and $K = \nu/k$ substituted.

$$q_y \frac{\partial K}{\partial z} + K \frac{\partial q_y}{\partial z} - q_z \frac{\partial K}{\partial y} - K \frac{\partial q_z}{\partial y} - g\rho_o \frac{\partial(\alpha(T - T_o))}{\partial y} = 0. \tag{41}$$

Combining eq (39) with (41) and rearranging terms give the general momentum equation:

$$\nabla^2\Psi + \frac{1}{K}\frac{\partial K}{\partial z}\frac{\partial \Psi}{\partial z} + \frac{1}{K}\frac{\partial K}{\partial y}\frac{\partial \Psi}{\partial y} = \frac{g\rho_o \partial(\alpha(T - T_o))}{K\,\partial y} \tag{42}$$

Eq (42) is equivalent to

$$\frac{1}{K}\nabla \cdot (K\nabla\Psi) = \frac{\rho_o g \partial(\alpha T - T_o)}{K\,\partial y}, \tag{43}$$

which forms the basis of the numerical computation. Extensions to afford for anisotropic and heterogeneous permeability distribution follow directly from eq (40).

In summary, the governing partial differential equations are:

Conservation of Energy:

$$(C_m\rho_m + a)\frac{\partial T}{\partial t} + \bar{u}\nabla \cdot C_f T = \nabla \cdot (k_m \nabla T) \tag{22}$$

Conservation of Mass:

$$\nabla \cdot q = 0 \tag{21}$$

Conservation of Momentum:

$$\nabla^2\Psi + \frac{1}{K}\frac{\partial K}{\partial z}\frac{\partial \Psi}{\partial z} + \frac{1}{K}\frac{\partial K}{\partial y}\frac{\partial \Psi}{\partial y} = \frac{g\rho_o \partial(\alpha(T - T_o))}{K\,\partial y} \tag{42}$$

Dimensionless Forms of Equations

The governing equations contain three dependent quantities — temperature, streamfunction, and fluid flux. The solution can be obtained with eqs (22) and (42) alone, since eq (42) is written in conservative form, that is, eq (42) implicitly includes eq (21). In turn, fluid flux can be computed from the stream function, eq (39).

Modeling of geologic processes with the governing equations derived above requires that the variables be scaled, similar to bench scale model experiments. Scaling permits simulation of processes that occur over hundreds of thousands of years in a few minutes of computer time. Often only the dimensionless variables are reported, generally as a constant Rayleigh number; however, to afford for the equations of state of the fluid and rock utilized in this study, Rayleigh numbers were computed from actual temperatures and pressures at each time increment.

The dimensionless forms of eqs (22) and (42) (see table 1 for definitions) are

$$F\frac{\partial T}{\partial t} + \tilde{u}\,\nabla C_t\, T = \nabla \cdot k_m \nabla T \tag{44}$$

$$\frac{1}{K}\nabla \cdot (K\,\nabla\,\Psi) = R_a\,\nabla\,\alpha\,T. \tag{45}$$

TABLE 1

Dimensionless and characteristic values

$y = yl^*$	$k = k\,k^*$
$z = zl^*$	$\nu = \underline{\nu}\,\nu^*$
$\nabla = (\underline{\nabla}/l^*)$	$C_f = C_f\,C_f^*$
$T = TT^*$	$k_m = k_m\,k_m^*$
	$F = 1 + \dfrac{a}{\rho_m c_m}$
	$Ra = \dfrac{g k \rho_o C_f^* T^* \alpha^* l^*}{\nu k_m^*}$
$t = \dfrac{t\, l^{*2} \rho_m C_m}{k_m^*}$	$\alpha = \underline{\alpha}\,\alpha^*$
$\bar{u} = \bar{u}\,\dfrac{k_m^*}{C_f^*\, l^*}$	
$\Psi = \underline{\Psi}\,\dfrac{k_m^*}{C_f^*}$	

Starred quantities are characteristic values for the respective parameters; l^* is characteristic height. For all model systems in this paper, $\Psi = \underline{\Psi}\ 3 \times 10^{-4}$ g cm^{-1} s^{-1}.

Approximations of Equations

The dimensionless energy and momentum equations are of the general form

$$\frac{1}{K}\,(\nabla \cdot (C\,\nabla\,u)) = F\frac{\partial u}{\partial t} - s \tag{46}$$

where s is the nonlinear advection term in the energy equation or the density perturbation term in the momentum equations, and F is a term in the energy equation that accounts for energy sources or sinks in the domain but is equal to 1 in the momentum equation. The equation is readily solved by the alternating direction implicit method (Peaceman-Rachford, 1955).

The alternating direction implicit method has been modified to include the variable parameter C in eq (46). The modified form of the difference equations is, for the initial one-half time step,

$$F_{ij}\frac{u^*_{ij}-u_{ij}}{\Delta t} = \frac{1}{K_{ij}}(\nabla_y \cdot (C_{ij}\nabla_z u^*_{ij}) + \nabla_z \cdot (C_{ij}\nabla_y u_{ij})) - s_{ij}, \tag{47}$$

and for the final one-half time step,

$$F_{ij}\frac{u_{ij}^{p+1}-u^*_{ij}}{\Delta t} = \frac{1}{K_{ij}}(\nabla_y \cdot (C_{ij}\nabla_y \cdot u^*_{ij}) + (\nabla_z \cdot (C_{ij}\nabla_z u_{ij}^{p+1})) - s_{ij}. \tag{48}$$

The expanded finite difference equations are of the general form:

$$D_1\, u^*_{i-1j} + D_2\, u^*_{ij} - D_3\, u^*_{i+1j} = 0. \tag{49}$$

Eq (49) forms a system of linearly independent equations between the N unknown quantities, u*'s, which is quickly solved by a Gauss elimination method.

Nonlinear Terms

Nonlinear terms, S_{ij}, in the momentum and energy equations are the thermal energy advection and fluid density gradients. The advective transport of thermal energy is given by

$$Q_{ADV} = \bar{u}\,\nabla C_p T, \tag{50}$$

The transportive character of this equation must be maintained in the numerical equations. Therefore, "upwind" differencing equations are used:

for $\bar{u} = > 0$

$$Q_{ADV} = \frac{\bar{u}_{ij}}{\Delta z}(C_{ij}\,(T_{ij} - T_{i-1j}) + T_{ij}\,(C_{ij} - C_{i-1j})); \tag{51}$$

for $\bar{u} = < 0$

$$Q_{ADV} = \frac{\bar{u}_{ij}}{\Delta z}(C_{ij}\,(T_{ij} - T_{i+1j}) + T_{ij}\,(C_{ij} - C_{i+1j}))\,. \tag{52}$$

Perturbations caused by fluid density gradients across an arbitrary horizontal plane in the system from eq (42) can be represented by a central difference equation:

$$Q_P = \frac{Ra_{ij}}{2\Delta y^2}(\alpha_{ij}\,(T_{ij-1} - T_{ij+1}) + T_{ij}\,(\alpha_{ij-1} - \alpha_{ij+1}). \tag{53}$$

Boundaries

Difference equations containing a point on the boundary are approximated with a general, first order, constant coefficient boundary condition equation:

$$\gamma_1\, u + \gamma_2\, \nabla\, u = \gamma_3 \tag{54}$$

For i = 2 this equation gives

$$u_{ij} = \gamma_{3_{2j}} + \frac{\gamma_{2_{2j}}}{2\Delta z}\, u^*_{3j}\left(\gamma_{1_{2j}} + \frac{\gamma_{2_{2j}}}{2\Delta z}\right)^{-1} \tag{55}$$

which may be substituted directly into eq (49).

Convergence and Time Steps

The numerical approximation for eq (22) is of the form

$$\nabla \cdot (k_m \nabla T) = F\frac{\partial T}{\partial t} - s. \tag{56}$$

This requires K_{ij} in numerical eq (46) to be equal to 1. A minor modification of eq (46) gives a solution to momentum eq (45) where $K = \nu/k$ and $C = \nu/k$. The transient term does not appear since energy and momentum equations are coupled, and the time step is made through the energy equation. We, therefore, require a steady-state solution which can be achieved through the relaxation sequence, used by Peaceman and Rachford (1955).

The maximum time step that will produce a convergent and stable numerical solution to the equations has been determined by stability analysis. This analysis shows the numerical solutions are stable, if time increments are constrained by

$$\Delta t < \frac{2}{\Delta z} + \frac{2}{\Delta y} + \frac{|q_z|}{\Delta z} + \frac{|q_y|}{\Delta y}. \tag{57}$$

This step size criteria returns a perfectly stable solution and is used in the steady state iteration to define the maximum step size possible for a given problem (Roache, 1972).

The numerical reliability of the model calculations was checked against analytical functions for pure conductive heat transport and were found to be in reasonable agreement. Exact verification is not possible for complex geometries of the heat source or for the combined convective-conductive heat transfer, since exact analytical solutions to these problems are impossible. The models give reasonable cooling times with respect to pure conduction, and the computed fluid fluxes seem realistic. However, the geologic reliability is entirely dependent on the reliability of the initial and boundary conditions and the equations of state for fluid and rock.

Equations of state.—Any equation of state can be used in conjunction with the numerical equations to represent rock and fluid properties. In this study the fluid properties were approximated by the H_2O–system, and the rock properties by average values for the appropriate rock composition.

Fluid.—The fluid phase transport properties significantly affect the nature of the cooling process. The fluid properties, except for viscosity, were computed directly from equations of state for the H_2O system

which was originally developed by Keenan and Keyes (1969), programmed and provided to us by Helgeson (see Helgeson and Kirkham, 1974, for details). The viscosity values were obtained from equations and tables modified from Bruges, Latto, and Ray (1966).

Rock.—The properties of the permeable media were estimated from standard table values for igneous and sedimentary rocks (Clark, 1966). Permeability data were estimated on the basis of analytical equations which relate fracture frequency and aperture to rock permeability (Norton and Knapp, 1977) and observations (Villas, 1975). The greatest uncertainty between the computed models and actual geologic processes is the woefully inadequate data on rock permeabilities. Bulk rock density and heat capacity are considered constant.

Analyses of Pluton Environments

Heat and mass transport phenomena in pluton environments depend on variations in pluton geometry, rock permeabilities, initial pluton temperature and heat content, fluid properties, and the system boundaries. Effects of these geologic parameters on the cooling process have been analyzed, using the partial differential equations and numerical approximations described above. In a sense, a sequence of heat transport experiments which simulate hypothetical systems have been computed in order to ascertain the effects of various geological parameters on transport phenomena in complex and realistic systems.

The emplacement of an igneous mass into the upper 10 km of the crust was assumed to be rapid with respect to the loss of heat by the body. The assumption was also made that fluid properties in these systems may be approximated by the equation of state for the H_2O–system, even though evidence suggests multicomponent fluids are certainly present. Circulating fluids are assumed not to react with the enclosing host rocks even though geologic evidence suggests that reactions occur. Finally, the two-dimensional domain, represented by 200 to 400 discrete points, is assumed to approximate a vertical section through the actual system. The errors introduced by the numerical approximations to the differential equations are on the order of $(\Delta z^2 + \Delta y^2)$ in space and Δt^2 in time. Overall, these errors in the model system are estimated to be less than 10 percent for the first derivatives, with respect to space and time.

The dependent variables, temperature, streamfunction, pressure, fluid, and heat flux, have been computed for a series of optimized steady state iterations which approximate the transient behavior of the system. Fluid redistribution caused by the cooling process and the temperature-pressure path that these fluids are subjected to is also summarized for a series of heuristic models, P1-P8.

Permeability.—Heat is transported in pluton environments by fluid convection and by thermal conduction. In the first portion of this communication, fluid circulation was shown to be an inevitable consequence of emplacement of dikes, stocks, and batholiths into fluid bearing host rocks. Although the magnitude of the thermal flux in such systems is a

linear function of rock permeability for low fluxes, it becomes nonlinear in systems that more closely approximate pluton environments. Therefore, relative contributions of conductive and convective heat transfer to the cooling process were compared.

The magnitude, distribution, and variation of bulk rock permeability with time affect the nature of heat transfer in the model systems. Permeability data on fractured crystalline rocks are not available; therefore, estimates have been based on a simple planar fracture model and on field observations. These considerations, together with interpretations of electrical resistivity and seismic data measured on the upper crust, indicated that bulk rock permeabilities were large enough to permit fluid circulation around hot plutons to depths of 10 to 20 km (Norton and Knapp, 1977). Therefore, we analyzed a sequence of systems whose initial conditions covered a reasonable range in bulk rock permeabilities.

Magnitude.—Systems in which host rocks have permeabilities of 10^{-17} cm^2, nanodarcy, or smaller and are saturated with a fluid whose properties are approximated by the H_2O–system apparently cool by pure conductive heat transfer since the fluid fluxes are $< 10^{-9}$ g cm^{-2} sec^{-1}. Pluton model P1 (fig. 1) is analogous to these types of systems.

Conductive heat transfer from a pluton produces isotherms that tend to be subparallel to the side and top contacts of the pluton and that have a broad convex upward form in rocks above the plutons. As we shall demonstrate in subsequent models, this pattern is unique to a system dominated by pure conductive cooling. The maximum vertical conductive heat flux is realized at the top contact between the pluton and host rocks at time = 0 yrs and decreases exponentially with increasing time (fig. 2).

The temperature maxima migrates upward from the P1 pluton top at 2 cm/yr during the initial 5×10^4 yrs and decreases to 0.5 cm/yr at 2×10^5 yrs (fig. 3). Thus, the initial condition of instantaneous emplacement of the pluton is reasonable for plutons that intrude into the upper crust at a rate $\geq$ 2 cm/yr. As a result of the relatively slow upward migration of thermal energy from the pluton, the 50°C isotherm is not displaced until 5×10^5 yrs after emplacement. Thermal decay of P1 is similar to the thermal decay predicted by Lovering (1935) and Jaeger (1968) using analytic solutions of the heat conduction equation. Their solutions predict the average pluton temperature decreases to 0.3 of the initial anomaly at 5.8×10^6 yrs, whereas our model predicts a decrease to 0.2 of the initial anomaly. The discrepancy is due to heat loss through the pluton top in our model, which was not accounted for in their analytic models, and, undoubtedly, to numerical differences.

The transition from conduction to convection dominated heat transfer occurs in systems where the fluid flux is $\gtrsim 10^{-8}$ g/cm^2 sec, if the heat content of the fluid is $\sim$ 100 cal/g. Host rock permeabilities $> 10^{-14}$ cm^2 and several kilometers tall thermal perturbations produce this magnitude of fluid flux. Models P2 and P3 demonstrate the transition

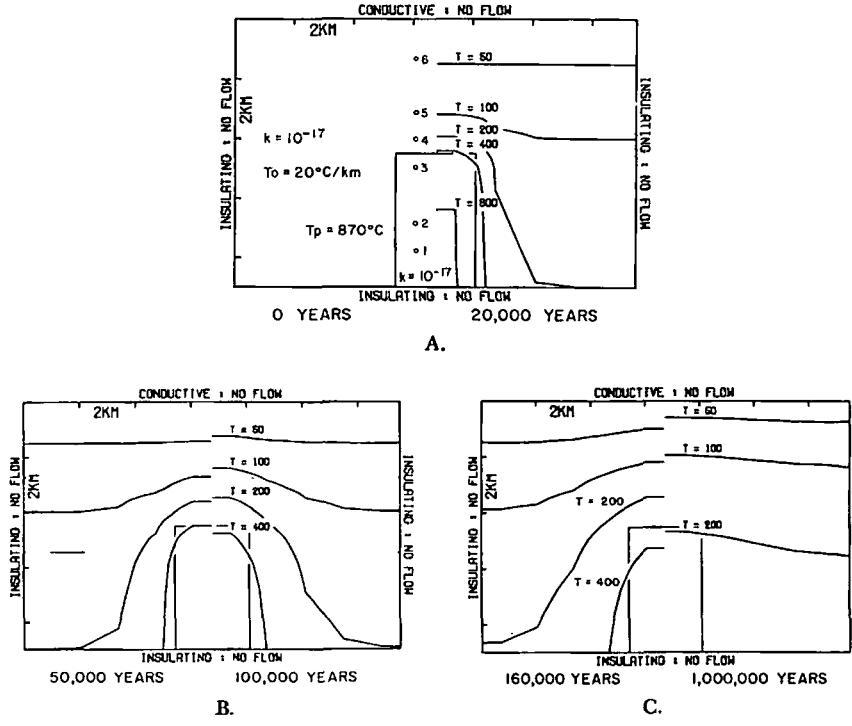

Fig. 1. Two-dimensional cross section of a pluton, Pl, and surrounding host rocks. (A) Boundary conditions and (left) initial conditions are depicted for an impermeable pluton emplaced at 870°C into uniform permeability host rocks, $k = 10^{-17}$ cm^2. Initial temperatures of the host rocks were defined by 20°C temperature at the top boundary and a thermal gradient of 20°C/km. The domain was represented by 100 grid points at regular intervals, $\Delta z = 0.9$ km and $\Delta y = 1.35$ km, and the cooling process was approximated by equations in text at discrete time intervals. (A) Steady state temperature distribution (right half) at elapsed time of 2×10^4 yrs. (B) Steady state temperature distribution in P1 at elapsed times of 5×10^4 yrs (left) and 10^5 yrs (right), (C) Steady temperature distribution in Pl at elapsed times of 1.6×10^5 yrs (left) and 10^6 yrs (right). Note that sharp inflections in all contoured functions are a consequence of the discretization interval and the interpolation function used in the contouring algorithm.

from conductive to convective dominated heat transport for systems containing impermeable plutons and uniformly permeable host rocks.

P2 is characterized by a host rock permeability equal to 10^{-14} cm^2 and has a total heat flux at the pluton top, which is on the average 10 percent greater than in P1, although the differences in isotherm distributions in the two systems are barely discernible. Vertical convective heat flux in P2 increases from zero at t = 0 to 0.5 HFU at 5×10^3 yrs, remains at this value until 10^5 yrs, then decreases gradually to 0.1 HFU at 2×10^5 yrs. Systems with permeabilities $> 10^{-14}$ cm^2 or with taller thermal anomalies than P2 are characterized by larger convective thermal fluxes because of the direct dependence of fluid flux on vertical extent of the initial anomaly and permeability.

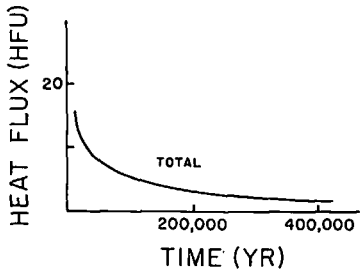

Fig. 2. Conductive heat flux in Pl as a function of time at top of pluton, 1 HFU = 10^{-6} cal cm^{-2} sec^{-1}. Thermal conductivity of 3×10^{-3} cal cm^{-1} sec^{-1} $°C^{-1}$ was assumed for all rocks in the system.

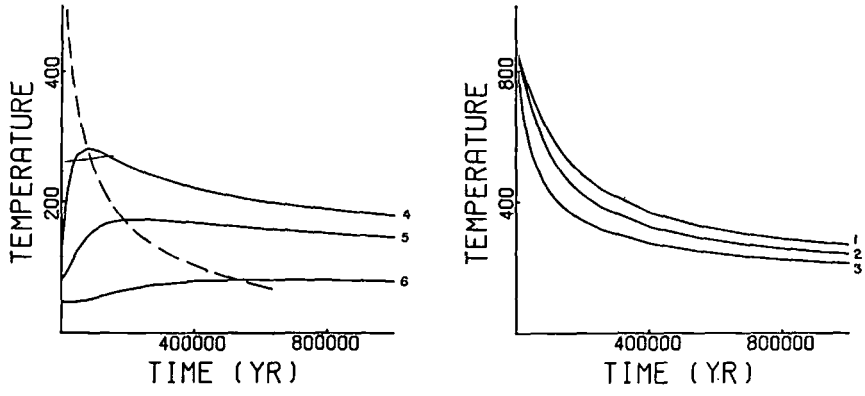

Fig. 3. Temperature as a function of time in Pl at fixed positions (left) 4, 5, and 6, fig. 1A, above top of pluton, 0.45, 1.4, and 3.2 km, respectively, and (right) within pluton at positions 1, 2, and 3, below top of pluton, 2.3, 1.4, and 0.45 km, respectively. Dashed line defines upward migration of temperature maxima with time.

Permeabilities in host rocks and plutons of 10^{-11} and 10^{-14} cm^2, respectively, cause convection to dominate the heat transfer process, P3 (fig. 4).

Fluid circulation in P3 is restricted to host rocks adjacent to and above the side contacts of the pluton (left half of fig. 4, B–D). The relatively lower permeability pluton acts as a barrier to fluid flow (left half of fig. 4B and table 2).[2]

Thermal energy is transferred upward into the overlying host rocks as the fluid circulation cells shift upward (fig. 4B–D). Although the streamfunction reaches a maximum at $\sim 10^5$ yrs, (fig. 4C), the gradient in the streamfunction near the symmetry plane of the system and at the side contacts of the pluton is a maximum at 1.6×10^5 yrs. The maximum fluxes range from 1 to 40×10^{-8} g/cm^2 sec (table 1) and occur directly above the pluton where T≈300°C and P≈250 bars. Although these fluid

[2] As defined in eq (40), the streamfunction is tangent to the instantaneous fluid flux vectors, and the gradient in the streamfunction defines the mass flux normal to that gradient.

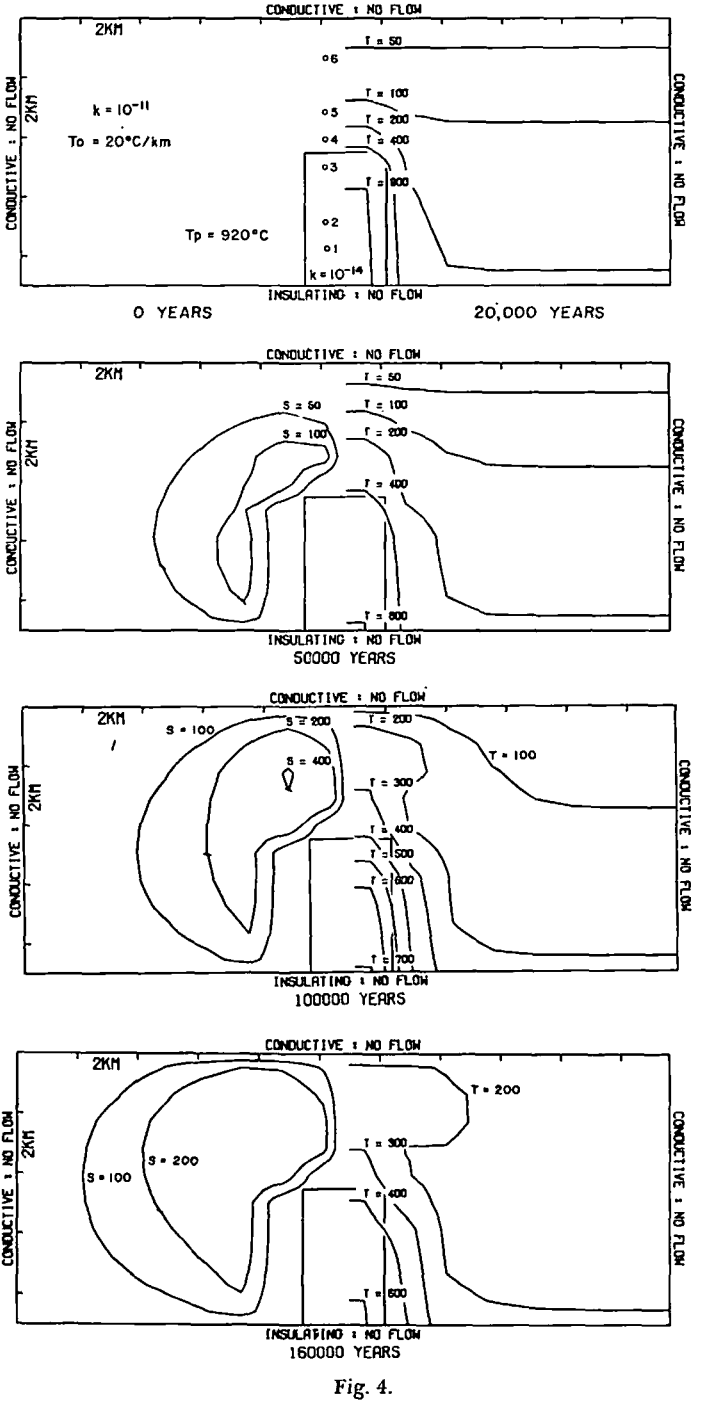
A.
CONDUCTIVE : NO FLOW
2KM
T = 50
T = 100
T = 200
T = 400
T = 800
k = 10⁻¹¹
To = 20°C/km
Tp = 920°C
k = 10⁻¹⁴
CONDUCTIVE : NO FLOW
2KM
CONDUCTIVE : NO FLOW
INSULATING : NO FLOW
0 YEARS
20,000 YEARS
B.
CONDUCTIVE : NO FLOW
2KM
T = 50
T = 100
T = 200
T = 400
T = 800
S = 50
S = 100
CONDUCTIVE : NO FLOW
2KM
CONDUCTIVE : NO FLOW
INSULATING : NO FLOW
50000 YEARS
C.
CONDUCTIVE : NO FLOW
2KM
S = 100
S = 200
S = 400
T = 200
T = 100
T = 300
T = 400
T = 500
T = 600
T = 700
CONDUCTIVE : NO FLOW
2KM
CONDUCTIVE : NO FLOW
INSULATING : NO FLOW
100000 YEARS
D.
CONDUCTIVE : NO FLOW
2KM
T = 200
T = 300
T = 400
T = 600
S = 100
S = 200
CONDUCTIVE : NO FLOW
2KM
CONDUCTIVE : NO FLOW
INSULATING : NO FLOW
160000 YEARS

Fig. 4.

TABLE 2

Fluid fluxes in P3 (g cm^{-2} sec^{-1} × 10^{5})

Position	time yrs =	2×10^4	5×10^4	1.6×10^5
Side contact (lower 3.6 km)				
q_y		0.07	1.	1.
q_z		5	12	25
Above top contact				
q_y		3	21	40
q_z		7	14	31

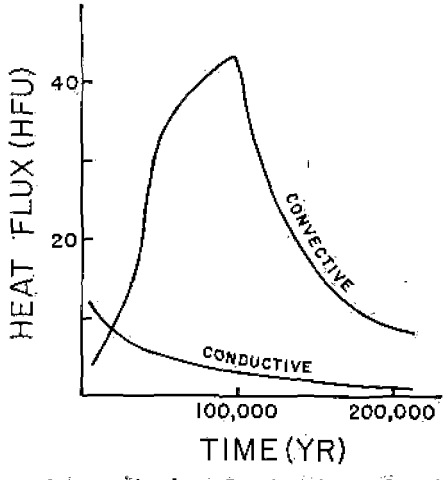

Fig. 5. Conductive and convective heat flux in P3 as a function of time at top of pluton. Thermal conductivity of 8×10^{-3} cal cm^{-1} sec^{-1} °C^{-1} was used for all rocks, whereas heat capacity of fluid was determined from temperature, pressure, and the equation of state for H_2O.

fluxes are relatively small compared with shallow groundwater systems, where fluxes are 10^{-4} cm sec^{-1}, the persistence of the hydrothermal system over 2×10^5 yrs results in the circulation of a large *total* fluid mass.

Heat flux is directly related to the magnitude of fluid circulation. Although within the pluton heat transfer is by conduction, along the pluton margins and in the overlying host rocks convection predominates. Conductive flux at the pluton top is largest at t = 0 yrs and decreases with time (fig. 5). Convective flux increases from zero at t = 0 to a maximum of 45 HFU at slightly less than 10^5 yrs, then decreases to 10 HFU

← Fig. 4. Two-dimensional cross section of system P3 depicting boundary conditions and (*left*): (A) initial conditions for pluton emplaced at an initial temperature of 920°C, into uniform permeability, k = 10^{-11} cm^2, host rocks. Pluton permeability is set at maximum permeability at which conduction dominates heat transfer out of the pluton. Initial temperatures of host rocks were defined by 20°C temperature at the top boundary and a thermal gradient of 20°C/km. The domain was represented by 200 grid points at regular intervals, Δz = 0.9 km and Δy = 1.35 km. (B–D) Steady state dimensionless streamfunction representing counter-clockwise fluid circulation at (B) 5×10^4 yrs, (C) 10^5 yrs, (D) 1.6×10^5 yrs; (*right*) temperature distribution at (A) 2×10^4 yrs, (B) 5×10^4 yrs, (C) 10^5 yrs, (D) 1.6×10^5 yrs.

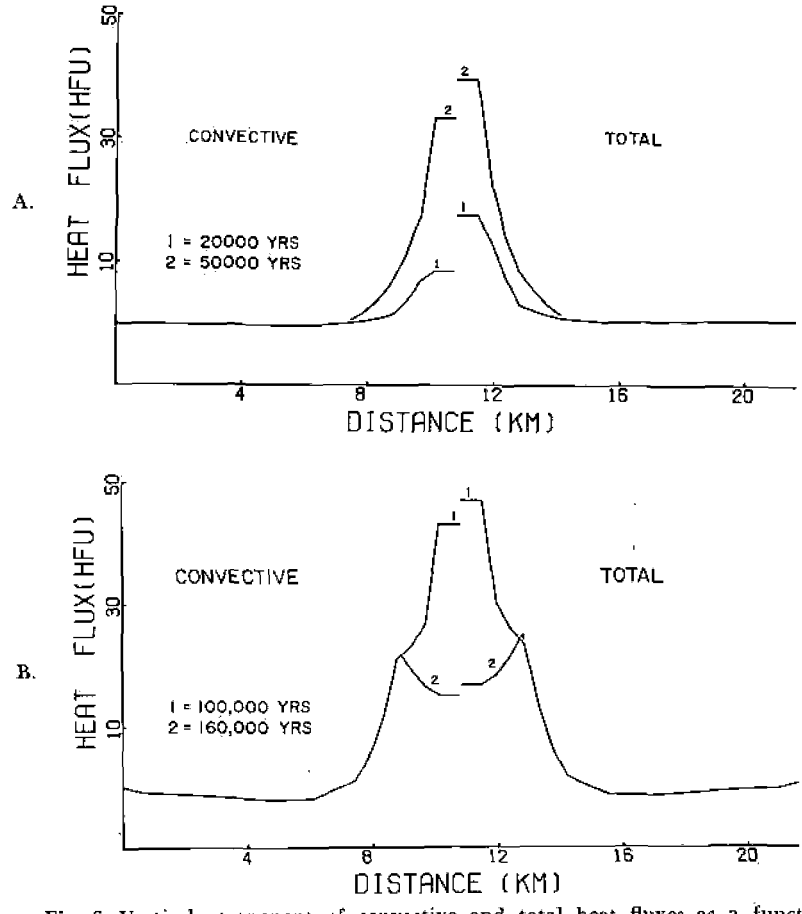

Fig. 6: Vertical component of convective and total heat fluxes as a function of distance along a horizontal plane coincident with the top of P3 pluton at elapsed times of (A) 2×10^4 yrs and 5×10^4 yrs, and (B) 10^5 yrs and 1.6×10^5 yrs.

at 2×10^5 yrs. The total heat flux across the pluton top decreases as the top portion cools. However, the large thermal gradient associated with the side contacts maintains the large heat flux in this region (fig. 6).

Convective heat flux is a nonlinear function of permeabilities, increases rapidly at 10^{-14} cm^2, becomes greater than the conductive heat flux function at 10^{-13} cm^2, then increases at a decreasing rate through P3 such that as permeability becomes infinite the heat flux becomes constant, as required by free convection in a single phase system (fig. 7).

Isotherms in P3 are more convex upward than in P1 and P2 and are displaced closer to the surface and inward toward the side contacts at comparable cooling times. This suggests that the distribution of temperature diagnostic mineral assemblages and fluid inclusions around the side contacts of plutons are useful in ascertaining the relative magnitude

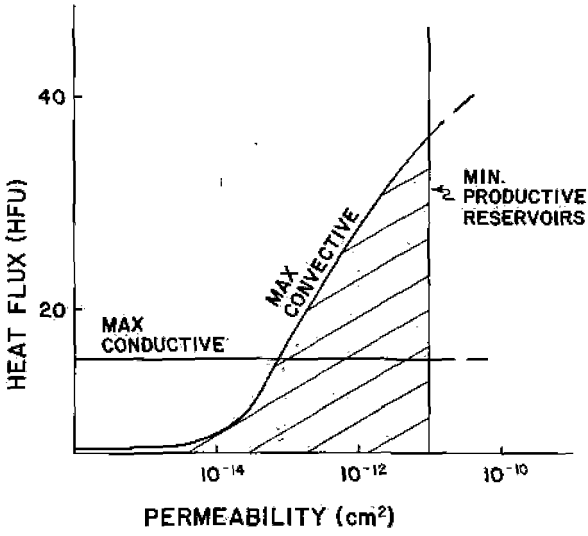

Fig. 7. *Maximum* vertical heat fluxes calculated at top of pluton as a function of host rock permeability, showing maximum model values for convection and conduction. At point $k = 10^{-14}$ cm^2 convective heat flux is approximately 10 percent of total heat flux. The minimum permeability at which geothermal fluids are produced is represented by the vertical line at $k = 10^{-13}$ cm^2 or about 1 millidarcy permeability.

of convective and conductive heat fluxes. At elapsed time = 1.6×10^5 yrs, the 200°C isotherm is shifted toward the pluton with respect to P1. The relatively large vertical heat flux transports thermal energy to the top boundary faster than it can be dispersed through the conductive but impermeable surface, and horizontal fluxes associated with the upward migrating circulation cells produce a plumose pattern in the isotherms (right half of 4C and D). As a result, regions of uniform temperature much broader than the thermal source are produced.

Temperatures in the P3 pluton decrease in a similar manner to the P1 and P2 plutons, since they are cooling essentially by conduction, (figs. 8A and 3); however, the rate of temperature decrease in P3 is greater as a result of increased heat transfer away from the boundaries caused by fluid circulation. Temperature variations with time in the overlying host rocks are complex (fig. 8A), especially when compared to P1 (fig. 3). This complexity is apparently a manifestation of the transport properties of the circulating fluid, the relative rate of conductive and convective heat flux, and numerical effects. The first temperature maxima at $t = 4 \times 10^5$ yrs occurs in response to convection along the pluton margins and conduction from the pluton. This maxima is analogous to the maxima in P1, except it occurs at smaller elapsed time and is greater in magnitude. The temperature in both systems gradually decreases after this maxima (fig. 3); however, in P3 the temperature increases to a second maxima. These temperature fluctuations with time may be caused by the fluid transport properties. As the fluid column

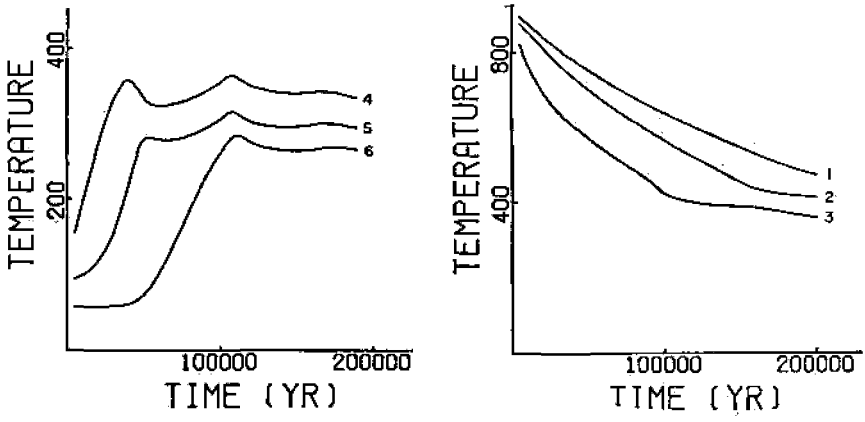

Fig. 8. Temperature as a function of time in system P3 at positions (A) 4, 5, and 6, above top of pluton, 0.45, 1.3, and 3.2 km, respectively, and (B) 1, 2, and 3, below top of pluton, 3.2, 2.3, and 0.45 km, respectively.

above point 4 is heated, fluid density decreases, and, consequently, pressure decreases. Viscosity, thermal coefficient of expansion, and heat capacity of the fluid, therefore, increase, but alpha increases more rapidly than viscosity or heat capacity (paths A and B, fig. 9).

Supercritical-fluid phase properties near the H_2O–system critical end point are continuous and show coincidence of C_p and α maxima and near coincidence of the viscosity minimum in the fluid properties.[3] This maximizes the heat flux at temperatures between 350° to 550°C (fig. 10). Over this temperature range bouyancy forces and heat transport properties are maximized, and the viscous drag force is minimized. Therefore, as conditions in a hydrothermal system cross the extrema in fluid properties from low to high temperature or from high to low pressure, the fluid's heat transport capability first increases then decreases. Therefore, small fluctuations in pressure and temperature may produce large variations in transport properties and cause multiple thermal pulses. Furthermore, in systems whose temperature and pressure conditions do intersect the two-phase surface, the broad oscillations in the temperature-time plot become sharp discontinuities. However, the numerical approximation of the differential equations has contributed an unknown amount to this phenomena. Clearly, the finite difference approximation of alpha across its maxima requires small differential pressure and temperature values. Therefore, we feel that the overall nature of the temperature time plots is realistic but that smaller time period oscillations may be numerical artifacts.

Broad aspects of the temperature-pressure variations in the system define some physical constraints on the development of a two-phase,

[3] The analogous feature is realized in NaCl–H_2O systems, only it is shifted to higher temperatures and pressures because of the corresponding shift in the critical end point.

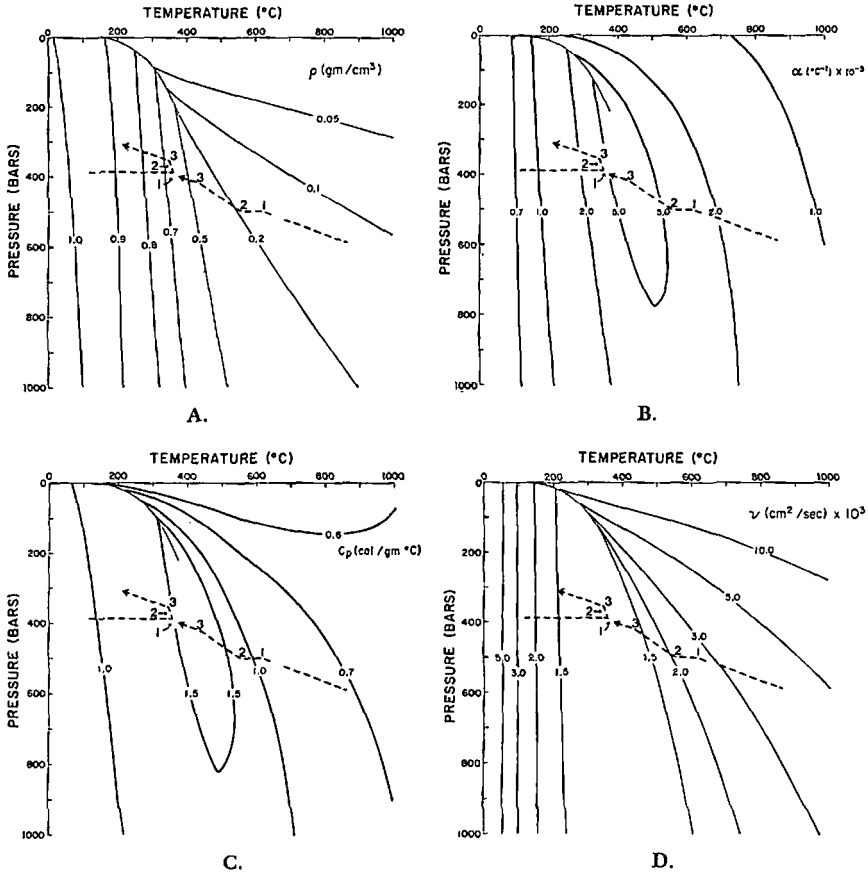

Fig. 9. Temperature-pressure projections of liquid-vapor surface and transport properties of phases in H_2O-system depicting transient temperature and pressure conditions at a position in host rocks 0.45 km above P3 pluton, left dashed line, and 0.45 km below pluton top, right dashed line. Numbers on the dashed lines correspond to maxima on the temperature versus time plot at position 4 in figure 8A. Temperature-pressure variations are shown relative to transport properties: (A) density, ρ, (B) isobaric thermal coefficient of expansion, α, (C) heat capacity at constant pressure, C_p, and (D) viscosity, ν.

liquid-vapor, region. Plutons that are emplaced at depths where the confining pressure is greater than the critical end point pressure do not develop a two-phase system by simple upward transfer of heat. This is evident if we examine the derivative fluid properties along the maximum, for example, for α and C_p, from 1 kb and 450°C to the critical end point (fig. 10). Both α and C_p increase, thereby increasing the transport capability of the fluid and preventing the system's conditions from reaching the two-phase surface.

Stratified.—Plutons emplaced into the upper 10 km of the crust often intrude stratified rocks. Volcanic or sedimentary rock sequences inevitably

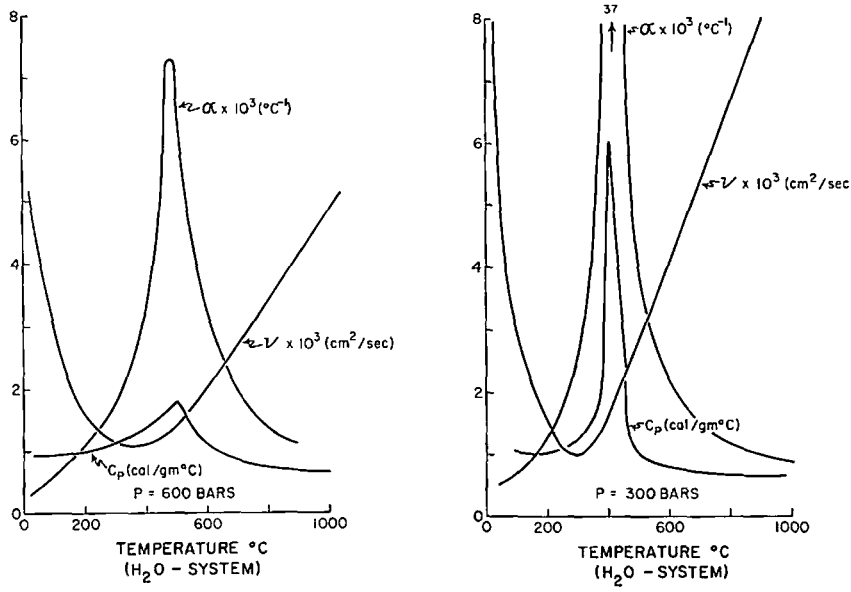

Fig. 10. Thermodynamic and transport properties of supercritical fluid in the H_2O system. The variation of the isobaric coefficient of thermal expansion, α, isobaric heat capacity, C_p, and viscosity, ν, with temperature at (A) 600 bars and (B) 300 bars pressure.

have vertical variations in permeability that may affect the style of fluid circulation and, consequently, the pluton's cooling history. This type of system is simulated by P4, which consists of a pluton intruded into a layered stratigraphic sequence (fig. 11).

Stratified rocks confine fluid circulation to the more permeable layers (fig. 12). Streamlines are refracted at permeability discontinuities, but since the streamlines are developed into circular like cells, the refraction often does not appear to coincide with the actual physical

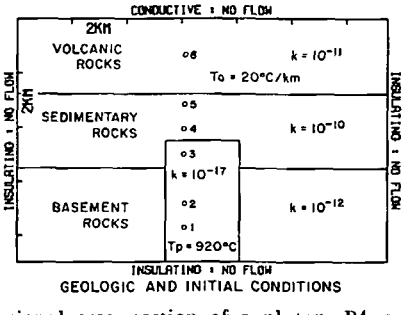

Fig. 11. Two-dimensional cross section of a pluton, P4, and stratified host rocks. Boundary conditions and (left) geologic conditions are depicted for an impermeable pluton emplaced at 920°C; (right) initial conditions depicted for a temperature of 20°C at the top boundary and a thermal gradient of 20°C/km. Constant permeability was maintained in the host rocks, but stepwise permeability increases were included for the upper portion of the pluton in order to simulate fracturing. The domain was represented by 160 grid points at regular intervals, $\Delta z = 0.9$ km and $\Delta y = 1.35$ km.

boundary. This style of fluid circulation accentuates the displacement of isotherms toward the sides of the pluton (right half of 12D; right half of 13A). The plumose outline of isotherms noted in P3 is not as well developed in P4, nor do the isotherms reach as near to the surface. The thermal energy dispersed laterally into the permeable unit is redispersed by conduction and results in a very broad doming of the isotherms in the upper portion of the system (see 100°C, right half of fig. 12A).

Time.—The effective stresses associated with the emplacement of magmas, their crystallization, and concomitant heating of the surrounding host rocks produce systematic and relatively abundant fractures in plutons and host rocks. Although the distribution of fracturing in time is poorly known, the crosscutting relationships observed in natural systems suggest a complex sequence of fracturing events. Crystallization of fluid bearing magmas may release substantial mechanical energy; therefore, the P4 pluton's permeability was increased early in its cooling history to simulate fracturing. Permeability variations were chosen arbitrarily, but the time of fracturing was chosen when the temperature decreased to ~ 860°C. Fracturing was approximated by an instantaneous increase in permeability.

The upper 0.9 km portion of the pluton was fractured at t = 1250 yrs, and permeability was increased to 10^{-11} cm^2 (left half of fig. 13A).

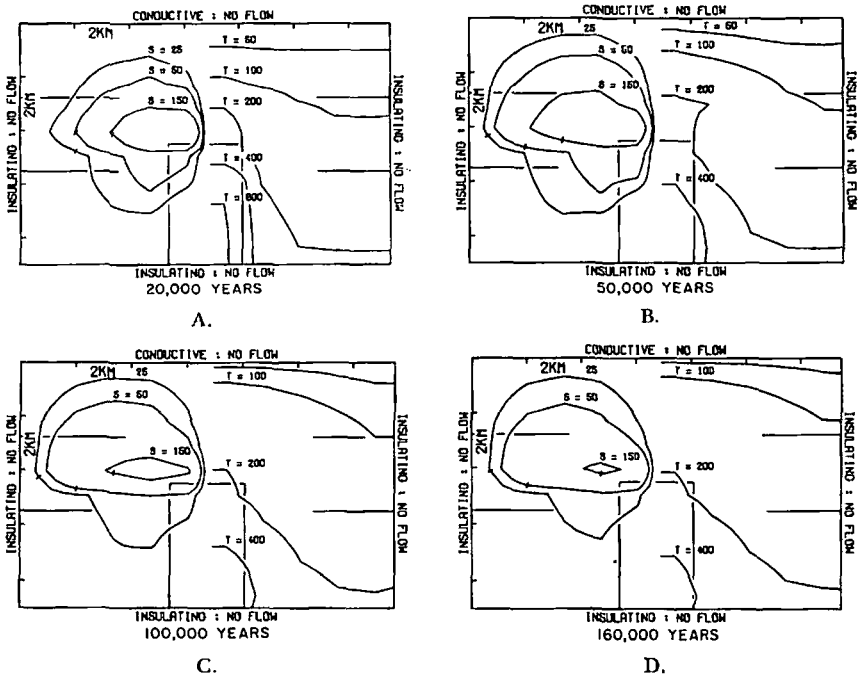

Fig. 12. Steady state (left) dimensionless streamfunction and (right) temperature distribution in system P4. Horizontal broken lines depict stratified permeability boundaries, (A) at 2 × 10^4 yrs, (B) at 5 × 10^4 yrs, (C) at 10^5 yrs, (D) at 1.6 × 10^5 yrs.

Comparison of the pre-fracture fluid circulation at t = 1200 yrs (left half of fig. 13B) with the post-fracture pattern at t = 2000 (left half of fig. 13C) illustrates both the deeper penetration of flow into the pluton and increasing fluid fluxes (table 2). A second fracture event at t = 5000 yrs (right half of fig. 13D) increased permeability to 10^{-10} cm^2 in the upper 0.9 km of the pluton and to 10^{-12} cm^2 in the next lower 1.8 km. Again the fluid circulation at t = 5×10^3 yrs (left half of fig. 13D) and at t = 2×10^4 yrs (left half of fig. 12A) illustrates the effect of the permeability increase.

The two increases in pluton permeability over 5×10^3 yrs have a dramatic effect on the fluid flux and thermal decay of the pluton (fig. 14). Specifically, the upper 0.9 km of the pluton cools at 0.12°C/yr for 5000 yrs, and the next lower 1 km cools at 0.02°C/yrs for 17500 yrs; thereafter temperature decreases at 10^{-4}°C/yr in both regions. Consequently, the temperature in the upper 2 km averages 260°C for 2×10^5 yrs. The coincidence of emplacement into shallow portions of the crust and thorough fracturing of the pluton rapidly cools the entire body to temperatures between 200° to 400°C.

Increased permeability increases fluxes in both the vertical and horizontal directions such that the thermal energy is more quickly dispersed.

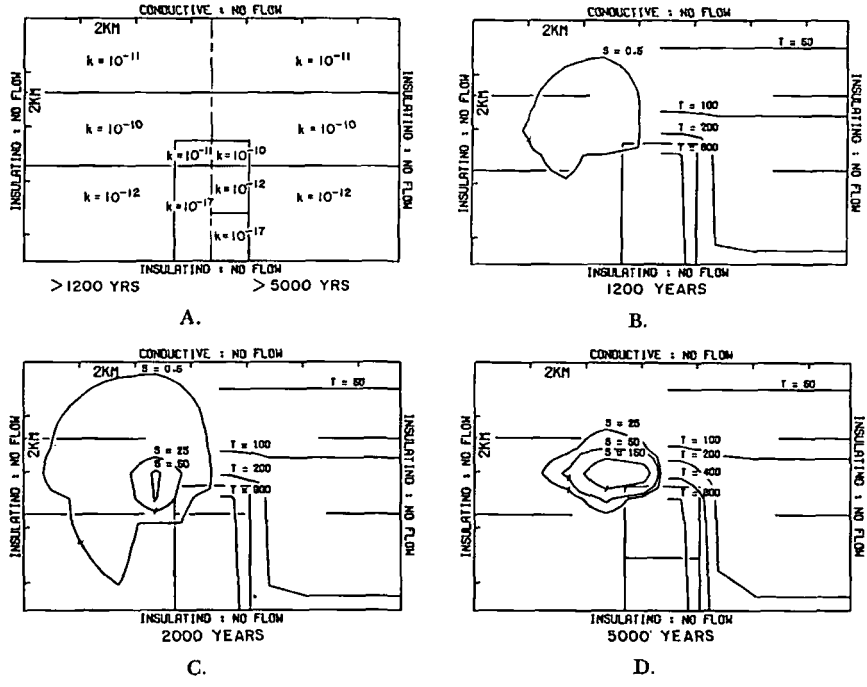

Fig. 13. Thermal history of P4 during short elapsed times when pluton permeability was increased to simulate fracturing. (A) Permeability distribution in systems (left) 1200 yrs < t < 5000 yrs (right). (B–D) Steady state (left) dimensionless streamfunction and (right) temperature distribution in system P4. Horizontal broken lines in host rocks and horizontal solid lines in pluton depict stratified permeability boundaries at (B) 1200 yrs, (C) 2000 yrs, (D) 5000 yrs.

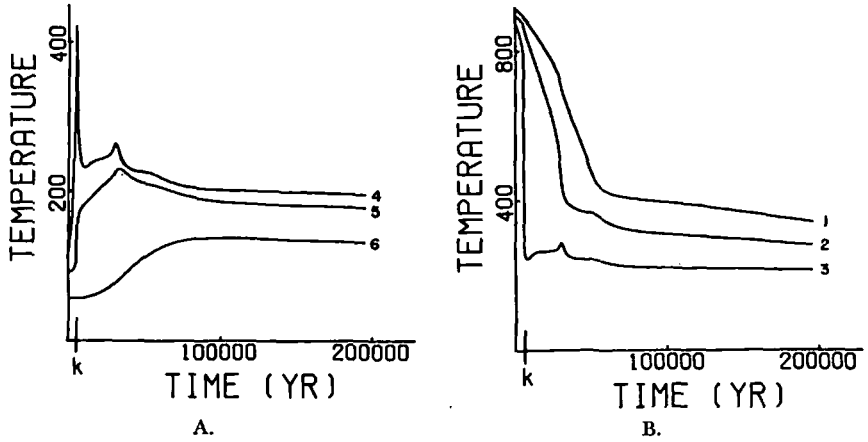

Fig. 14. Temperature as a function of time in system P4 at fixed points (A) 4, 5, and 6, above top of pluton, 0.45, 1.3, and 3.2 km, respectively, and (B) 1, 2, and 3, below top of pluton, 3.2, 2.3, and 0.45 km, respectively. Symbol k denotes approximate times at which pluton permeability was increased in order to simulate fracturing.

However, the thermal history at a position 4 km above the pluton does not reveal evidence of the pluton fracturing.

Fracture zone.—Conditions where igneous activity is most common are conducive to the formation of numerous fractures, both within the pluton and in host rocks. The effects of fracture controlled permeability within host rocks over the top of the pluton were analyzed using model P5 (fig. 15A).

Fluid circulation is confined to the permeable zone above the pluton. The streamline pattern also differs from previous models, because the system boundaries are open to fluid flow (figs. 15B–D). Circulation cells, centered within the fracture zone, reduce the broad isotherm surface observed in previous systems to a much narrower and larger amplitude surface confined to the fracture zone. The broader low amplitude doming of the isotherms is primarily the result of conduction heat away from the fracture zone (right half of fig. 15D). Temperature variation with time within the pluton follows a normal conductive cooling pattern, except that the upper 1 km of the pluton is cooled at an increased rate by fluid circulation.

Temperatures within the fracture zone are similar in distribution but lower in magnitude than previous systems: Lower values of temperature, relative to model P3, are a result of the narrow, large permeability fracture zone and the height of the thermal anomaly in the fracture zone (figs. 16 and 8). However, the temperature-time curves are quite similar in magnitude to P4 (fig. 14), illustrating the common effect of increased permeability.

Pluton geometry.—The vertical extent of the pluton exposed to permeable host rocks determines the lateral extent of the fluid circulation. This effect was simulated by model P6, where the vertical exposure of the pluton was decreased to 2.7 km by introducing a layer of 10^{-17}

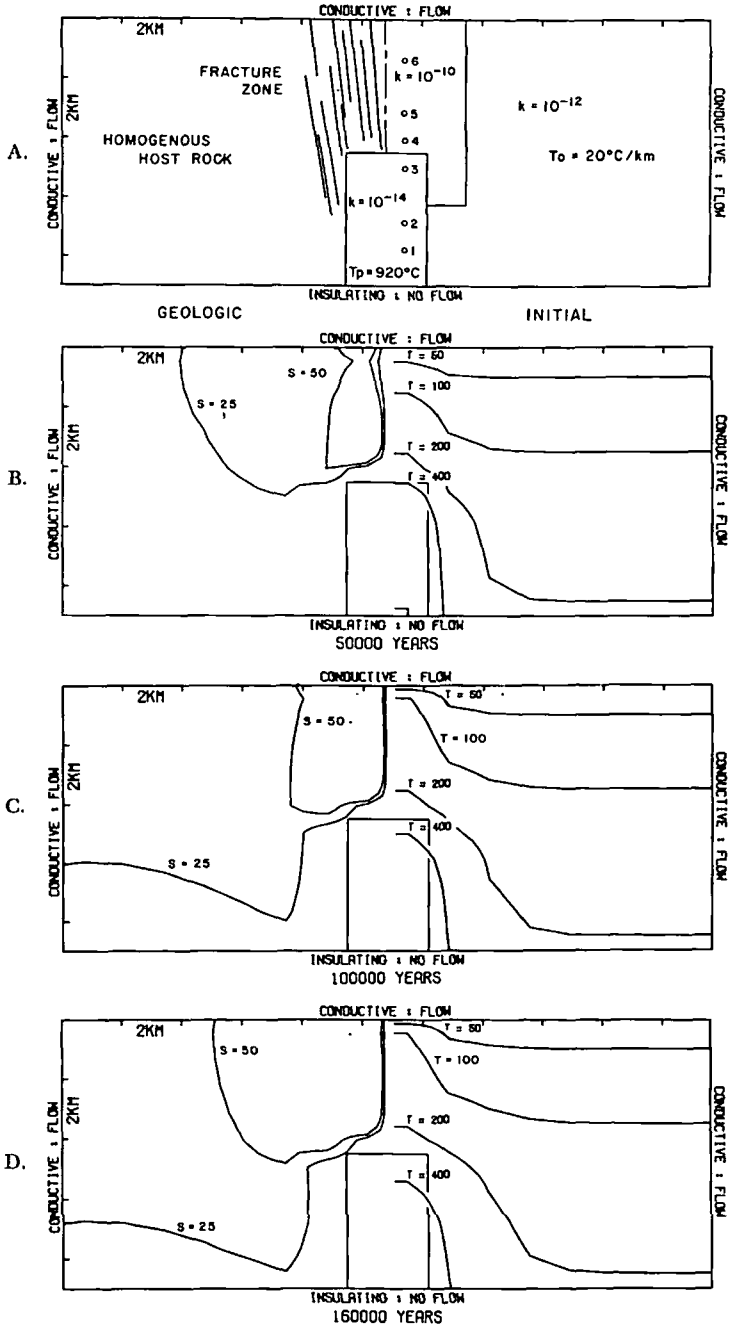

Fig. 15. Two-dimensional cross section of system P5 depicting boundary conditions and (A) initial (left) and geologic (right) conditions for anomalously high permeability zones directly over the top of pluton. Pluton is emplaced at 920°C into host rocks whose temperatures are defined by 20°C top boundary temperature and a 20°C/km thermal gradient. The domain was represented by 160 grid points at regular intervals, $\Delta z = 0.9$ km and $\Delta y = 1.35$ km. (B–D) Steady state (left) dimensionless streamfunction at (B) 5×10^4 yrs, (C) 10^5 yrs, (D) 1.6×10^5 yrs; (right) temperature distribution at (B) 5×10^4 yrs, (C) 10^5 yrs, (D) 1.6×10^5 yrs.

cm^2 permeability across the base of the domain (fig. 17A). In the upper portion of the system heat is transferred away from the pluton by convection. Fluid circulation is centered over the side contact and 1 km above the top of the pluton at 5×10^5 yrs and migrates upward 1 km by $t = 1.6 \times 10^5$ yrs (fig. 17, B–D). However, in P3, fluid circulation is centered in the host rocks laterally away from the side contact, as well as above the top contact (fig. 4, B–D). The height of the circulation cells is less in P6 than in P3, and the lateral extent of the cells is also proportionately smaller. The ratio of the cell widths is approximately equal to the ratio of the effective pluton heights for the two systems. Therefore, plutons with the larger effective heights will cause fluid circulation a greater distance from their side contacts.

The convective heat flux at $t = 2 \times 10^4$ yrs is equivalent over the plutons in both P3 and P6, but P6 has 10 percent greater flux along its side margins (figs. 6A and 18). This difference increases to 50 percent between 5×10^4 yrs and 10^5 yrs, then decreases to 45 percent at 1.6×10^5 yrs (fig. 19). These differences between the two systems are also evident in the temperature variations with time, although the initial temperature increase above the pluton tops is nearly identical, figures 20 and 8. The second inflection point in each of the temperature-time curves is shifted to earlier times and is of lower magnitude for the shorter pluton.

Level.—Plutons emplaced at levels < 2.2 km generate initial conditions that include two-phase fluid flow with respect to H_2O–systems; those emplaced at increasing depth greater than 2.2 km generate thermal anomalies that are proportionately more extended in the vertical direction. The theory and numerical equations used in this study do not afford for two-phase flow; therefore, the effect of pluton emplacement at depths greater than 2.2 km was examined. The effective height of pluton P7 in permeable rocks is 2.7 km, equivalent to P6, but P7 is 6.3 km deep (left half of fig. 21A).

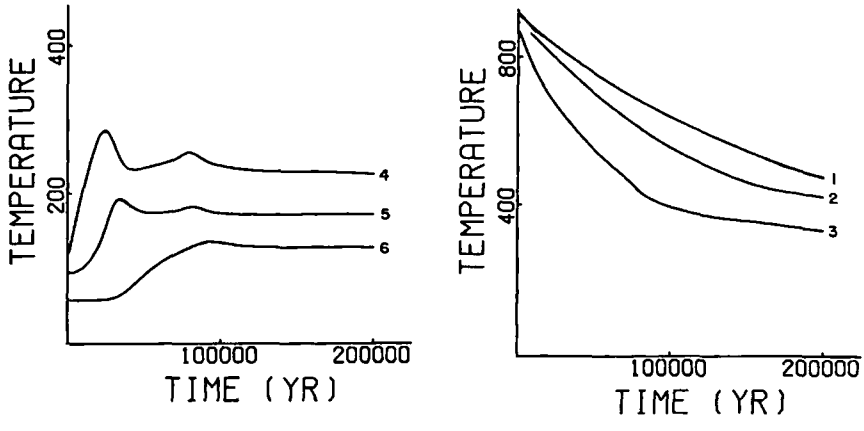

Fig. 16. Temperature as a function of time in system P5 at fixed positions (A) 4, 5, and 6, above top of pluton, 0.45, 1.3, and 3.2 km, respectively, and (B) 1, 2, and 3, below top of pluton, 3.2, 2.3, and 0.45 km, respectively.

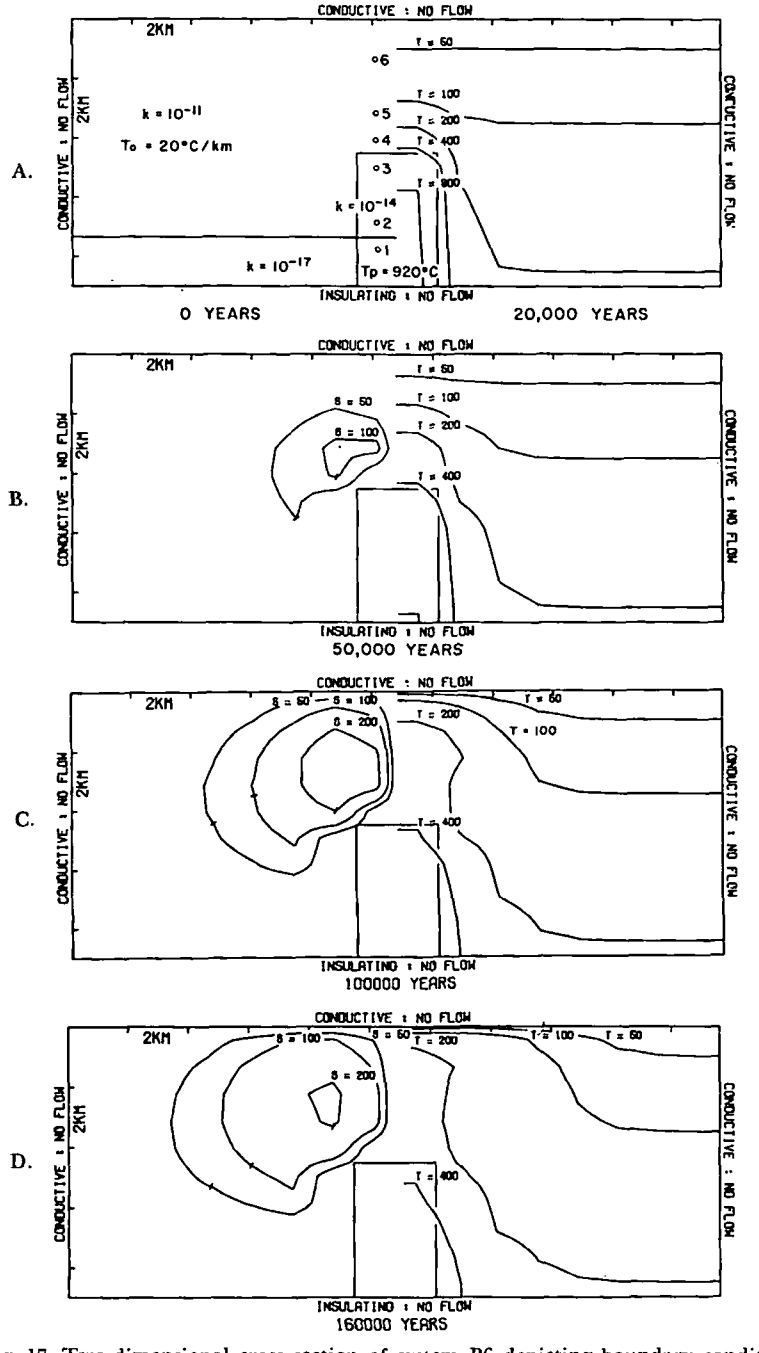

Fig. 17. Two-dimensional cross section of system P6 depicting boundary conditions and (left): (A) initial conditions for pluton identical to P3 except for low permeability layer at base of system. (B–D) Steady state dimensionless streamfunction at (B) 5×10^4 yrs, (C) 10^5 yrs, (D) 1.6×10^5 yrs; (right) temperature distribution at (A) 2×10^4 yrs, (B) 5×10^4 yrs, (C) 10^5 yrs, (D) 1.6×10^5 yrs.

Fluid circulation is similar initially around plutons P7 and P6 since the thermal perturbation with respect to the surroundings is similar (left half of fig. 21B). However, as the thermal anomaly from P7 becomes dispersed over the 6.3 km between the top of the pluton and the surface, larger circulation cells develop (left half of fig. 17D and left half of fig. 21D). This extension of the anomaly results in a plumose isotherm pattern similar to the taller and shallower pluton in P3 but is less extensive in width and height because of the lower total energy content of the P7 pluton (right half of figs. 21C, 21D, and 4D).

Width.—A batholith size pluton was simulated with model P8 (fig. 23). Fluid circulation in P8 is similar to other systems but is upward along the side contacts of the relatively impermeable pluton around the top corner and upward from the top contact (left half of figs. 23D–F).

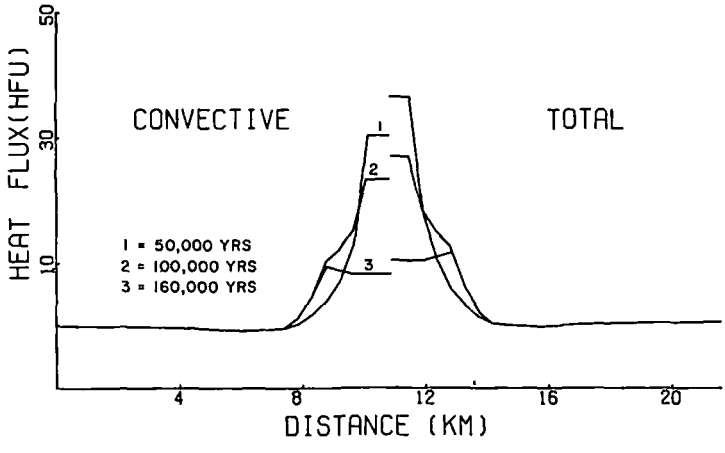

Fig. 18. Vertical component of convective and total heat fluxes as a function of distance along a horizontal plane coincident with the top of P6 pluton at elapsed times of 5×10^4 yrs, 10^5 yrs, and 1.6×10^5 yrs.

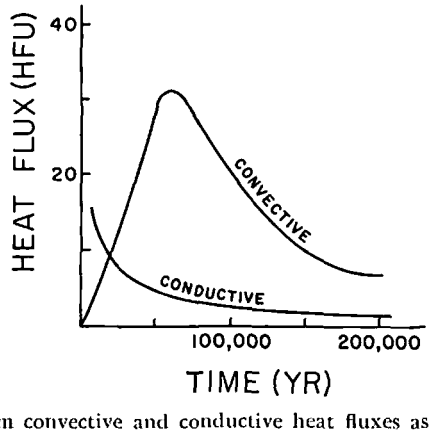

Fig. 19. Maximum convective and conductive heat fluxes as a function of time at top of P6 pluton.

This flow style eventually generates a secondary thermal perturbation due to the width of the pluton (right half of fig. 23F). The effect of the pluton width is to delay the development of fluid circulation over the top of the batholith. Therefore, upward displacement of isotherms is less over the pluton top than at its sides (right half of figs. 23D–F). This lateral temperature perturbation produces secondary circulation cells. These circulation cells further accentuate the temperature anomaly by depressing the isotherms in the central downflow zone (right half of fig. 23F). The secondary cells eventually dominate over the fluid circulation along the side contacts (left half of fig. 23F), and circulation breaks up into 4 Bénard-like cells (Bénard, 1901). As a consequence of this circulation pattern, a 60 km^2 region over the top of the batholith remains at 400°C for 10^6 yrs.

Undoubtedly, the perfectly flat top pluton which extends for 54 km is geologically unreasonable. However, it does indicate an extreme condition which, together with the stock sized plutons in previous models, can be used to analyze the nature of heat transport from a batholith sized body which may have stocks protruding from its upper boundary or for a broad convex topped batholith. Batholiths with convex tops tend to decrease the tendency for secondary cells to develop. Irregular topography, consisting of apical stocks on the batholith top, will develop secondary convective cells around each topographic feature.

Relative cooling rates.—Differences in the cooling rates are insignificant for systems for which pluton size and permeability are equal (table 3). Although large fluid flux occurs along the margins of systems P3 and P6, this does not increase the cooling rate of the pluton significantly. Fluid circulation has its greatest effect in redistributing the thermal energy upward toward the surface as opposed to laterally away from the

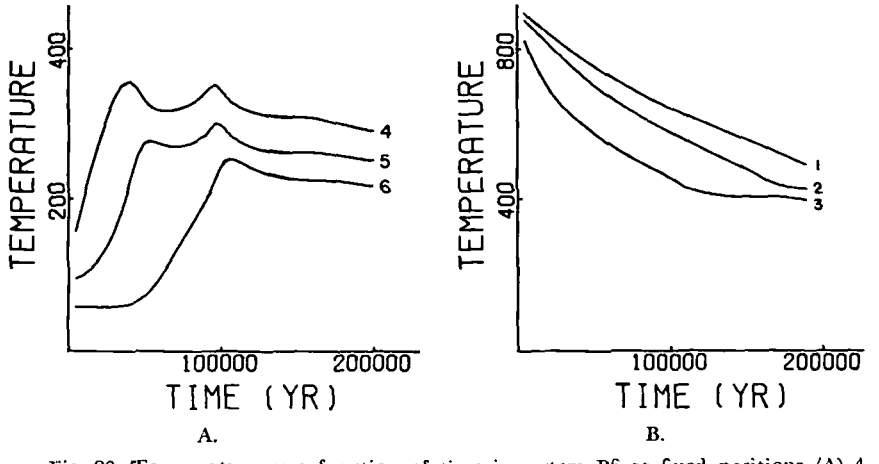

Fig. 20. Temperature as a function of time in system P6 at fixed positions (A) 4, 5, and 6, above top of pluton, 0.45, 1.3, and 3.2 km, respectively, and (B) 1, 2, and 3, below top of pluton, 3.2, 2.3, and 0.45 km, respectively.

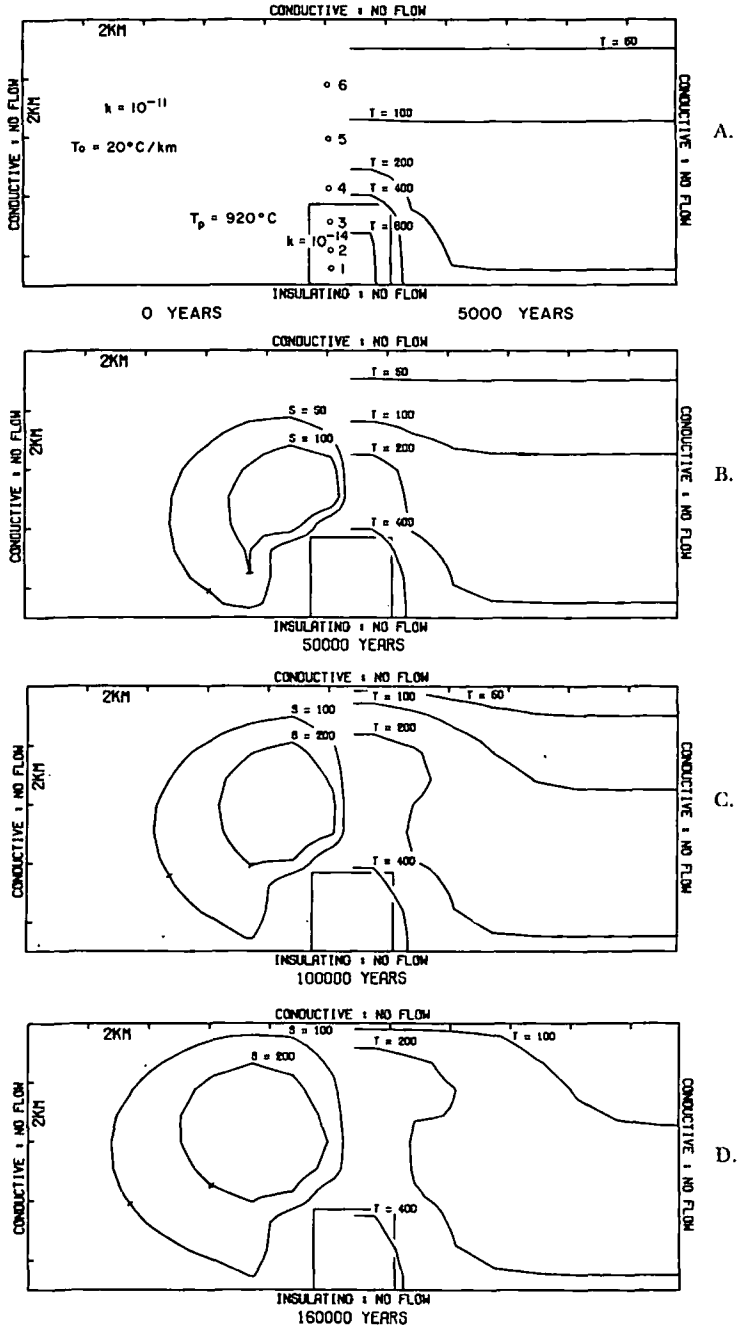

Fig. 21. Two-dimensional cross section of system P7 depicting boundary conditions and (A) initial conditions (left) for a 2.7 km tall pluton emplaced at 920°C into uniform permeability host rocks. Host rock temperature and permeability are same as system P3. The domain was represented by 160 grid points, $\Delta z = 0.9$ km and $\Delta y = 1.35$ km. (B–D) Steady state (left) dimensionless streamfunction at (B) 5×10^4 yrs, (C) 10^5 yrs, (D) 1.6×10^5 yrs; (right) temperature distribution at (A) 5×10^3 yrs, (B) 5×10^4 yrs, (C) 10^5 yrs, (D) 1.6×10^5 yrs.

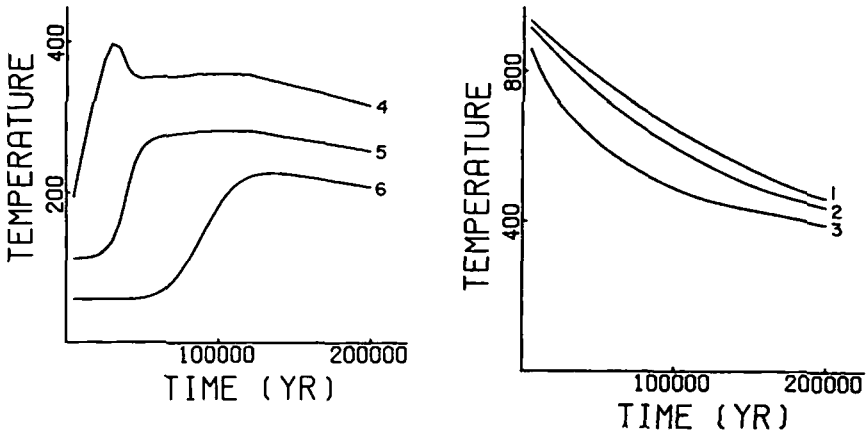

Fig. 22. Temperature as a function of time in system P7 at fixed points (A) 4, 5, and 6, above top of pluton, 0.45, 1.3, and 3.2 km, respectively, and (B) 1, 2, and 3, below top of pluton, 3.2, 2.3, and 0.45 km, respectively.

pluton. Plutons with permeabilities 10^{-14} cm^2 tend to cool much more rapidly than their relatively impermeable counterparts, compare P4 with P3.

Fluid redistribution.—The redistribution of large quantities of fluid is a direct consequence of fluid circulation in pluton environments. This redistribution and concomitant changes in temperature and pressure give rise to an overall irreversible chemical interaction between fluids and minerals. The purpose of this section is to examine some of the features of fluid redistribution in model systems.

Fluid circulation is represented by the distribution of streamlines in each of the systems; however, of more direct interest to mass transport computations is the actual distance and path along which a given fluid packet moves during the thermal event. These fluid pathlines, as defined by eq (36), are analogous to a time exposure of a single fluid packet as it circulates through the system. Pathlines for fluid packets whose origins are in various portions of a system are dependent on the rock permeability and proximity of the path origin to the thermal anomaly (figs. 24, 26, 28, 30, and 32). Fluids initially in the upper portions of low permea-

TABLE 3

Pluton cooling rates

System	Fraction of initial anomaly after 2×10^5 yrs	
P1	0.4	conduction
P3	0.4	convection in host rocks
P4	0.2	permeable pluton
P5	0.4	fracture zone in host rocks
P6	0.4	less exposed in impermeable rocks
P7	0.3	shorter and deeper pluton
P8	0.8*	batholith

* 0.45 after 1.2×10^6 yrs

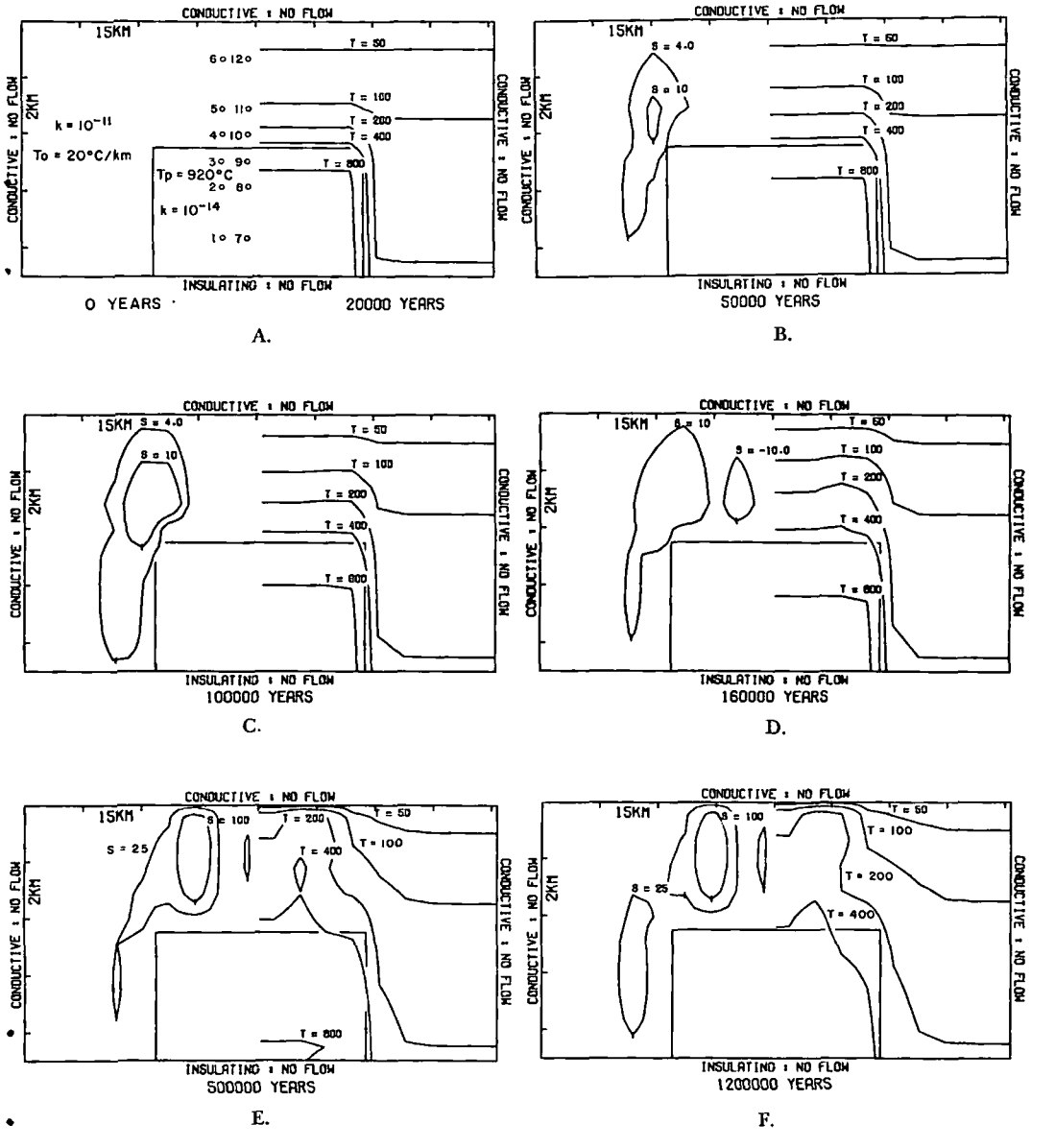

Fig. 23. Two-dimensional cross section of system P8 depicting boundary conditions and (A) initial conditions (left) for batholith size intrusive emplaced into domain with conditions similar to P3. The domain is represented by 180 grid points, $\Delta z = 0.9$ km and $\Delta y = 6.75$ km. (B–D) Steady state (left) dimensionless streamfunction at (B) 5×10^4 yrs, (C) 10^5 yrs, (D) 1.6×10^5 yrs, (E) 5×10^5 yrs, (F) 1.2×10^6 yrs; (right) temperature distribution at (A) 2×10^4 yrs, (B) 5×10^4 yrs, (C) 10^5 yrs, (D) 1.6×10^5 yrs, (E) 5×10^5 yrs, (F) 1.2×10^6 yrs.

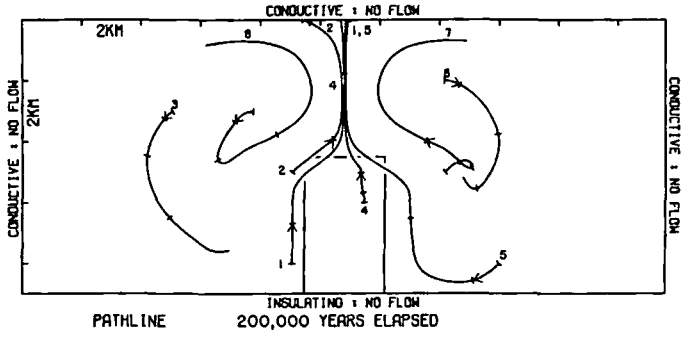

Fig. 24. Examples of fluid pathline in system P3 representing the redistribution of fluids caused by the thermal anomaly. Arrows indicate direction of fluid motion; tic marks occur every 5×10^4 yrs.

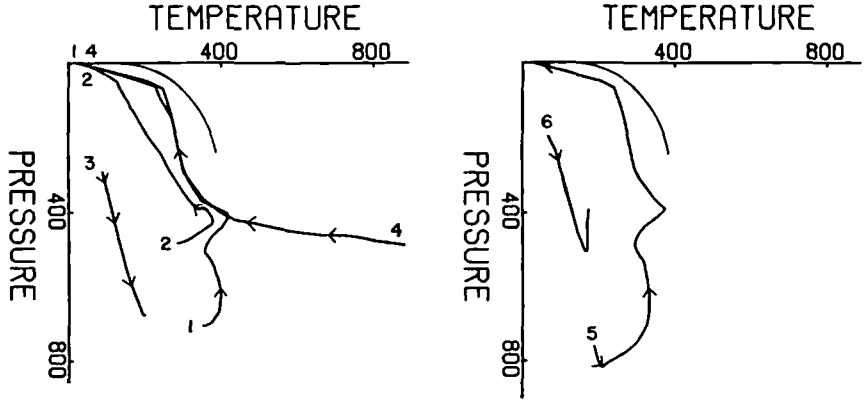

Fig. 25. Pressure-temperature path of fluid packets that circulate along paths in system P3 (fig. 24). Paths are shown with respect to liquid-vapor surface in H_2O system.

bility plutons flow relatively short distances in the initial 10^5 yrs (for example, 1 km in systems P3, P5–P7, figs. 24, 28, 30, and 32). During the subsequent 10^5 yrs fluid circulation increases enough in the upper portions of the pluton to transport fluid packets several km into the overlying host rocks. Fluids initially in larger permeability plutons are transported completely out of the pluton in the initial 10^5 yrs (fig. 26). As a result, this fluid is replaced by fluid packets circulating along pathlines into the sides of the pluton.

Fluids initially in host rocks several km away from the pluton convect toward and into the pluton (fig. 24). The pathlines trend along the side contacts of low permeability plutons, whereas they flow into the plutons with larger permeability (fig. 26). As the fluids move horizontally toward the pluton, the circulation center migrates upward in the system. Therefore, pathlines with origins above the pluton tend to form upward looping spirals. Stratified permeabilities restrict pathline movement to

the larger permeability units. In P4 layered units force the circulation toward the pluton (fig. 26), and, since P4 is a relatively permeable pluton, fluid packets then circulate through the pluton.

Fracture zones effectively channel the fluid up through the fracture zone. Pathlines in the vertical fracture zone are proportionately longer than those in the adjacent, less permeable rocks (fig. 28). Transit time for these packets from the top of the pluton to the surface is 10^5 yrs.

Changes in temperature and pressure along fluid pathlines describe a path through the H_2O system along which the solvent properties of the fluid may be described and define the intensive variables required to calculate mass transfer between fluid and rock. Packets of supercritical fluid, whose temperatures are in the critical endpoint region, are subjected to drastic changes in thermodynamic and electrostatic properties (figs. 25, 27, 29, 31, and 33). Extreme variations in thermodynamic behavior of the solvent along these paths are apparent from the work by Helgeson and Kirkham (1974a,b).

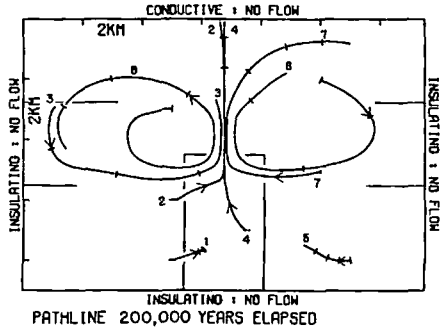

Fig. 26. Examples of fluid pathline in system P4 representing the redistribution of fluids caused by the thermal anomaly. Arrows indicate direction of fluid motion; tic marks occur every 5×10^4 yrs.

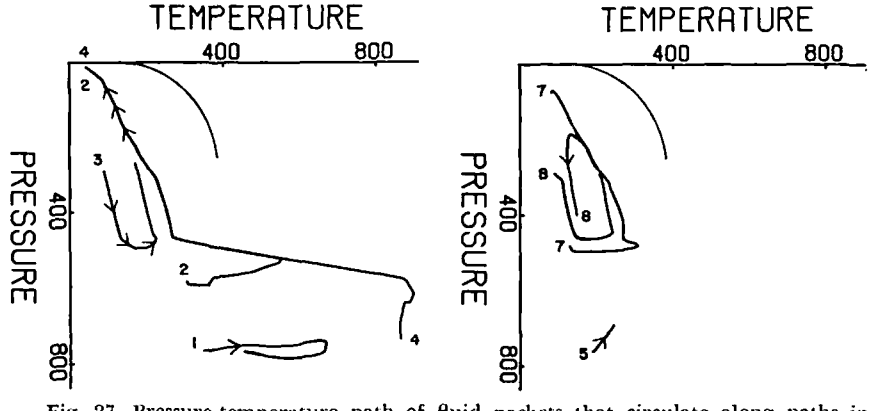

Fig. 27. Pressure-temperature path of fluid packets that circulate along paths in system P4 (fig. 26). Paths are shown with respect to liquid-vapor surface in H_2O system.

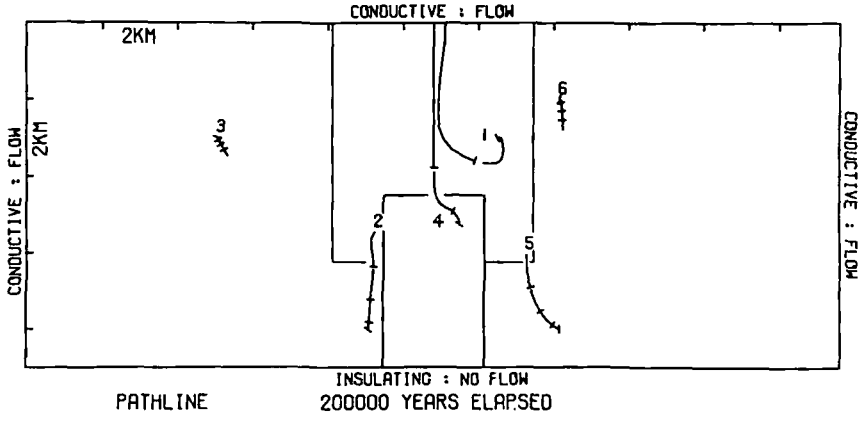

Fig. 28. Examples of fluid pathline in system P5 representing the redistribution of fluids caused by the thermal anomaly. Arrows indicate direction of fluid motion; tic marks occur every 5×10^4 yrs.

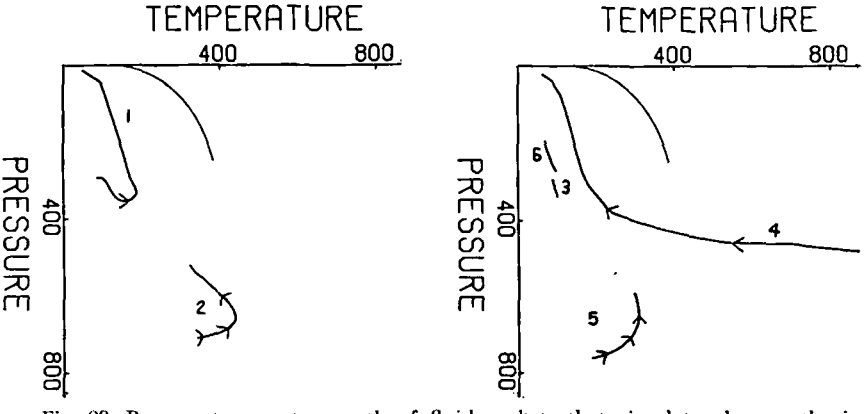

Fig. 29. Pressure-temperature path of fluid packets that circulate along paths in system P5 (fig. 28). Paths are shown with respect to liquid-vapor surface in H_2O system.

Enormous quantities of fluid are circulated through pluton environments where thermal convection is the predominant cooling process. The total mass of fluid circulating through a unit area, integrated over a time interval of 2×10^5 yrs for each system (table 4), is considerably less for low permeability plutons than for the fractured plutons.

The mass of fluid that flows during time interval t_2–t_1, through an area, A, normal to a fluid pathline is defined by

$$M_f = A \int_{t_1}^{t_2} \rho_f \bar{v} dt, \tag{58}$$

where $\bar{v}$ is the Darcy velocity and ρ_f is the density of the fluid. The mass

of rock exposed to the circulating mass of fluid is defined in terms of the true velocity, $\bar{v}_t$, of the fluid:

$$M_r = A\,(1-\phi)\int_{t_1}^{t_2} \rho_r \bar{v}_t dt, \tag{59}$$

where ϕ is the flow porosity and ρ_r is the density of the rock. The mass ratio of circulating fluid to rock contacted by the fluid is the ratio of eqs (58) and (59), if the average fluid velocity over the time interval is used:

$$\frac{M_f}{M_r} = \frac{\phi}{1-\phi}\,\frac{\int_{t_1}^{t_2} \rho_f dt}{\int_{t_1}^{t_2} \rho_r dt}, \tag{60}$$

since the true velocity is related to the Darcy velocity by

$$\bar{v}_t = \frac{\bar{v}}{\phi}. \tag{61}$$

The rock density is nearly constant over temperature ranges realized in pluton environments, and the fluid density varies from 0.2 to 0.9 g cm^{-3}. Therefore, fluid-rock mass ratios are approximately

$$\frac{M_f}{M_r} \approx \frac{\phi\,\rho_f}{(1-\phi)\,\rho_r}. \tag{62}$$

TABLE 4

Mass of fluid circulated through systems (g cm^{-2} × 10^5)

Position	System P3	P4	P5	P6	P7
1	0.3	0.02	0.3	trace	trace
2	0.5	4	0.4	0.5	0.4
3	0.7	24	0.6	0.5	0.5
4	22	35	20	15	20
5	33	27	30	15	20
6	24	5	20	20	20

TABLE 5

Fluid:rock mass ratios

Position	P3	P4	P5	P6	P7
1	0.05	0.1	0.06	0.07	0.1
2	0.08	0.16	0.1	0.1	0.1
3	0.1	0.3	0.1	0.1	0.1
4	0.25	0.31	0.31	0.26	0.25
5	0.28	0.32	0.33	0.3	0.28
6	0.30	0.33	0.34	0.3	0.30

The effective mass ratio (table 5), defined by eq (60), permits computation of fluid-rock reactions from the viewpoint of a circulating or stagnant fluid. In rocks where the fluid flow is confined to fractures, the flow porosity may be on the order of 10^{-4} to 10^{-5} (Norton and Knapp, 1977), and, therefore, the $(1-\phi)$ term in the denominator is $\cong 1$, and the effective mass ratio is on the order of the flow porosity, since $\rho_r \cong 2.73$ g cm^{-3}. These mass ratios are exceedingly small compared to those predicted from stable light isotope data on hydrothermal systems (Taylor, 1971). The reason for this discrepancy is obvious, since eq (60) defines the mass of rock contacted by a circulating mass of fluid, whereas the isotopic data estimates the integrated effect of all fluid packets circulating through an arbitrary rock mass.

The total mass of fluid that circulates through an arbitrary mass of rock, at a fixed position in a hydrothermal system, is normally used in predicting the amount of isotopic or other chemical exchange that occurs

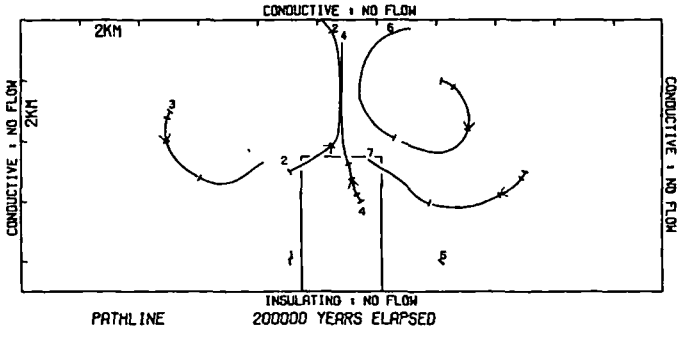

Fig. 30. Examples of fluid pathlines in system P6 representing the redistribution of fluids caused by the thermal anomaly. Arrows indicate direction of fluid motion; tic marks occur every 5×10^4 yrs.

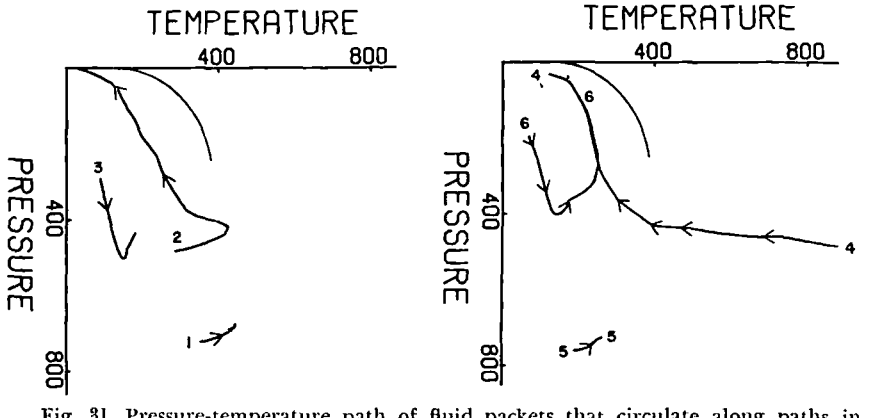

Fig. 31. Pressure-temperature path of fluid packets that circulate along paths in system P6 (fig. 30). Paths are shown with respect to liquid-vapor surface in H_2O system.

between fluid and rock. The amount of fluid flowing through rock volume, V, is

$$M_f = \int_{t_1}^{t_2} A\bar{v}\rho_f dt, \tag{63}$$

where A is the cross-sectional area of the rock volume that is normal to the Darcy velocity vector, $\bar{v}$. The fluid-rock mass ratio in this case is defined by

$$\frac{M_f}{M_r} = \frac{\int_{t_1}^{t_2} A\bar{v}\rho_f dt}{\rho_r V}. \tag{64}$$

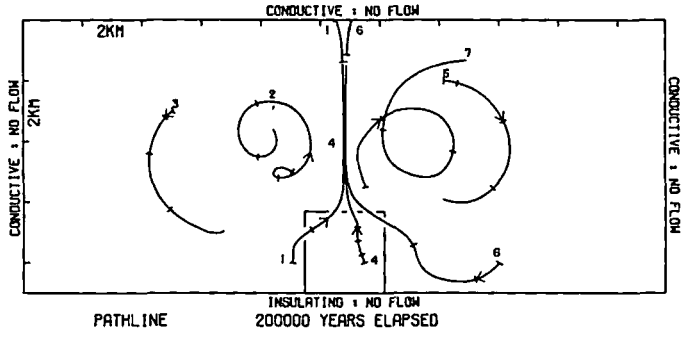

Fig. 32. Examples of fluid pathline in system P7 representing the redistribution of fluids caused by the thermal anomaly. Arrows indicate direction of fluid motion; tic marks occur every 5×10^4 yrs.

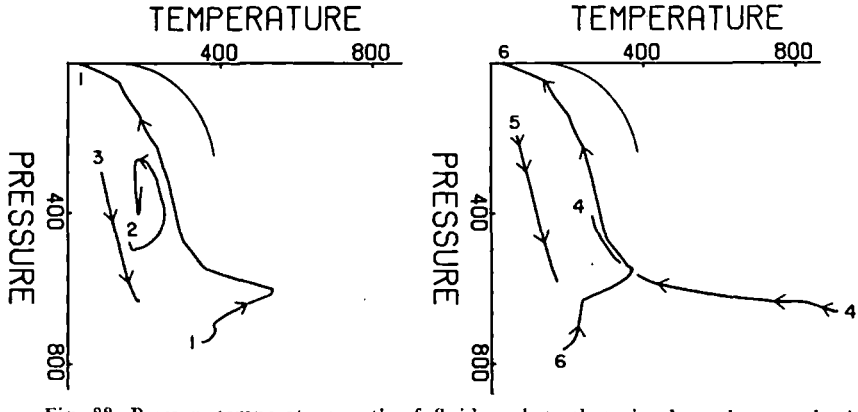

Fig. 33. Pressure-temperature path of fluid packets that circulate along paths in system P7 (fig. 32). Paths are shown with respect to liquid-vapor surface in H_2O system.

This ratio is essentially the integrated amount of fluid passing through the rock. Ratios computed from eq (64) for the model systems range from positive infinity, for infinity thin rock wafers, to values on the order of 0.5 when the rock volume is the entire thermal anomaly. Circulation of reactive fluids through these environments can not be adequately simulated by the numerical equation used for the circulation of inert fluids but requires explicit equations for exchange, reaction, diffusion, and advection of components, as suggested in Norton and Knapp (1977). Simulation of these types of systems will be the topic of a future communication.

CONCLUSIONS

Spatial and temporal variations in fluid flow and heat flux in a sequence of simplified geologic systems indicate that bulk rock permeabilities in host rocks around hot plutons that are $\geqq 10^{-14}$ cm^2 result in convection of thermal energy upward along the sides of the pluton and toward the surface. However, only in those systems that contain permeable plutons is the cooling rate increased. The rather small variation in permeability over which the transition from conductive to convective heat transfer occurs and the relatively low threshold value of permeability required for significant convective heat transfer suggest that heat transfer by circulating fluids may be significant over very broad crustal regions where temperature perturbations occur within the crust. Temperature conditions around plutons that cool by convective heat transfer are substantially different from their conductive dominated equivalents. Large volumes of rock above shallow plutons remain at nearly constant temperature for very long periods of time. The temperature is nominally in the range of 200° to 400°C for the upper crust. This feature and the circulation of large masses of fluid from considerable distances away from the thermal anomaly undoubtedly affect the thermal metamorphism and hydrothermal alteration of rocks in the pluton's vicinity.

Heuristic models of hot pluton environments suggest that fluid circulation is an integral part of their cooling process. Major features of the hydrothermal system noted in these models are undoubtedly evident in their natural analogs. Particularly, the composition and distribution of mineral assemblages shift in both stable and radiometric isotope abundances, and the composition and filling temperatures of fluid inclusions should reflect the style and duration of fluid circulation. However, these data must have been collected with cognizance of the system's flow channels.

Fluids circulate from one rock, temperature, and pressure environment into another along pathlines defined by the fluid potential field and through fracture controlled channels. The fluid flux ranges from 10^{-4} to 10^{-8} gr^{-2} sec^{-1}, and the surface area of minerals exposed along the flow channels is relatively large compared to the amount of fluid in the flow channel. Recalling the porosity model of Norton and Knapp (1977), it is apparent that the circulating bulk fluid may be in direct contact with

only a small portion of the rock in the permeable media, but the mass of fluid to rock ratios is large. As a consequence of the above features, the fluids being redistributed in natural systems will be grossly out of equilibrium with the bulk rock as they flow along the pathlines, although they may have initially been equilibrated with the bulk rock at their initial location. Therefore, if the overall irreversible nature of the reactions between circulating fluids and rocks, the nature of fracture controlled permeability, and the magnitude and direction of fluid flux are accounted for, the geochemical history of pluton environments can be defined.

Hydrothermal alteration phases and stable light isotope distributions have already been interpreted as indicating a style of fluid circulation similar to that indicated by our physical analysis (Helgeson, 1970; Taylor, 1971; and Norton, 1972). Indications that other chemical data may reflect this circulation process are evident. We wish to call attention to the fact that although shifts in chemical composition do indicate fluid redistribution and that in certain instances the direction of fluid flow can be implied, ultimately fluids are shifted into chemical equilibrium with the mineral phases along the flow channel. Subsequently, the fluid and mineral chemistry will not reflect a chemical shift in all or any of the chemical parameters.

Fluid circulation may have played a significant role in regions of the crust where magmatic and volcanic activity is most voluminous, such as along the crustal plate boundaries. The tectonic setting of both convergent and divergent plate boundaries is such that abundant fracturing of host rocks typically accompanies the igneous events. As a result, these environments probably have sufficiently large permeabilities to permit fluid circulation. Fluid circulation, total heat flux, and, consequently, the heat transfer through Earth's crust may be significantly greater than heretofore recognized. One manifestation of this voluminous fluid circulation is the large thicknesses of volcanic rocks that have been hydrothermally altered. Very clearly, our notions of heat flux are in error by perhaps as much as a factor of ten at plate boundaries, since geophysical surveys have probably not measured the convective component.

The divergent plate environment along oceanic ridges is an equally dramatic example of the potential significance of fluid circulation. Consider that the rate of seafloor spreading is proportional to the mass of igneous melt emplaced at the spreading center and further hypothesize that only the upper 2 km of the ridge environment has a permeability greater than 10^{-14} cm^2. Then, by analogy to the models presented above, a mass of fluid equivalent to the entire ocean system has been circulated through the spreading centers, over 2×10^8 yrs, if one assumes an average of 5 cm are added to the crust every year along the strike length of the mid-ocean ridges.

Finally, igneous bodies have interacted with a quantity of fluid nearly equivalent to their mass since permeabilities $\geq 10^{-14}$ cm^2 appear to be reasonable values for many plutons in the shallow crust.

ACKNOWLEDGMENTS

This research was supported by NSF Grants GS-41136 and EAR74-03515 A01 and by matching computer funds from the University of Arizona Computer Center. Additional funds were provided in the early stages by the Universities of Utah and Arizona. The study has benefited from the suggestions and assistance from many of our colleagues, but in particular we are indebted to R. Knapp, R. N. Villas, T. Gerlach, H. Hardee, and D. W. Larson. The study was conceived when H. C. Helgeson pointed out that an early cartoon drawn by the principal author could be quantified, and the study has continually benefited from his critical comments. We are also grateful to H. C. Helgeson and David Kirkham for providing programs to compute equation of state properties in the H_2O-system. We wish to acknowledge the guidance from Lawrence Cathles during the early stages of program development. We wish to thank Lynn McLean for many improvements in the manuscript.

REFERENCES

Bear, Jacob, 1972, Dynamics of fluids in porous media: New York, Am. Elsevier, 764 p.

Bianchi, L., and Snow, D. T., 1969, Permeability of crystalline rocks interpreted from measured orientations and apertures of fractures: Jodphur, Rajasthan, Arid Zone Research Assoc. of India, Annals of Arid Zone, v. 8, no. 2, p. 231-245.

Bénard, M., 1901, Les tourbillons cellulaires dans une nappe liquide transportant de la chaleur par convection en régime permanent: Am. Chim. Phys., v. 23, p. 62-144.

Bruges, E. A., Latto, B., and Ray, A. K., 1966, New correlations and tables of the coefficient of viscosity of water and steam up to 1000 bar and 1000°C: Internat. Jour. Heat and Mass Transfer, v. 9, p. 465-480.

Clark, S. P., Jr., ed., 1966, Handbook of Physical Constants, rev. ed.: New York, Geol. Soc. America Mem. 97, 587 p.

Donaldson, I. G., 1962, Temperature gradients in the upper layers of the earth's crust due to convective water flows: Jour. Geophys. Research, v. 67, no. 9, p. 28-48.

———— 1968, The flow of stream water mixtures through permeable beds: a simple simulation of a natural undisturbed hydrothermal region: New Zealand Jour. Sci., v. 11, no. 1, p. 3-23.

Elder, J. W., 1965, Physical processes in geothermal areas, *in* Lee, W. H. K., ed., Terrestrial Heat Flow: Am. Geophys. Union, Geophys. Mon. Ser. 8, 276 p.

———— 1967, Steady free convection in a porous medium heated from below: Jour. Fluid Mechanics, v. 27, p. 29-84.

Helgeson, H. C., 1970, A chemical and thermodynamic model of ore deposition in hydrothermal systems: Mineralog. Soc. America Spec. Paper 3, p. 155-186.

Helgeson, H. C., and Kirkham, D. H., 1974a, Theoretical predictions of the thermodynamic behavior of aqueous electrolytes at high pressures and temperatures; I: Summary of the thermodynamic/electrostatic properties of the solvent: Am. Jour. Sci., v. 274, p. 1089-1198.

———— 1974b, Theoretical predictions of the thermodynamic behavior of aqueous electrolytes at high pressures and temperatures; II: Debye-Huckel parameters for activity coefficient and relative partial molal properties of the source: Am. Jour. Sci., v. 274, p. 1199-1261.

Holst, P. H., and Aziz, K., 1972, Transient three-dimensional natural convection in confined porous media: Internat. Jour. Heat and Mass Transformation, v. 15, p. 73-90.

Jaeger, J. C., 1968, Cooling and solidification of igneous rocks, *in* Hess, H., ed., Basalts, v. II: New York, John Wiley & Sons, Inc., p. 504-535.

Keenan, J. H., and Keyes, F. G., 1969, Steam Tables: New York, John Wiley & Sons, 162 p.
Lindgren, W., 1907, The relation of ore deposition to physical conditions: Econ. Geology, v. 2, p. 105-127.
Lister, C. R. B., 1974, On the penetration of water in hot rock: Astron. Soc. Jour. Geophys. Research, v. 39, p. 465-509.
Lovering, T. S., 1935, Theory of heat conduction applied to geological problems: Geol. Soc. America Bull., v. 46, p. 69-94.
Nield, D. A., 1968, Onset of thermohaline convection in a porous medium: Water Resources Research, v. 4, p. 553-560.
Norton, D., 1972, Concepts relating anhydrite deposition to solution flow in hydrothermal systems: Internat. Geol. Cong., 24th, Montreal 1972, sec. 10, p. 237-244.
Norton, D., and Knapp, 1977, Transport phenomena in hydrothermal systems: The nature of rock porosity: Am. Jour. Sci., v. 277, p. 913-936.
Peaceman, D. W., and Rachford, H. H., Jr., 1955, The numerical solution of parabolic and elliptic differential equations: Soc. Indust. Appl. Math. Jour., v. 3, no. 1, p. 28-41.
Rayleigh, Lord, 1916, On convection currents in a horizontal layer of fluid, when the higher temperature is on the underside: Philos. Mag., ser. 6, v. 32, p. 529-545.
Ribando, R. J., Torrance, K. B., and Turcotte, D. L., 1976, Numerical models for hydrothermal circulation in the oceanic crust: Jour. Geophys. Research, v. 81, p. 3007-3012.
Roache, Patrick J., 1972, Computational Fluid Dynamics: Albuquerque, N.M., Hermosa Publishers, 434 p.
Rubin, H., 1973, Effect of nonlinear stabilizing salinity profiles on thermal convection in a porous medium layer: Water Resources Research, v. 9, p. 211-221.
Schmidt, E., 1969, Properties of Water and Steam in SI-Units: New York, Springer-Verlag, 205 p.
Ssu-hsiao, C., 1250, *in* Brower, ed., Of All Things Most Yielding: San Francisco, California, McGraw Hill, Friends of the Earth, 128 p.
Taylor, H. P., Jr., 1971, Oxygen isotope evidence for large-scale interaction between meteoric ground waters and Tertiary granodiorite intrusions, Western Cascade Range, Oregon: Jour. Geophys. Research, v. 76, p. 7755-7873.
Van Hise, C. R., 1901, Some principles controlling the deposition of ores: Am. Inst. Min. Eng. Trans., v. 30, p. 27.
Veronis, G., 1968, Effect of stabilizing gradient of solute on thermal convection. Jour. Fluid Mech., v. 34, p. 315-336.
Villas, N. R., ms, 1975, Fracture analysis, hydrodynamic properties, and mineral abundance in altered igneous rocks at the Mayflower Mine, Park City District, Utah: Ph.D. dissert., University of Utah, Salt Lake City, 253 p.
Wooding, R. A., 1957, Steady state free thermal convection of liquid in a saturated permeable medium: Jour. Fluid Mech., v. 2, p. 273-285.

[AMERICAN JOURNAL OF SCIENCE, VOL. 277, OCTOBER, 1977, P. 913-936]

American Journal of Science

OCTOBER 1977

TRANSPORT PHENOMENA IN HYDROTHERMAL SYSTEMS: THE NATURE OF POROSITY

D. NORTON and R. KNAPP

Department of Geosciences,
University of Arizona, Tucson, Arizona 85721

ABSTRACT. Porosity of rocks may be described by $\phi_{Total} = \phi_{Flow} + \phi_{Diffusion} + \phi_{Residual}$. Laboratory experiments indicate that total porosities of fractured rocks in hydrothermal systems range from 0.2 to 0.01, and diffusion porosities range from 10^{-3} to 10^{-6}. Synthesis of data from the literature and field observations of fracture characteristics indicate that flow porosities range from 10^{-3} to 10^{-6}. Therefore, the major portion of total porosity in pluton environments is due to residual pores not interconnected to either flow or diffusion porosity.

Permeability may be defined as a function of the abundance and geometry of continuous flow channels. Our observations suggest that a planar fracture model is a reasonable first order approximation for fractures in pluton environments. An analysis of aperture, abundance, and continuity indicates permeabilities on the order of 10^{-14} cm^2 may characterize large regions of the crust.

The proposed porosity model affords for the definition of the interface between circulating hydrothermal fluids and reactant minerals in a manner consistent with the physical phenomena and with the partial differential equations that describe advection-diffusion-reaction processes.

NOTATION

A — area (cm^2)
A_i — volumetric source of i^{th} component
b — half the fracture aperture (cm)
B — coordinate of fracture aperture (cm)
d — fracture aperture (cm)
D_{ik} — diffusion coefficient of the i^{th} ion due to a concentration gradient of the k^{th} ion (kgH_2O cm^{-1} sec^{-1})
f — fracture frequency (cm fracture^{-1})
F_D — fluid driving force (g cm sec^{-2})
F_r — fluid resistive force (g cm sec^{-2})
k — permeability (cm^2)
l — unit length (cm)
m_i — molality of the i^{th} component (moles kgH_2O^{-1})
M_i — moles of the i^{th} component
n — fracture abundance (fractures cm^{-1})
Q — volumetric flow rate (cm^3 sec^{-1})
S — surface area (cm^2)
$\bar{S}_i$ — summation of component fluxes for the i^{th} ion (mols cm^{-2} sec^{-1})
t — time (sec)
$\bar{u}_i$ — flux of the i^{th} component (moles cm^{-2} sec^{-1})

$\bar{v}$ — fluid velocity (cm sec^{-1})
V — representative elemental volume (cm^3)
δ_c — width of concentration boundary layer (cm)
δ_o — width of laminar flow profile (cm)
η — viscosity (g cm^{-1} sec^{-1})
ν — viscosity (cm^2 sec^{-1})
ρ — fluid density (g cm^{-3})
ρ_β — bulk density (g cm^{-3})
ρ_γ — grain density (g cm^{-3})
σ — shear stress (g cm^{-1} sec^{-2})
τ — tortuosity of pores
ϕ_D — total diffusion porosity
ϕ_F — flow porosity
ϕ_R — residual porosity
ϕ_T — total porosity
ϕ'_D — equal to the directional diffusion porosity divided by τ
$\bar{\phi}$ — equal to ϕ'_D/ϕ_D
Ω — fluid potential (g cm^{-1} sec^{-2})
∇ — operator, $\frac{\partial}{\partial x} + \frac{\partial}{\partial y} + \frac{\partial}{\partial z}$ (cm^{-1})

INTRODUCTION

The interface between circulating aqueous solutions and reactant mineral phases is defined by the relative distribution of solution filled pores and minerals. This interface is a controlling factor in the chemical mass transfer that typically occurs between minerals and solutions in geochemical systems. Conceptual models that have been developed for the sedimentary rock environment (Fatt, 1956) neither adequately describe low total porosity and systematically developed fractures characteristic of igneous rocks nor do they account for the distribution of alteration minerals found in hydrothermal systems. Alteration minerals in hydrothermal systems occur both along and adjacent to continuous fractures. The compositions and assemblages of these minerals do not change over distances of meters to hundreds of meters parallel to the fractures, whereas abrupt changes occur normal to the fracture plane over distances of only millimeters to tens of centimeters. In rocks where the fracture sets are sufficiently close-spaced, the alteration zones may overlap, thereby producing a continuous zone of alteration products normal to the adjacent fractures. These aspects of mineral distributions suggest that the two principal modes of aqueous ion transport are by fluid flow along fractures and by aqueous diffusion away from the fractures.

The reaction between circulating fluids and their host rocks and the diffusion of aqueous ions to and away from flow channels may be described in terms of partial differential equations. Since the distribution of alteration mineral products predicted by the numerical solution to

these equations depends directly on the nature of porosity, the following porosity model was developed.

Porosity model.—The total porosity in fractured media, ϕ_T, may be represented by

$$\phi_T = \phi_F + \phi_D + \phi_R; \quad (1)$$

ϕ_F is the effective flow porosity and represents those pores through which the dominant mode of fluid and aqueous species transport is by fluid flow; ϕ_D is the diffusion porosity and represents those pores through which the dominant mode of transport is by diffusion through the aqueous phase (Garrels, Dreyer, and Howland, 1949); ϕ_R is the residual porosity and represents those pores not connected to ϕ_F or ϕ_D. The geometry and distribution of these pore types is apparent in many outcrops (pl. 1) where one can readily observe continuous fracture sets, ϕ_F, and less continuous sets, ϕ_D. These field observations, together with laboratory measurements that define total diffusion and residual porosity, suggest the porosity distribution in these types of outcrops can be schematically represented by figure 1.

TOTAL POROSITY

The total porosity of a rock is defined by

$$\phi_T = 1 - \frac{\rho_\beta}{\rho_\gamma} \quad (2)$$

where ρ_β is the dry rock bulk density of a representative sample determined by standard immersion techniques, and ρ_γ is the grain density, determined on a finely ground sample with a grain size less than the minimum pore diameter. The porosity determined in this manner is a measure of the total pore volume in rock, if the sample represents all porosity types. Partial or total saturation of the pores with fluid would introduce errors on the order of 2 percent of the total porosity for rocks in the ≤ 0.05 porosity range.

FLOW POROSITY

The flow porosity of fractured rocks is that portion of the total rock that constitutes rock permeability. Continuous pore features in pluton environments include planar features such as faults, joints, cracks, or bedding planes in layered host rocks. A simple flow porosity model based on open-smooth-walled fractures appears to be a reasonable first approximation of permeability.

Fluid flow in natural systems is characterized by laminar flow (fig. 2), which is the basis for development of equations that relate fracture characteristics to rock permeability. Following the formulations of De-Weist (1969), Snow (ms, 1970), and Maini (ms), a representative elemental volume, V, is chosen such that it contains a single fracture parallel to the x-y coordinate axis. A functional expression is derived for one-dimensional fluid velocity at any point in the fracture cross section from

PLATE I

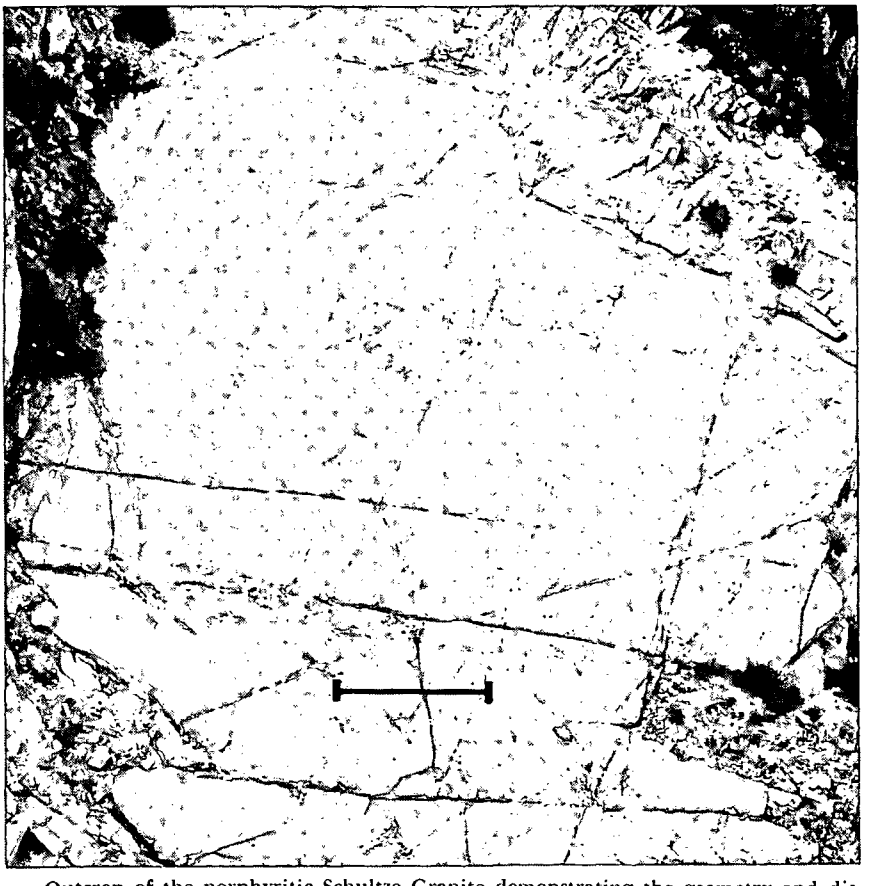

Outcrop of the porphyritic Schultze Granite demonstrating the geometry and distribution of flow and diffusion porosity. Continuous fractures, which cross cut outcrop, represent flow channels, and discontinuous fractures represent diffusion porosity. Scale bar is 5 m.

the differential equation describing the flow. This function is then used to find the mass flow along the fracture by integrating the velocity function over the fracture opening.

Steady state flow conditions require equality between the fluid driving force, F_d, and the resistive viscous force, F_r. The driving force is determined by the gradient in fluid potential and the area on which the force acts:

$$F_d = lA\nabla\Omega. \tag{3}$$

The resistive force is due to shear stress acting on the surface area, S, of the fracture walls:

$$F_r = \sigma S. \tag{4}$$

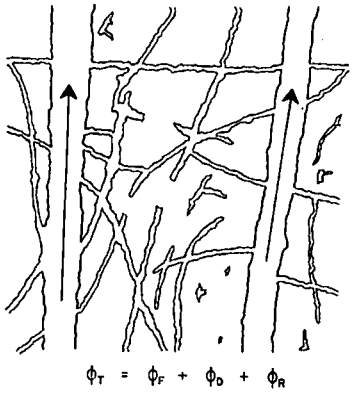

Fig. 1

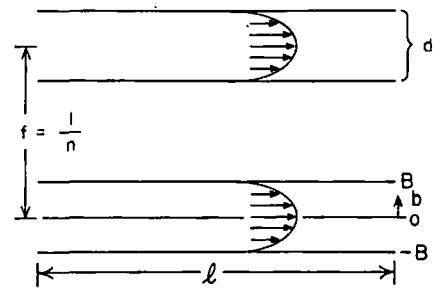

Fig. 2

Fig. 1. Schematic representation of constituent porosities showing the geometric relationships between residual pores, ϕ_R, diffusion pores, ϕ_D, and flow pores, ϕ_F. The arrows denote an arbitrarily chosen direction of fluid flow in ϕ_F. The pores extending from these two flow channels either have apertures that are too small to permit significant fluid flow or are discontinuous; therefore, all these pores are ϕ_D. The relative abundances are not shown.

Fig. 2. The laminar flow profile in planar fractures due to viscous drag forces at the walls. f is the fracture spacing and d the aperture. B and $-B$ represent the limits of integration in eq (9).

where $S = 2l$, and l is the unit length of the representative elemental volume. The shear stress in a viscous fluid is related to the fluid velocity by:

$$\sigma = -\eta \frac{d\bar{v}}{db}, \tag{5}$$

where $b = \frac{1}{2}$ fracture aperture (cm). The area on which the fluid driving force acts is orthogonal to the direction of flow in the fracture:

$$A = 2b \tag{6}$$

Combining eqs (3-6), we have a differential equation in terms of fluid velocity and distance from the fracture wall:

$$d\bar{v} = -b \frac{\nabla\Omega}{\eta} db. \tag{7}$$

Integrating eq (7) and evaluating the integration constant by using $\bar{v} = 0$ when $b = B$ gives the velocity profile across the aperture of a single fracture:

$$\bar{v} = \frac{\nabla\Omega}{2\eta}(B^2 - b^2). \tag{8}$$

This parabolic flow profile develops in less than 1 m along the fracture for fluid velocities less than 10 cm/sec, and we will, therefore, assume in subsequent discussions that this flow profile is fully developed in geologic systems.

The volumetric flow rate from a single fracture is defined by first considering the flow velocity through an incremental cross-sectional area of the fracture and then integrating this expression over the fracture opening orthogonal to the flow direction (fig. 2).

$$Q = \int_{-B}^{B} \frac{l\nabla\Omega}{2\eta} (B^2 - b^2)\, db. \tag{9}$$

Integrating eq (9) gives the flow rate,

$$Q = \frac{-2B^3\nabla\Omega}{3\eta} \tag{10}$$

per unit length, l, of a single fracture. Substituting the aperture of the fracture into (10) gives the volume flow rate from n such parallel fractures

$$Q = \frac{-nd^3\nabla\Omega}{12\eta}. \tag{11}$$

The general statement of Darcy's Law for flow through porous media is (Hubbert, 1940):

$$Q = \frac{-k\nabla\Omega}{\eta}, \tag{12}$$

and k is a factor describing the shape and length characteristics of the flow passages. By analogy of (12) to (11) we see this intrinsic rock parameter, permeability, for fracture controlled flow is:

$$k = \frac{nd^3}{12}. \tag{13}$$

Fracture sets in natural systems are not precisely represented by this model; however, anisotropic characteristics of the fractures may be formulated into a tensor form:

$$Q = -\frac{k_{ij}}{\eta}\nabla\Omega, \tag{14}$$

where k_{ij} is the permeability tensor in which the subscript i relates to the fluid flow direction, and j relates to the potential gradient direction.

The porosity of the flow channels is also related to the fracture aperture and abundance, where

$$\phi_F = nd \tag{15}$$

for a single parallel fracture set.

Field observations of abundance and aperture on parallel fracture sets, together with eq (13), permit permeability estimates to be made. Abundances of fractures in plutons vary from 0.5 fracture/cm in some ore deposits (Bingham, Utah) to 10^{-3} fractures/cm in unaltered igneous bodies (Villas, ms; Bianchi and Snow, 1969). Aperture variations, which

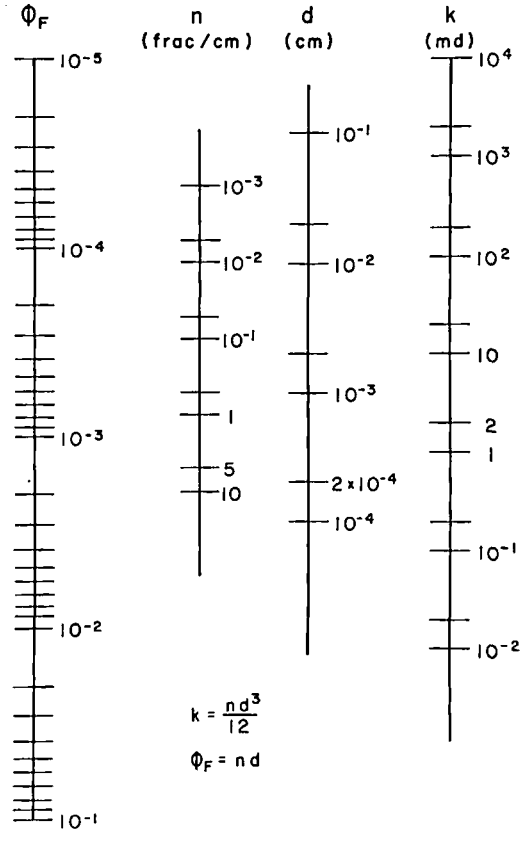

Fig. 3. Graphical solution to eqs (13) and (15). Aperture estimates, d, range from 5×10^{-5} to 2×10^{-2} cm, whereas fracture abundances, n, range from 5×10^{-1} to 10^{-3}/cm. With $d = 10^{-4}$ cm and $n = 5 \times 10^{-1}$/cm, $\phi_F = 5 \times 10^{-5}$ and $k = 4 \times 10^{-8}$ md where 10^{-11} cm^2 = 1 millidarcy.

have the greatest effect on permeability but are the least well known, may range from 5×10^{-5} to 2×10^{-2} cm. Though these ranges in apertures and abundances are large, they place some interesting constraints on the magnitude of flow porosity when examined with respect to a single fracture set, compare eqs 13 and 15 and their graphical solution (fig. 3). The maximum range in flow porosity is from 10^{-2} to 5×10^{-8}. Values estimated by Villas (ms) on the Mayflower Pluton range from 2×10^{-3} to 3×10^{-5}. The comparable total porosities for the Mayflower diorite are in the range of 0.01 to 0.03. Similarly, the flow porosity and the total porosity of the Sherman Granite are 5×10^{-6} and 10^{-2}, respectively (Pratt and others, 1974). We, therefore, conclude that the flow porosities are generally a small fraction of the total porosities, even though precise limits can not be established.

Measurements of permeability by different methods often yield significantly different values. In general, in-situ measurements of permea-

bility on large representative blocks of fractured rock indicate values in the range of 10^{-12} to 10^{-8} cm^2 (table 1). An in-situ experiment conducted on the Sherman Granite determined the permeability of this rock to be 10^{-11} cm^2, whereas the permeability determined on intact core samples is about 2 to 3 orders of magnitude lower. Laboratory measurements of intact core samples of limestones, dolomites, and granites (table 1) also indicate very low values of permeability. Clearly, the permeability of rocks in hydrothermal systems is a poorly known quantity.

Estimates of rock permeabilities in the Earth's crust rely on deep drill holes, 10 km in sedimentary basins and 4 to 5 km in crystalline rocks, abundance and aperture of continuous fractures, electrical resistivity profiles, elastic properties of intact rock samples, and seismic data. These various lines of indirect evidence suggest that permeabilities to depths of 10 to 15 km may be significantly greater than 10^{-14} cm^2. Whereas laboratory measurements indicate that a pressure increase from 1 bar to 1 kb produces a $10^{1.5}$ decrease in permeability (Brace, Walsh, and Frangos, 1968), seismic hypocentral data suggest that brittle rock failure and transient fractures occur at depths to at least 15 to 20 km. The persistence of continuous fractures filled with conductive pore fluids at considerable depths is further indicated by relatively high electrical conductivities in the middle to upper crust (Plauff, 1966; Jackson, 1966; Keller, Anderson, and Pritchard, 1966; and Brace, 1971).

The permeability of fractured crystalline rocks is due to continuous fractures, and, even though the rock mass between these channels has a

TABLE 1

Some permeability measurements on crystalline rocks

Rock type	k(cm^2)	ϕ_F	Method	Reference
Hardhat-granite	10^{-9}-10^{-13}		pump	Boardman and Skrove, 1966
Sherman-granite	10^{-11}	2×10^{-6}	pump	Pratt and others, 1974
Sherman-granite	$< 10^{-14}$		core	Pratt and others, 1974
Quartz porphyry	$\sim 10^{-11}$		pump	Cadek and others, 1968
Gneiss-schist	5×10^{-11}		pump test in fractured zone	Marine, 1966
Gneiss-schist	5×10^{-14}		pump (without fractures)	Marine, 1966
Gneiss-schist	10^{-15}		core	Marine, 1966
Metabasalt	2×10^{-9}		pump	Davis, 1969
Schist	1.4×10^{-8}		pump	Davis, 1969
Quartz diorite	10^{-7} to 3×10^{-10}	2×10^{-3} to 3×10^{-5}	planar fracture model	Villas, ms.
Granite	10^{-4} to 10^{-10}	5×10^{-2} to 4×10^{-5}	planar fracture model	Bianchi and Snow, 1969
Welded tuff	$< 2\times10^{-16}$		pump	Winograd, 1971
Bedded tuff	10^{-10}-10^{-12}		pump	Winograd, 1971
Granite	10^{-14}-10^{-17}		core*	Brace, Walsh, and Frangos, 1968
Limestone	2×10^{-15}		disk	Ohle, 1951
Dolomite	10^{-10}		disk	Ohle, 1951
Volcanic (clastics)	10^{-8}-6×10^{-12}		drawn down	Grindley, 1965

* Measured as a function of effective pressure

relatively high total porosity, its effective permeability is nil. This fact is also evidenced by the above observations and the distribution of hydrothermal alteration minerals along the walls of fractures. The fact that alteration minerals occur in veins in ore deposits and active geothermal systems clearly demonstrates the nature of fracture controlled fluid flow. The widespread chemical alteration of rocks in hydrothermal systems further attests to the relatively large permeability of rocks in the Earth's crust.

The importance of deducing broad scale permeabilities of the crust relates directly to studies of the mass movement of aqueous solutions in the crust. Permeabilities greater than 10^{-14} cm^2 are conducive to the circulation of fluids in pluton environments and perhaps over broader regions of the crust (Norton and Knight, 1977). Also, since flow porosity in fractured igneous rocks, and possibly in fractured rocks in general, is apparently a small fraction of the total rock porosity, 10^{-1} to 10^{-5}, the true velocity of particles within a flow fracture, eq (8), will be orders of magnitude greater than the superficial velocity.

$$\bar{v}_{true} = \frac{\bar{v}_{Darcy}}{\phi_F} \tag{16}$$

DIFFUSION POROSITY

The nature of diffusion porosity is apparent, if we consider a typical region, R, within which the transport of aqueous components by fluid flow is insignificant with respect to diffusional transport. These conditions may occur in regions characterized by discontinuous fractures, small aperture fractures, or discontinuous pores. This type of region is typically bounded by continuous sets of fractures which constitute the flow channels in the overall system (fig. 1).

The diffusional flux of the i^{th} ion from the region is defined by the flux vector normal to an incremental area of the region's surface, S,

$$\bar{u}_i = -\phi'_D \sum_k D_{ik} \nabla m_k \tag{17}$$

where ϕ'_D is the ratio of the diffusion porosity coincident with the normal flux vector to the tortuosity, τ, of the pores, m_k is the concentration of the k^{th} ion in molality, and D_{ik} is the diffusion coefficient of the i^{th} ion due to the gradient in concentration of the k^{th} ion. The amount of the i^{th} ion leaving the region, with respect to the volume, is given by the volume integral of the divergence of $\bar{u}_i$,

$$\frac{\partial M_i}{\partial t} = \int_R \text{div } \bar{u}_i dV, \tag{18}$$

whereas the change in the amount of the i^{th} aqueous ion contained within the region as a function of time, is given by,

$$\frac{\partial M_i}{\partial t} = \int_R \rho \phi_D (1 + A_i) \frac{\partial m_i}{\partial t} dV, \tag{19}$$

where ϕ_D is the total diffusion porosity, and A_i is a volumetric source or sink of the i^{th} ion which, in effect, describes the irreversible mass transfer between the aqueous and solid phases. The amount leaving and amount depleted must be equal; therefore, eqs (18) and (19) are equal. Since the integrals hold for any subregion in R, the integrals can be eliminated. Eqs (18) and (19) are combined to describe the conservation of the i^{th} aqueous species in R:

$$\rho\phi_D (1 + A_i) \frac{\partial m_i}{\partial t} = \nabla \cdot \phi'_D \sum_k D_{ik} \nabla m_k. \tag{20}$$

The magnitude and distribution of the directional diffusion porosity, ϕ'_D, as defined by eq (17), have been measured on a variety of rocks. The total diffusion porosity is determined by experiments where $A_i = 0$ and $k = 1$ and are calculated by rearranging (20).

$$\frac{\partial m_i}{\partial t} = \rho D_i \bar{\phi} \nabla^2 m_i, \tag{21}$$

where

$$\bar{\phi} = \frac{\phi'_D}{\phi_D} \tag{22}$$

Eq (21) is then solved numerically to yield $\bar{\phi}$, which substituted in eq (22) gives ϕ_D.

Experimental apparatus modified from Garrels, Dreyer, and Howland (1949) was used to obtain the diffusion porosity data (Knapp, ms). Rock wafers, 1.0 to 2.5 cm in radius and from about 0.2 to 1.0 cm thick, are embedded with epoxy in Plexiglas plugs, so that only the circular surfaces are exposed. The samples are then saturated by drawing 10^{-4} N KCl solution through the wafer for at least 24 hrs. Microscopic examination of the wafers serves to check the epoxy seal for leakage and the rock for any induced fractures.

The plug with the saturated rock is next placed in a Plexiglas diffusion cell; the cell is filled with a measured amount (usually 60 ml) of 10^{-4} N KCl solution, and electrodes are inserted into the cell. The entire assemblage is placed in a thermally insulated, 25°C, tank containing about 10 l of 1 N KCl solution, which sets up an activity gradient across the rock wafer. Care is taken to minimize any fluid potential gradient between the cell and the tank to a negligible value. The concentration change is monitored by conductometric methods.

The experimental error in these measurements is difficult to define precisely. But, based on ϕ'_D measured on adjacent samples of apparently homogeneous and isotropic rocks, the precision is between 4 and 30 percent (Knapp, ms). Though this upper limit is fairly large, it does not seriously affect the conclusions derived from the experimental data.

The results of experiments indicate that the diffusion porosity is on the order of 10^{-3} to 10^{-4} (fig. 4). Furthermore, the diffusion porosity is

a very small fraction of the total rock porosity, since $\phi'_D \approx 0.04\ \phi_T$ (fig. 5). Total rock porosities in the samples studied amount to 10^{-2} to 2×10^{-1} (fig. 6).

Of all the rocks examined during this study (tables 2 and 3), the volcanic rocks have the largest total porosities, from 0.2 to 2×10^{-1}, and ϕ'_D values, from 10^{-2} to 10^{-3} (figs. 4 and 6). Carbonate rocks studied have a fairly narrow range of total porosity values, from about 5×10^{-2} to less than 10^{-2}, whereas the ϕ'_D values range from 10^{-3} to 10^{-4}. The

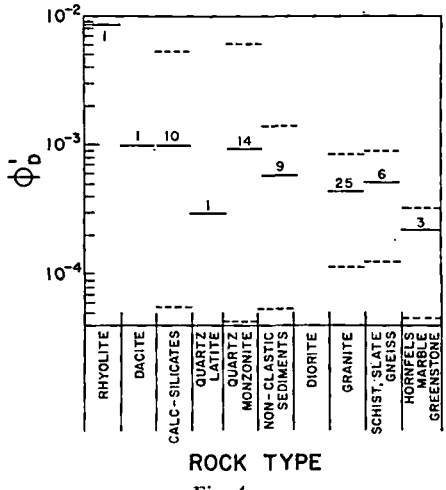

Fig. 4

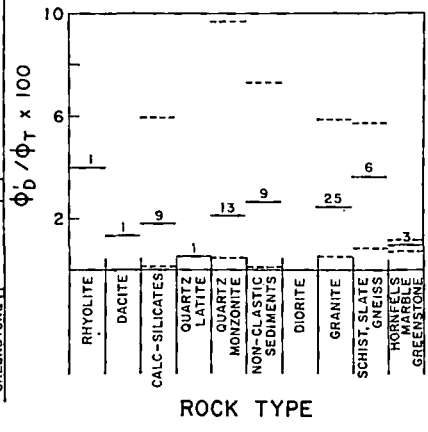

Fig. 5

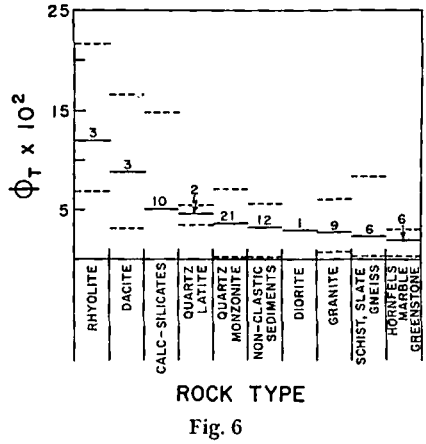

Fig. 6

Fig. 4. Mean values, solid lines, and range of values, dashed lines, of ϕ'_D for the various rock types examined in this study. The numerals denote the number of determinations for each rock type.

Fig. 5. The percentage of the total porosity that is composed of ϕ'_D. The solid lines are mean values, and the dashed lines are the range in values. The numerals denote the number of determinations for each rock type.

Fig. 6. Total porosity values for the various rock types studied. The solid lines are mean values, and the dashed lines the range in values. The numerals denote the number of determinations for each rock type.

TABLE 2

Density and porosity data

Sample no.	Bulk density ρ_B (g/cm^3)	Grain density ρ_γ (g/cm^3)	Total porosity $\phi_T \times 10^2$	$\phi'_D \times 10^4$	Sample thickness (cm)
Johnson Camp, Ariz.					
BQZ-5	2.61	2.72	4.11	8.1*	1.04
				13.7**	1.04
AL-007	2.68	2.74	2.12	5.5**	0.424
				1.5*	0.988
LA5	2.55	3.00	14.7	10.	0.90
AM-005	2.71	2.79	2.72	14.**	0.843
				2.*	0.800
AU-004	2.62	2.68	2.53		
ML-002	2.78	2.85	2.35		
MM-6	2.55	2.65	3.88		
MU-001	2.55	2.69	5.35		
ESC-3	2.64	2.71	2.62		
BP-4	2.60	2.70	3.85		
PS-1-JC	2.69	2.73	1.54	8.86**	0.925
				4.92*	0.964
Globe-Miami, Ariz.					
PS-1-GM	2.74	2.78	1.30		
Ronda, Spain					
R-71	2.74	2.76	.73	2.4*	0.386
R-80	2.77	2.80	1.07	3.3*	1.224
R-81	2.85	2.89	1.38	59.	1.29
R-125	2.72	2.97	8.42	7.1**	0.673
R-217	2.69	2.77	2.89	3.2	0.880
R-245	3.01	3.03	.660	3.7**	0.831
R-278	2.66	2.73	2.56	2.9	1.14
Chino, N.M.					
CS-1	2.69	2.97	9.43	7.5	1.05
CS-2	2.79	3.01	7.31	3.5	0.942
CS-4	2.75	2.83	2.83		
CS-5	4.25	4.67	8.99	53.	0.881
CS-6	3.01	3.12	3.53	9.7	1.33
CS-7	2.73	2.75	.73		
CS-8	3.18	3.24	1.85	7.0	1.19
CS-9	2.73	2.80	2.50	2.6	1.25
CS-10	2.72	2.73	.366	2.9	0.820
CS-11	2.64	2.71	2.58	4.1	1.02
CS-12	2.62	2.74	4.38	0.53	0.742
CS-13	2.49	2.67	6.74		
Chino pluton	2.62	2.69	2.60	10.	0.839
Silver City, N.M.					
Chino pc	2.97	2.99	.669	0.45	0.979
Cont. pit	2.91	3.03	3.96	0.54	0.949
150 pit	3.62	3.82	5.24	2.0	1.04
Copper Flat Pluton	2.48	2.62	5.34	2.9	0.857
San Manuel, Ariz.					
SM-1	2.71	2.75	1.46	1.1	1.04
SM-2	2.70	2.75	1.82	2.1	0.968
SM-3	2.71	2.87	5.58	4.1	1.02
SM-5	2.63	2.70	2.59	0.42	0.881
SM-7	2.45	2.63	6.84	11.	0.999
SM-8	2.57	2.70	4.82	8.8	0.958
SM-9	2.58	2.73	5.50	5.8	1.05

TABLE 2 (continued)

Sample no.	Bulk density ρ_B (g/cm^3)	Grain density ρ_γ (g/cm^3)	Total porosity $\phi_T \times 10^2$	$\phi'_D \times 10^4$	Sample thickness (cm)
Butte, Mont.					
8	2.73	2.91	6.35	61.	1.03
9A	3.04	3.22	5.41		
10282-2	2.60	2.71	3.77	8.4	1.18
10282-1	2.65	2.66	.0753	8.0	1.52
1024-1	2.74	2.77	1.55		
10283-1	2.73	2.76	1.01	2.4	1.12
Sierrita-Esperanza, Ariz.					
E-1	2.53	2.60	2.96		
E-2	2.66	2.71	1.96		
E-5	2.44	2.63	7.48		
ST-1	2.57	2.64	2.50		
ST-3	2.79	2.86	2.90		
ST-6	2.64	2.70	2.63	3.4	0.807
				1.1	1.27
Schultze Pluton, Globe-Miami, Ariz.					
S1 BB	2.51	2.65	5.35	3.9	0.840
SPV	2.61	2.66	1.77	4.8	1.0
				2.2	1.0
				8.3	0.507
SD5				16.0	0.144
				6.8	0.222
				6.1	0.280
5CM				5.2	0.481
3A				5.4	0.643
7CM				5.1	0.708
2				2.1	0.911
3				6.4	0.987
4				4.6	1.107
Bingham, Utah					
BGP	2.46	2.62	6.11	3.0	1.19
BQLP	2.58	2.65	2.64		
BWR	2.44	2.79	12.5	3.2	1.17
Miscellaneous					
SG-1	2.52	2.62	4.12		
LG-1	2.65	2.68	1.08	3.1	1.0
				2.0	1.0
RM-1	2.16	2.75	21.5	86.	0.888
TC-1	2.56	2.64	2.96		
AG-1	2.60	2.62	.611		
TR-3	2.62	2.65	1.36		
TR-5	2.46	2.66	7.52	9.9	1.09
TR-6	1.68	2.76	3.08		
DAC	2.20	2.61	15.7		

* Oriented perpendicular to foliation or bedding.
** Oriented parallel to foliation or bedding.

TABLE 3

Mineralogy of samples

Sample no.	Rock name	Mineralogy
Johnson Camp, Ariz.		
BQZ-5	Bolsa quartzite	quartz
AL-007	Lower Abrigo shale	clay, calcite
LA5	Lower Abrigo skarn	tremolite, muscovite, quartz, magnetite, hematite
AM-005	Middle Abrigo limestone	calcite, chert
AU-004	Upper Abrigo quartzite	quartz
AU-006	Upper Abrigo limestone	calcite, chert
ML-002	Lower Martin limestone	calcite
MM-6	Middle Martin limestone	calcite
MU-001	Upper Martin quartzite	quartz
ESC-3	Escabrosa marble	calcite
BP-4	Black Prince limestone	calcite
PS-1-JC	Pinal Schist	
Globe-Miami, Ariz.		
PS-1-GM	Pinal Schist	
Ronda, Spain		
R-71	slate	
R-80	biotite-garnet metapelite	andalusite, quartz, sericite, biotite, magnetite
R-81	quartzite	quartz, diopside, biotite, sphene, plagioclase, chlorite
R-125	pelitic schist	muscovite, tourmaline, andalusite, staurolite, quartz, biotite, garnet, plagioclase
R-217	hornfels	quartz, biotite, plagioclase, perthite, cordierite
R-245	granulite-grade gneiss	quartz, garnet, microperthite, plagioclase, sillimanite, biotite
R-278	hornfels	quartz, perthite, cordierite, plagioclase, biotite, sillimanite
Chino, N. Mex.		
CS-1	skarn	quartz, magnetite, pyrite, chalcopyrite
CS-2	skarn	quartz, sericite(?), biotite, magnetite, chlorite, pyrite, chalcopyrite
CS-3	skarn	quartz, andradite, magnetite, calcite, pyrite, chalcopyrite
CS-4	skarn	quartz, tremolite, magnetite, pyrite
CS-5	skarn	magnetite, quartz, pyrite, calcite
CS-6	skarn	amorphous silica, hematite, magnetite, calcite
CS-8	skarn	diopside, quartz, amorphous silica(?), calcite, magnetite
CS-9	skarn	quartz, calcite, diopside(?)
CS-10	Syrena limestone	calcite
CS-11	Upper Oswaldo limestone	calcite, quartz
CS-12	Lower Syrena limestone	calcite, quartz
CS-13	rhyolite subvolcanic	
Chino pluton	altered quartz monzonite porphyry	
Silver City, N. Mex.		
Chino pc	greenstone	
Cont. pit	skarn	quartz, andradite, magnetite, talc, sericite(?), pyrite, chalcopyrite, calcite
150 pit	skarn	andradite, quartz
Copper Flat pluton	quartz latite porphyry	

TABLE 3 (continued)

Sample no.	Rock name	Mineralogy
San Manuel, Ariz.		
SM-1	porphyritic Oracle quartz monzonite, altered	quartz, microcline, chlorite, biotite, plagioclase, hornblende, montmorillonite, epidote, hematite
SM-2	porphyritic Oracle quartz monzonite, altered	quartz, K-feldspar, plagioclase, chlorite, biotite, kaolinite, montmorillonite
SM-3	porphyritic Oracle quartz monzonite, altered	quartz, K-feldspar, sericite, kaolinite, biotite, plagioclase, pyrite, chlacopyrite, hematite
SM-5	porphyritic Oracle quartz monzonite, altered	quartz, K-feldspar, chlorite, plagioclase, sericite, pyrite, hematite, epidote
SM-7	quartz monzonite porphyry, altered	quartz, K-feldspar, plagioclase, chlorite, biotite, sericite, pyrite
SM-8	quartz monzonite porphyry, altered	quartz, sericite, chlorite, K-feldspar
SM-9	porphyritic Oracle quartz monzonite, altered	quartz, sericite, clay, plagioclase, microcline
Butte, Mont.		
8	sericitized Butte quartz monzonite	
9A	sericitized Butte quartz monzonite	with pyrite, chalcocite, enargite in vein
10282-2	argillized (white) Butte quartz monzonite	
10282-1	argillized (green) Butte quartz monzonite	quartz, potassium feldspar, plagioclase, biotite, hornblende, anhydrite
1024-1	altered Butte quartz monzonite	
10283-1	fresh Butte quartz monzonite	
Sierrita-Esperanza, Ariz.		
E-1	altered Esperanza quartz monzonite porphyry	quartz, plagioclase, K-feldspar, biotite, sericite, rutile, molybdenite, chalcopyrite
E-2	altered Esperanza quartz monzonite porphyry	quartz, plagioclase, K-feldspar, biotite, montmorillonite, pyrite, chalcopyrite, molybdenite
E-5	altered rhyolite	with quartz, hematite, sericite, pyrite
ST-1	altered quartz monzonite porphyry	quartz, K-feldspar, kaolinite, biotite, pyrite, chalcopyrite
ST-3	altered biotite quartz diorite	plagioclase, biotite, montmorillonite(?), chlorite, sericite, epidote, quartz
ST-6	altered Harris Ranch quartz monzonite	quartz, plagioclase, K-feldspar, hornblende, kaolinite, chlorite, biotite, calcite, pyrite, hematite
Schultze Pluton, Globe-Miami, Ariz.		
S1 BB	altered porphyritic Schultze Granite	quartz, K-feldspar, plagioclase, biotite, clays, muscovite, calcite, Cu oxides
SPV	equigranular Schultze Granite	quartz, K-feldspar, plagioclase, biotite, kaolinite, muscovite, clays

TABLE 3 (continued)

Sample no.	Rock name	Mineralogy
Porphyritic Schultze Granite, Globe-Miami, Ariz.		
SD5	porphyritic granite	
SD5	porphyritic granite	
SD5	porphyritic granite	
5CM	porphyritic granite	
3A	porphyritic granite	
7CM	porphyritic granite	
2	porphyritic granite	
3	porphyritic granite	
4	porphyritic granite	
Bingham, Utah		
BGP	Bingham granite porphyry	
BQLP	Bingham quartz latite porphyry	
BWR	Bingham latite dike	
Miscellaneous		
SG-1	Stronghold granite (Cochise's Stronghold, Ariz.)	
LG-1	Sherman granite (Laramie, Wyo.)	
RM-1	altered tuff (Red Mountain, Ariz.)	
TC-1	Texas Canyon granite (Texas Canyon, Ariz.)	quartz, K-feldspar, plagioclase, biotite, muscovite
AG-1	Amole granite (Tucson, Ariz.)	
TR-3	Troy granite (Troy, Ariz.)	
TR-5	rhyodacite dike (Troy, Ariz.)	
TR-6	dacite dike (Troy, Ariz.)	
DAC	dacite flow (Superior, Ariz.)	

plutonic rocks studied have a very uniform total porosity, with all values falling within several units of 4×10^{-2}. But, similar to the carbonate rocks, ϕ'_D varies greatly, between about 5×10^{-3} and 4×10^{-5}. The calc-silicate altered rocks have large values of both total and diffusion porosity, with ϕ_T between 1.5×10^{-1} and 3×10^{-3} and ϕ'_D between about 5×10^{-3} and 5×10^{-5}.

Many of the hydrothermally altered calc-silicate and plutonic rocks have significantly greater values for both total porosity and ϕ'_D than their unaltered equivalents (tables 2 and 3). The mean total porosity for the calc-silicates from Chino, N. M. is 4.6×10^{-2}, compared to 2.4×10^{-2} for their unaltered equivalents, and the mean ϕ'_D for these same rocks is $1.2\ 10^{-3}$ as compared to $2.4\ 10^{-4}$ for the unaltered equivalents. The altered rocks from Butte, Mont. also show this trend; the mean total porosity is 3.2×10^{-2}, compared to 1.1×10^{-2}, respectively, and the mean ϕ'_D is 2.6×10^{-3}, compared to 2.4×10^{-4} for unaltered equivalents.

Comparison of the hydrothermally altered plutonic rocks from San Manuel and Sierrita-Esperanza, Ariz. with unaltered rocks from the Laramie, Wyoming and Troy, Ariz. plutons suggests a similar result, although samples SM-5, with $\phi'_D = 4.2 \times 10^{-5}$, (San Manuel, Ariz.), and CS-7 (Chino, N.M.), with $\phi_T = 7.3 \times 10^{-3}$, deviate significantly from this trend. It is interesting to note that the bulk of the difference in pore volume between hydrothermally altered rocks and their unaltered equivalents is due to a markedly larger value of residual porosity in the altered rocks (table 2). Since the mineral surface area:fluid ratio is very large, porosity increase due to irreversible chemical mass transfer in the residual pores is negligible; this larger value must be a result of either initial condition or subsequent modification of the initial porosity.

Total porosities for the isotropic metamorphic rocks studied range from about 3×10^{-2} to less than 10^{-2}; ϕ'_D for these same rocks varies from about $3.0\ 10^{-4}$ to about $4.5\ 10^{-5}$. The anisotropic rocks studied have a wider range in total porosity, with values ranging from about 10^{-1} to less than 10^{-2} (table 4). These values show that ϕ'_D parallel to foliation or bedding is significantly greater than that perpendicular, by a factor of about 2 to 7.

A consistent ratio between ϕ'_D and total porosity, that is, 4×10^{-2}, is also apparent in the data. This consistency suggests that ϕ'_D can be estimated from rather simple measurements of ϕ_T.

The total diffusion porosity, ϕ_D, may be computed from values of ϕ'_D determined above, eq (22), and the transient times required to attain steady state in the experiments. Values for an altered quartz monzonite, SM7, and a metapelite, 80, indicate that ϕ'_D is simply one axial component of ϕ_D, that is, $\phi_D = 3\phi'_D$.

RESIDUAL POROSITY

Residual porosity, ϕ_R, is the bulk of the total rock porosity since the analysis of the flow and diffusion porosity indicates that the sum of ϕ_F and ϕ_D amounts to a small fraction of the total porosity, for example, 10^{-1}. Therefore, residual porosity is $> 0.9\ \phi_T$ in fractured media.

NATURE OF PORES

Location, relative size distribution, and continuity of the pores can be determined by an analysis of porosity and mineral size distributions (figs. 7 and 8) and direct observation. The porosity distribution, exclusive of flow porosity, is obtained by measuring the density as a function

TABLE 4

Values for ϕ'_D by orientation of sample

Sample	Parallel	Perpendicular
AL007	5.40×10^{-4}	1.48×10^{-4}
AM005	13.9	2.01
PS-1-JC	8.86	4.92
BQZ	13.7	8.05

of crushed grain size. Intergranular porosity requires the density of the crushed aggregate and, hence, total measured porosity to increase as the size of the crushed grains decreases. As the crushed-grain size approaches a mineral-grain size a greater increase is expected. The contributions to porosity from pores around grains of various sizes can be calculated by using the density of the smallest grain in the interval as ρ_γ in eq 2. Measurements of this type were made on samples of the equigranular and porphyritic Schultze Granite (figs. 7 and 8).

The correlation between mineral grain size and porosity distributions for the porphyritic Schultz Granite (fig. 7) indicates the pores occur between grains and that pore size is bimodally distributed. Mode I is composed almost wholly of pores with a maximum dimension greater than 4 mm, constituting 30 percent of the total pore volume. Mode II is composed of pores that have a maximum dimension less than 1 mm, constituting 70 percent of the pore volume. In mode I there is a large increase in pore volume (30 percent), as the crushed grain size approaches 4 mm. Because this size interval corresponds to the phenocryst size range, it can be concluded that this pore volume is located around the phenocrysts. The imperfect correlation between grain size and porosity in the size interval, 4 to 1 mm, can be interpreted to mean that there is very little pore volume located around the minerals in this size interval. Finally, the porosity distribution volume in mode II roughly mimics

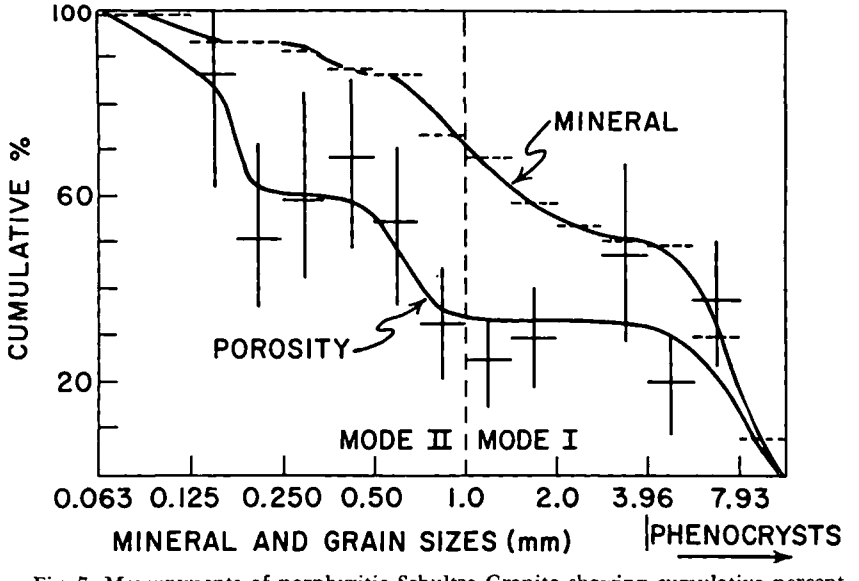

Fig. 7. Measurements of porphyritic Schultze Granite showing cumulative percentage of porosity as a function of crushed grain sizes. Horizontal bars are plotted at actual measured porosity values, with their length representing the precision of the crushed grain size measurement. Vertical bars represent the precision of the porosity measurement, also, cumulative percentage mineral sizes as a function of mineral size. Horizontal dashed lines represent precision for the size ranges.

the mineral distribution, again indicating that these pores are located around these minerals.

The intergranular nature of the pores implies that they have a maximum dimension less than or equal to their associated mineral dimension; that is, the more continuous pores are located around the larger mineral sizes. The porosity and mineral size distribution curves in mode I also indicate that 30 percent of the pore volume is located around the larger minerals, which at the most comprise 50 percent of the mineral surface area in the rock, whereas in mode II 70 percent of the pore volume is located around 30 percent of the minerals.

The porosity and mineral distribution for the equigranular Schultze Granite also shows there is one domain of porosity closely correlated with mineral distribution (fig. 8). The lack of correlation in mode I, however, permits two conclusions about pore location and continuity. The larger pores are either intergranular and less than or equal to the mineral dimensions or elongate pores that crosscut mineral boundaries.

The continuity of intergranular pores in the porphyritic Schultze Granite can be determined from ϕ'_D values for samples of varying thicknesses (fig. 9). Large increases in ϕ'_D indicate large abundances of pores with a maximum dimension equal to that sample thickness. These data indicate a discontinuity at about 8 mm, which is also suggested by correlative changes of porosity and mineral abundance distribution

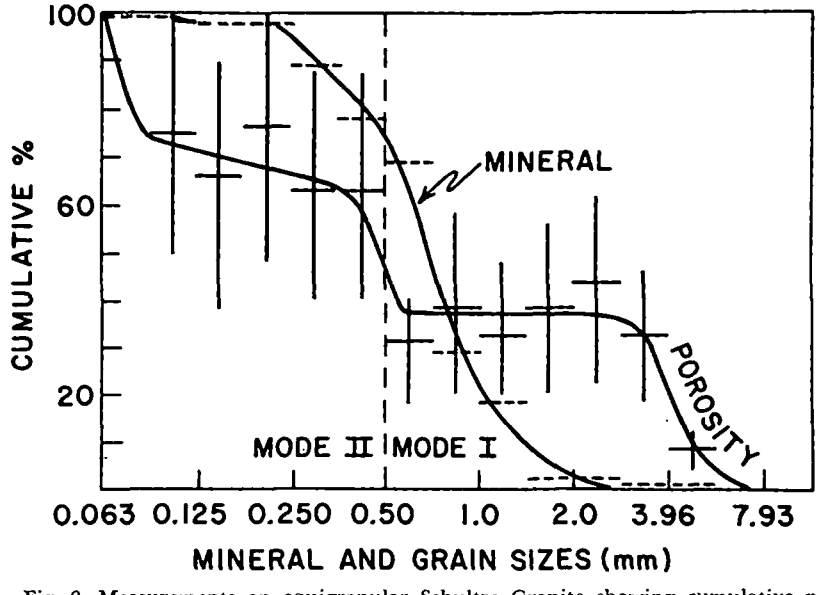

Fig. 8. Measurements on equigranular Schultze Granite showing cumulative percentage of porosity as a function of crushed grain sizes. Horizontal bars are plotted at actual measured porosity values, with their length representing the precision of the crushed grain size measurement. Vertical bars represent the precision of the porosity measurement, also, cumulative percentage mineral sizes as a function of mineral size. Horizontal dashed lines represent precision for the size ranges.

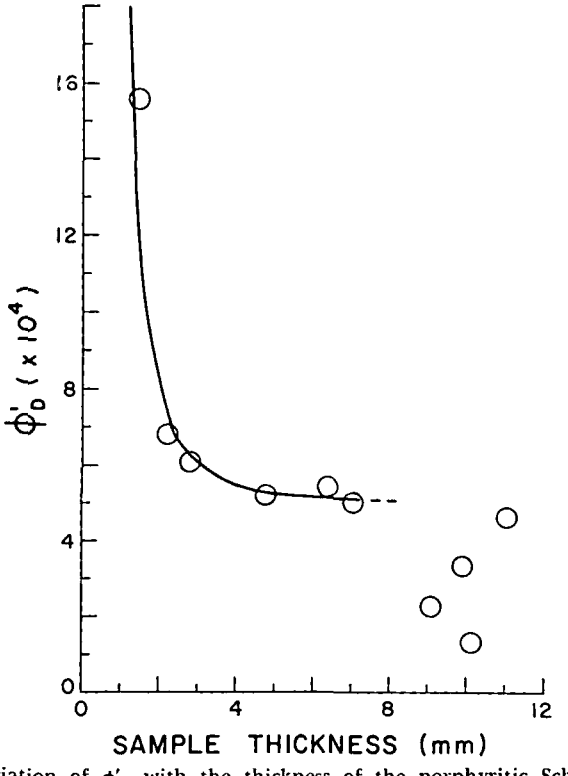

Fig. 9. Variation of ϕ'_D with the thickness of the porphyritic Schultze Granite samples used in diffusion experiment.

curves in mode I (fig. 7). This discontinuity indicates that there is a large abundance of pores with a maximum dimension of about 8 mm and that these more continuous pores are located around the phenocrysts.

The large increase in ϕ'_D at about 2 mm (fig. 9) indicates that the preponderance of pores have a maximum dimension less than this length. This increase of ϕ'_D approaches the value of the total porosity as the sample thickness approaches zero. Previous experiments determined (Garrels, Dreyer, and Howland, 1949) that $\phi'_D/\phi_T = 0.4$ for limestone samples 1 to 2 mm thick. These values are in general agreement with those reported in our study, if one assumes the relationship in figure 9 holds for a variety of rock types.

The geometry of discontinuous pores in fractured media may be classified into two broad categories, equidimensional pores and microcracks. Equidimensional pores vary from less than 1 mm to as great as 5 mm. This upper limit in size for equidimensional pores coincides with the large increase in the porosity distributions (figs. 7 and 8) and serves as partial confirmation of these curves. The pores composing this category have shapes that range from prismatic to highly irregular. Observed apertures of the microcracks range from less than 1 μm to no

PLATE 2

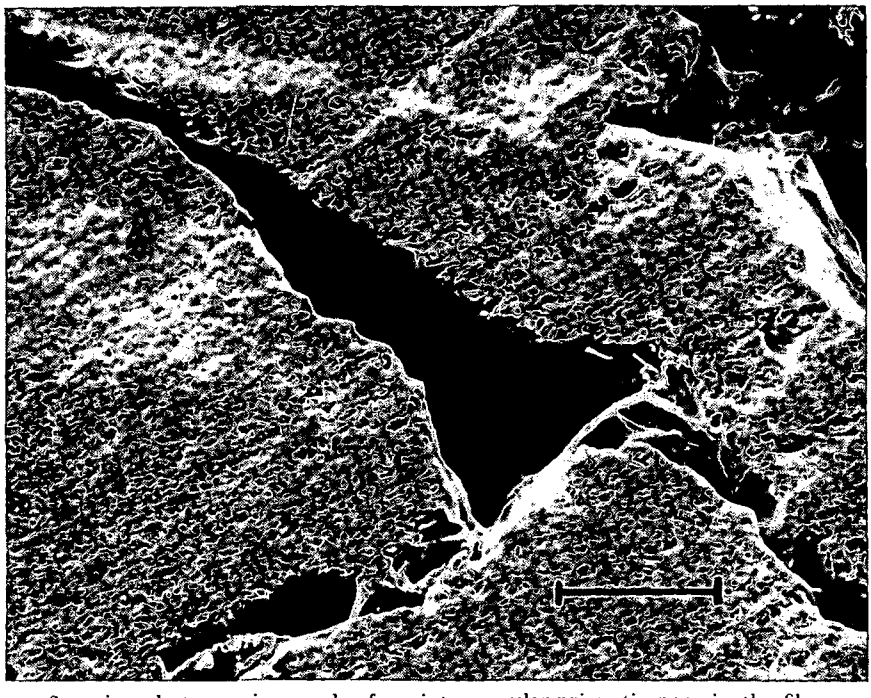

Scanning electron micrograph of an intergranular-prismatic pore in the Sherman Granite. This type of pore probably represents the geometry and size of diffusion and/or residual pores. The scale bar is 100 μm.

greater than 40 μm. Clearly, the small values for the apertures require the bulk of the pore volume to be composed of equidimensional pores. The suggested intergranular nature of the pores is also supported by the above observations, since the equidimensional pores are clearly distributed around grain boundaries (pl. 2).

In summary, the above data suggest that a general porosity model for fractured igneous rocks consists of continuous planar fractures, ϕ_F, and cylindrical pores, ϕ_D (fig. 10).

ADVECTION–REACTION–DIFFUSION

Porosity data define the distribution of fluids in hydrothermal systems. This information permits formulation of the governing partial differential equations for the advection-diffusion-reaction of aqueous species in a hydrothermal system.

The actual paths described by circulating packets of fluid in and around cooling intrusive bodies are defined in two dimensions by

$$\frac{dx}{\bar{v}_x} = \frac{dz}{\bar{v}_z} = dt, \tag{23}$$

where $\bar{v}_x$ and $\bar{v}_z$ are the component velocities. Examples of these pathlines in hydrothermal systems are presented in Norton and Knight, 1977. Fluids circulating along pathlines flow from one chemical environment into another, which results in differences in fluid compositions between those fluids in the flow porosity and those in the diffusion porosity, as well as disequilibrium between fluids and mineral phases. The transfer of heat between circulating fluid and rock may cause further disequilibrium within a rock volume. The mass transfer resulting from this disequilibrium occurs within flow porosity and diffusion porosity.

Advective transport depends directly on the magnitude of the flow velocities in ϕ_F. For flow velocities normally realized in these systems, a parabolic flow profile develops in less than a meter along the fracture and is effective over a thickness equal to half the fracture aperture (fig. 10). The true velocity in the fracture varies from zero at the wall of the fracture to an average value, defined by

$$\bar{v}_t = \frac{\bar{v}_{Darcy}}{\phi_{flow}}. \tag{24}$$

Therefore, the advective flux of the i^{th} ion is

$$\bar{u}_i = \bar{v}_t m_i \phi_F \rho. \tag{25}$$

The diffusional flux within ϕ_F parallel to the flow direction and across a concentration boundary layer, δ_c, follows from eq (17) with the substitution of ϕ_F for ϕ_D.

$$\bar{u}_{iF} = -\phi_F \sum_k D_{ik} \nabla_{xy} m_k. \tag{26}$$

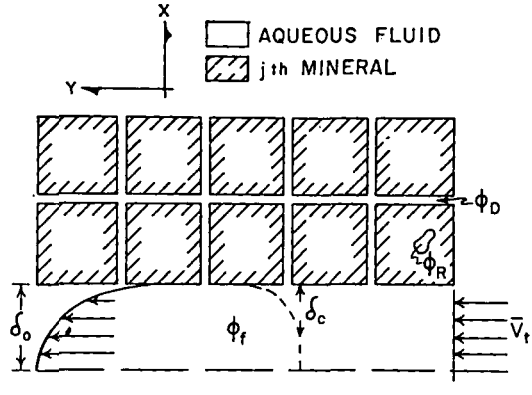

Fig. 10. Schematic two-dimensional porosity model for homogenous and isotropic ϕ_D. The model represents a possible geometric distribution of pores with respect to discrete minerals and is consistent with data collected in this study. In particular, we note that diffusion pores, ϕ_D, occur along each mineral grain boundary and interconnect with continuous fractures, ϕ_F. Although the relative abundance of the porosity types is not represented in this schematic representation, typical values for the porosity parameter are $\phi_D = 2 \times 10^{-4}$, $\phi'_D = 3\phi_D$, $\tau = 1$, diffusion pore radius of 10^{-3} cm and mineral sizes of 0.14 cm. The model and values are a first order approximation of pore geometry in fractured rocks.

As discussed previously, aqueous diffusion is the dominant transport mechanism within the diffusion pores and is defined by

$$\bar{u}_{iD} = -\phi'_D \sum_k D_{ik} \nabla_{xy} m_k. \tag{27}$$

The total flux of the i^{th} ion from the representative region, R, can be obtained by summing the advective and diffusive fluxes within the flow porosity domain and the diffusive flux within the diffusion porosity domain (eqs 25, 26, and 27).

$$\bar{S}_i = \bar{u}_i + \bar{u}_{iF} + \bar{u}_{iD}. \tag{28}$$

An expression for the total amount of the i^{th} ion in R available for transport can be obtained by modifying eq (19) to read

$$M_i = \int_R \rho (\phi_F + \phi_D) (m_i + A_i m_i) \, dV. \tag{29}$$

The amount of the i^{th} ion loss from R is equal to the volume integral of the divergence of $\bar{S}_i$,

$$-\int_R \operatorname{div} \bar{S}_i \, dV, \tag{30}$$

and must be equal to the rate of depletion of the ion in R, that is, the time derivative of eq (29). Introducing a conservation of mass and combining the time derivative of eqs (29) and (30) results in the governing partial differential equation for conservation of the i^{th} aqueous species:

$$\rho (\phi_F + \phi_D) (A_i + 1) \frac{\partial m_i}{\partial t} + \rho \bar{v}_t \phi_F \nabla_{mi} = \nabla D_{ik} \phi_F \nabla m_k + \nabla D_{ik} \phi'_D \nabla m_k. \tag{31}$$

Eq (31), together with the partial differential equations describing fluid flow in pluton environments, accounts for the circulation of fluids through reactive host rocks. This formulation is fundamentally different from previously derived equations in that it explicitly affords for the appropriate porosity values in fractured rocks. Other formulations utilize total rock porosity, which may produce significantly different results since we found ϕ_T is as large as several orders of magnitude greater than $(\phi_D + \phi_F)$.

ACKNOWLEDGMENTS

This research was supported by NSF Grant nos. GA-41136 and EAR74-03515-A01 and the University of Arizona. We wish to thank Dr. Timothy Loomis, Mr. Bill Baltosser, Bear Creek Mining Company, the University of Arizona chapter of SGE, and the Anaconda Company for donating samples and rock descriptions which greatly enhanced the scope of this study. We also wish to thank Lynn McLean for improvements in the manuscript.

REFERENCES

Bianchi, L., and Snow, D. T., 1969, Permeability of crystalline rocks interpreted from measured orientations and apertures of fractures: Jodphur, Rajasthan, Arid Zone Research Assoc. of India, Annals of Arid Zone, v. 8, no. 2, p. 231-245.

Boardman, C. R., and Skrove, J., 1966, Distribution in fracture permeability of a granitic rock mass following a contained nuclear explosion: Jour. Petroleum Technology, v. 18, p. 619-623.

Brace, W. F., Walsh, J. B., and Frangos, W. T., 1968, Permeability of granite under high pressure: Jour. Geophys. Research, v. 73, p. 2225-2236.

Brace, W. F., 1971, Resistivity of saturated crustal rocks to 40 km based on laboratory measurements, *in* Heacock, J. G., ed., The structure and physical properties of the Earth's crust: Am. Geophys. Union, Geophys. Mon. Ser., v. 14, p. 243-255.

Cadek, J., Hazdrova, M., Kacura, G., Krasny, J., and Malkovsky, M., 1968, Hydrogeology of the thermal waters at Teplice and Usti nad Labem: Sbornik Geol. Ved, Hydrogeol., Inzenyrska Geol., rada HIG, sv. 6, p. 1-184.

Davis, S. N., 1969, Porosity and permeability of natural materials, *in* DeWiest, R. J. M., ed., Flow through porous media: New York, Acad. Press, p. 54-90.

DeWiest, R. J. M., 1965, Geohydrology: New York, John Wiley & Sons, Inc., 366 p.

Fatt, I., 1956, The network model of porous media: Am. Inst. Mining Engineers, Petroleum Trans., v. 207, p. 141-181.

Garrels, R. M., Dreyer, Z. M., and Howland, D. L., 1949, Diffusion of ions through intergranular spaces in water saturated rocks: Geol. Soc. America Bull., v. 60, p. 1809-1828.

Grindley, G. W., 1965, The geology, structure, and exploitation of the Wairakei geothermal field: Taupo, New Zealand: Wellington, New Zealand Geol. Survey, 131 p.

Hubbert, M. K., 1940, The theory of ground-water motion: Jour. Geology, v. 48, p. 785-944.

Jackson, D. B., 1966, Deep resistivity probes in the southwestern United States: Geophysics, v. 31, p. 1123-1144.

Keller, G. V., Anderson, L. A., and Pritchard, J. I., 1966, Geological survey investigations of the electrical properties of the crust and upper mantle: Geophysics, v. 31, p. 1078-1087.

Knapp, R. B., ms, 1975, An analysis of the porosities of fractured crystalline rocks: M.S. thesis, Univ. Arizona, 90 p.

Maini, Y. N. T., ms., 1971, In situ hydraulic parameters in jointed rock—their measurement and interpretation: Ph.D. dissert., Univ. London, 312 p.

Marine, I. W., 1966, Hydraulic correlation of fracture zones in buried crystalline rock at the Savannah River plant, near Aiken, South Carolina: U.S. Geol. Survey Prof. Paper 550-D, p. 223-227.

Norton, D. L., and Knight, J. E., 1977, Transport phenomena in hydrothermal systems: cooling plutons: Am. Jour. Sci., v. 277, p. 937-981.

Ohle, E. L., 1951, The influence of permeability on ore distribution in limestone and dolomite: Econ. Geology, v. 46, p. 667-706.

Plauff, D., 1966, Magneto-telluric soundings in the southwestern United States: Geophysics, v. 31, p. 1145-1152.

Pratt, H. R., Black, A. D., Brace, W. F., and Norton, D. L., 1974, In situ joint permeability in a granite: EOS, Am. Geophys. Union Trans., v. 55, p. 433.

Snow, D. T., ms, 1965, A parallel plate model of fractured permeable media: Ph.D. dissert., Univ. California, Berkeley, 331 p.

———— 1970, The frequency and apertures of fractures in rock: Internat. Jour. Rock Mechanics Min. Sci., v. 7, p. 23-40.

Villas, R. N., ms., 1975, Fracture analysis, hydrodynamic properties and mineral abundance in altered igneous wall rocks of the Mayflower mine, Park City district, Utah: Ph.D. dissert., Univ. Utah, Salt Lake City, 253 p.

Winograd, I. J., 1971, Hydrogeology of ash flow tuff: a preliminary statement: Water Resources Research, v. 7, p. 994-1006.